Building blocks for atomically assembled magnetic and electronic artificial lattices

Rejali, R.

DOI
10.4233/uuid:02cd1165-9fef-4613-a12c-dc3c4bd9d731

Publication date
2022

Document Version
Final published version

Citation (APA)
Rejali, R. (2022). *Building blocks for atomically assembled magnetic and electronic artificial lattices*. [Dissertation (TU Delft), Delft University of Technology]. https://doi.org/10.4233/uuid:02cd1165-9fef-4613-a12c-dc3c4bd9d731

Important note
To cite this publication, please use the final published version (if applicable).
Please check the document version above.

BUILDING BLOCKS FOR ATOMICALLY ASSEMBLED MAGNETIC AND ELECTRONIC ARTIFICIAL LATTICES

BUILDING BLOCKS FOR ATOMICALLY ASSEMBLED MAGNETIC AND ELECTRONIC ARTIFICIAL LATTICES

Dissertation

for the purpose of obtaining the degree of doctor
at Delft University of Technology
by the authority of the Rector Magnificus Prof. Dr. ir. T.H.J.J. van der Hagen
chair of the Board for Doctorates
to be defended publicly on
Tuesday 27 September 2022 at 10:00 o'clock

by

Rasa REJALI

Master of Science in Physics,
McGill University, Montreal, Canada,
born in Esfahan, Iran.

This dissertation has been approved by the promotors.

Prof. dr. A. F. Otte
Dr. T. van der Sar

Composition of the doctoral committee:

Rector Magnificus,	chairperson
Prof. dr. A. F. Otte,	Delft University of Technology, promotor
Dr. T. van der Sar,	Delft University of Technology, copromotor

Independent members:

Prof. dr. Y. M. Blanter,	Delft University of Technology
Prof. dr. ir. H. S. J. van der Zant	Delft University of Technology
Prof. dr. ir. H. J. W. Zandvliet	University of Twente
Dr. S. C. Conesa-Boj,	Delft University of Technology
Dr. I. Swart,	Utrecht University

Keywords: Scanning tunneling microscopy, inelastic electron tunneling spectroscopy, single atom magnetism, field-emission resonances, artificial lattices

Printed by: Gildeprint, Enschede

Front & Back: Artistic impression of the band structure of graphene.

Casimir PhD Series 2022-22, Delft-Leiden

ISBN 978-94-6366-589-6

An electronic version of this dissertation is available at
http://repository.tudelft.nl/.

To my loving parents.

CONTENTS

SUMMARY

This thesis focuses on possible platforms for a bottom-up approach towards realizing and characterizing atomically assembled magnetic and electronic artificial lattices. For this, we make use of the scanning tunneling microscope (STM), which provides a local probe of the magnetic and electronic properties of the sample and allows for the atom-by-atom construction of extended lattices. On the one hand, to address avenues for constructing extended spin lattices, we study single Fe atoms coordinated on the four-fold symmetric nitrogen binding site of the Cu_2N/Cu_3Au surface—a system which permits large-scale atomic assembly, and allows for independent access to both the orbital and spin degrees of freedom. On the other hand, we investigate the viability of laterally confined vacuum resonances on the chlorinated Cu(100) surface as a basis for constructing electronic lattices. We atomically assemble dimers and trimers of various geometries to determine the tight-binding parameters, and as a proof of concept, experimentally realize a looped Su-Schrieffer–Heeger chain using this platform. These studies are made possible by means of a low-temperature, ultra-high vacuum STM, which allows for atom manipulation and, via spectroscopic techniques, permits us to locally probe the sample density of states and detect inelastic excitations of the spin and orbital angular momentum.

In **chapter 1**, we set the stage by sketching the subject matter of this thesis and contextualizing it in terms of existing literature. Similarly, **chapter 2** outlines the theoretical framework necessary for understanding single atom magnetism in the context of effective Hamiltonians. This chapter also provides a brief overview of the tight binding method for describing the electronic structure of lattices. In **chapter 3**, we shift gears to focus on the experimental methods relevant to the work presented in this thesis, such as the basic principles of scanning probe microscopy, as well as an overview of spectroscopic and atom manipulation techniques.

Chapter 4 presents a detailed look at nitrogen-bound Fe atoms on the Cu_2N/Cu_3Au surface: the symmetry of this binding site engenders a nearly uniaxial crystal field that preserves the orbital momentum of these magnetic adatoms in the out-of-plane direction. The unquenched orbital moment leads to an enhanced single ion anisotropy, which carries direct consequences for the stability and lifetime of the atom's magnetization. Furthermore, a sufficiently weak spin-orbit coupling permits us to address the spin and orbital degrees of freedom separately, inciting and probing independent excitation of each magnetic moment. In addition to a conventional spin excitation, we observe an inelastic orbital excitation that corresponds to a full reversal of the atomic orbital momentum. This process is facilitated by a charged virtual state, and leaves the atom's spin stated unaltered. These results, in conjunction with the easy atom manipulation afforded by this platform, form a promising outlook for future studies on magnetic artificial lattices, in which the constituent building blocks can interact via both the spin and orbital angular momentum.

Chapter 5 is devoted to the study of laterally confined field-emission resonances, which can be seen as artificial atoms in the context of atomically assembled electronic lattices. In this chapter, we use atom manipulation of single chlorine vacancies on the chlorinated Cu(100) surface to construct atomic-scale potential wells along the surface: by assembling vacancies to reveal a square patch of the underlying metal, we can engineer lateral confinement of the vacuum-localized electronic states, thereby generating particle-in-a-box modes. We demonstrate that alterations of the confining potential—which can either be implemented via a changing tip-sample distance or through atom manipulation—can be used to carefully tune the electronic lifetime of these states. To determine the lifetime-limiting processes, we model the transport through the confined resonances: in doing so, we find the electron lifetime depends critically on bulk band structure of the underlying structure. Demonstrating control over the electronic lifetime, and consequently the time-average state occupation, is a useful proof of concept for studies focusing on simulating quantum many-body states with artificial lattices.

In **chapter 6**, we assess the feasibility of using laterally confined field emission resonances as a platform for artificial lattices. We begin by characterizing the coupling between confined vacuum states in various dimer and trimer geometries. Our results indicate that hybridization only occurs with the aid of a so-called bridging patch, which constitutes an additional exposed metal patch connecting neighbouring patches. Within this context, we find we can tune the hopping strength, the orbital overlap, and the on-site energy of these artificial atoms by adjusting the structure geometry. We use this platform to realize a looped dimerized chain; as expected from previous works, differential conductance measurements support the existence of a domain wall state in this structure. We point to future avenues for exploring topological states in higher energy bands, such as those found in a diamond chain lattice.

Chapter 7 addresses the more technical aspects of field-emission resonances. Namely, we discuss a simple one-dimensional approach for modelling the out-of-plane potential to reproduce the key features of laterally unconfined field-emission resonances, such as their spatial extent and energy. Additionally, we propose a normalization scheme for extracting quantitative information about the local density of states from constant-height or constant-current differential conductance measurements taken at applied bias voltages exceeding the sample work function. Finally, we present a transport model for estimating the electronic lifetimes of these vacuum-localized, discretized states from height-dependent spectroscopic data. We benchmark this method for a bare Cu(100) surface and recover a lifetime that is in fair agreement with previously reported values.

SAMENVATTING

Dit proefschrift richt zich op mogelijke platforms voor een bottom-up benadering voor het realiseren van atomair opgebouwde magnetische en elektronische kunstmatige roosters. Hiervoor maken we gebruik van de scanning tunneling microscoop (STM), die lokaal inzicht biedt in de magnetische en elektronische eigenschappen van materialen en de atoom-voor-atoom constructie van verlengde roosters mogelijk maakt. Enerzijds bestuderen we afzonderlijke Fe-atomen geplaatst op de viervoudige symmetrische stikstofbindingsplaats van het Cu_2N/Cu_3Au-oppervlak — een systeem dat atomaire opstellingen op grote schaal mogelijk maakt, en zorgt voor onafhankelijke toegang tot zowel de orbitale als de spin-vrijheidsgraden—om methodes voor het bouwen van verlengde spinroosters te vinden. Anderzijds onderzoeken we de haalbaarheid van lateraal opgesloten vacuümresonanties op het gechloreerde Cu(100)-oppervlak als basis voor het construeren van elektronische roosters. We creëren atomaire dimeren en trimeren van verschillende geometrieën om de *tight-binding* parameters te bepalen en verwezenlijken, als *proof of concept*, een lusvormige Su-Schrieffer–Heeger keten met dit platform. Deze studies worden mogelijk gemaakt door middel van een lage-temperatuur, ultrahoog vacuüm STM, die atoommanipulatie mogelijk maakt en, via spectroscopische technieken, ons in staat stelt om lokaal de dichtheid van toestanden te onderzoeken en inelastische excitaties van het spin en orbitale impuls moment te detecteren.

In **Hoofdstuk 1** leggen we de basis door het onderwerp van dit proefschrift te schetsen en het in termen van bestaande literatuur te plaatsen. Op dezelfde manier schetst **Hoofdstuk 2** het theoretische raamwerk dat nodig is om het magnetisme van één atoom te begrijpen in de context van effectieve Hamiltonianen. Dit hoofdstuk geeft ook een kort overzicht van de *tight-binding* methode voor het beschrijven van de elektronische structuur van roosters. In **Hoofdstuk 3** verleggen we de focus naar de experimentele methoden die relevant zijn voor het werk dat in dit proefschrift wordt gepresenteerd, zoals de basisprincipes van scanning probe microscopie, evenals een overzicht van spectroscopische en atoommanipulatietechnieken.

Hoofdstuk 4 geeft een gedetailleerd overzicht van stikstofgebonden Fe-atomen op het Cu_2N/Cu_3Au-oppervlak: de symmetrie van deze bindingsplaats veroorzaakt een bijna uniaxiaal kristalveld dat het orbitale impulsmoment van deze magnetische adatoms in de richting uit het vlak behoudt. Het niet-samengedrukte orbitale moment leidt tot een versterkte enkel-ion-anisotropie, wat directe gevolgen heeft voor de stabiliteit en levensduur van de magnetisatie van het atoom. Bovendien stelt een voldoende zwakke spin-baankoppeling ons in staat om de spin- en orbitale vrijheidsgraden afzonderlijk aan te pakken, en onafhankelijke excitatie van beide magnetisch momenten op te wekken en te onderzoeken. Naast een conventionele spin-excitatie, nemen we een inelastische orbitale excitatie waar die overeenkomt met een volledige omkering van het atomaire orbitale moment—dit proces wordt mogelijk gemaakt door een geladen virtuele toestand en laat de spin van het atoom onveranderd. Deze resultaten, in combinatie met de gemak-

kelijke atoommanipulatie die dit platform biedt, vormen een veelbelovend vooruitzicht voor toekomstige studies over magnetische kunstmatige roosters, waarin de bouwstenen kunnen interageren via zowel de spin als het orbitale impulsmoment.

Hoofdstuk 5 is gewijd aan de studie van lateraal begrensde veldemissieresonanties, die gezien kunnen worden als kunstmatige atomen in de context van atomair opgebouwde elektronische roosters. In dit hoofdstuk gebruiken we atoommanipulatie van enkelvoudige chloorvacancies op het gechloreerde Cu(100)-oppervlak om op atomaire schaal potentiaalputten langs het oppervlak te construeren: door vacancies zo te manipuleren dat ze een vierkant stukje van het onderliggende metaal onthullen, maken we laterale opsluiting van de vacuümgelokaliseerde elektronische toestanden mogelijk, waardoor deeltjes-in-een-doos toestanden worden gecreëerd. We demonstreren dat veranderingen van het beperkende potentiaal—die kunnen worden geïmplementeerd via een veranderende tip-sample afstand of door atoommanipulatie—kunnen worden gebruikt om de elektronische levensduur van deze toestanden zorgvuldig af te stellen. Om de levensduurbeperkende processen te bepalen, modelleren we het transport door de resonanties: hierbij ontdekken we dat de levensduur van het elektron in grote mate afhangt van de bulkbandstructuur van de onderliggende structuur. Het demonstreren van controle over de levensduur van het elektron, en bijgevolg de tijdsgemiddelde toestandsbezetting, is een nuttig *proof of concept* voor studies die zich richten op het simuleren van kwantum veel-lichaam toestanden met kunstmatige roosters.

In **Hoofdstuk 6** onderzoeken we de haalbaarheid van het gebruik van lateraal begrensde veldemissieresonanties als platform voor kunstmatige roosters. We beginnen met het karakteriseren van de koppeling tussen beperkte vacuümtoestanden in verschillende dimeer- en trimeergeometrieën. Onze resultaten geven aan dat hybridisatie alleen plaatsvindt met behulp van een zogenaamd overbruggingsstuk, dat een extra blootgestelde stuk metaal vormt dat aangrenzende stukken verbindt. Binnen deze context vinden we dat we de hopsterkte, de orbitale overlap en de lokale energie van deze kunstmatige atomen kunnen afstemmen door de geometrie van de structuur aan te passen. We gebruiken dit platform om een lusvormige gedimeriseerde keten te realiseren; zoals verwacht op basis van eerdere werken, ondersteunen differentiële geleidingsmetingen het bestaan van een domeinwandtoestand in deze structuur. We wijzen op toekomstige wegen voor het verkennen van topologische toestanden in hogere energiebanden, zoals die gevonden zijn in een diamanten kettingrooster.

Hoofdstuk 7 behandelt de meer technische aspecten van veldemissieresonanties. We bespreken namelijk een eenvoudige ééndimensionale benadering voor het modelleren van het potentiaal in de normaalrichting van het vlak om de belangrijkste kenmerken van lateraal onbeperkte veldemissieresonanties te reproduceren, zoals hun reikwijdte en energie. Daarnaast dragen we een normalisatieschema's aan voor het extraheren van kwantitatieve informatie over de lokale dichtheid van toestanden uit differentiële geleidingsmetingen met constante hoogte of constante stroom uitgevoerd bij aangelegde spanningen die de werkfunctie van het materiaal overschrijden. Ten slotte presenteren we een transportmodel voor het schatten van de elektronische levensduur van deze gediscretiseerde toestanden op basis van hoogteafhankelijke spectroscopische gegevens. We benchmarken deze methode voor een kaal Cu(100)-oppervlak en vinden een levensduur die redelijk in overeenstemming is met eerder gerapporteerde waarden.

1

INTRODUCTION

We often describe materials in terms of their atomic constituents, casting the bulk magnetic and electrical properties as collective behaviour that emerges from the interactions between these building blocks. Implicit to this framework are two entangled concepts: the transition between the physics that governs single atoms to the principles dictating the bulk behaviour of materials; as well as the nature and impact of the various interatomic interactions at play. One avenue towards gaining understanding of these two facets is via so-called artificial lattices, which take a bottom-up approach towards engineering and studying novel states of matter [1–3]. These designer lattices can function as model systems, lending insight into the evolution of material properties and allowing for control over the symmetries and interactions responsible for specific electronic and magnetic behaviour. Moreover, this approach circumvents the issues surrounding material synthesis and allows for creating toy models for simulating physical systems that are computationally intractable, such as those hosting many-body quantum states [4–11].

Although a range of experimental platforms have been used for the creation of artificial matter [6, 9–14], the low-temperature scanning probe framework is uniquely suited to such studies as it provides a local measure of the sample density of states and enables atom-by-atom assembly of extended architectures [1–3]. Unlike self-assembled artificial lattices [15–17]—which allow for relative ease and rapidity in realizing large-scale lattices—the freedom permitted by atom manipulation can be advantageous when seeking a high degree of flexibility and precision. In this case, the lattice is constructed by meticulously coordinating single atoms or molecules into the desired position. This allows for complete customizability of the lattice architecture, including the deliberate introduction of defects and impurities. Moreover, recent advances demonstrating automatable and large-scale atom manipulation renders this methodology well-suited to the construction of lower-dimensional artificial matter [18].

To date, several studies have made use of the atom manipulation capabilities offered by low-temperature scanning tunneling microscopy to realize a variety of artificial lattices, and to study their designed electronic and magnetic properties using spectroscopic techniques [19–32]. Two distinct approaches are usually taken for investigating

artificial electronic and magnetic architectures: for the former, atomic or molecular impurities are positioned to realize a particular potential landscape through quantum confinement; whereas in the latter case, spin lattices are constructed by manipulating adsorbates with a well-defined magnetic moment. In the following, we will detail common approaches towards controlling and studying the electronic and spin degrees of freedom in artificial lattices within a scanning probe framework.

The electronic structure and properties of model systems can be simulated with artificial electronic lattices, which provide a high degree of control over the lattice parameters and are typically devoid of real-world complications, making their characterization more straightforward. The ability to construct these systems from the bottom-up allows us to closely trace the evolution of the electronic band structure, tune the interaction strength of the constituent artificial atoms, and tailor the geometry of the overall lattice. This freedom permits a detailed look at the effects of strain, reduced dimensionality, symmetry and periodicity (or the lack thereof), defects, coupling, and topology [19–28]. The constituents of artificial electronic lattices typically find their origin in quantum confinement: the first demonstrations of engineered confinement of electronic states through atomic assembly showed the emergence of quantum well states [33, 34]—a series of discretized states whose energy and spatial extent depend on the particulars of the confining potential, analogous to the bounds states of an atom [19, 35–39]. Several avenues have been pursued for achieving this localization to engineer artificial atoms, such as assembling adatom clusters to generate an attractive potential [35, 36], positioning adsorbates to create a scattering potential [37, 38], and using atomic-scale defects, like vacancies in a dielectric monolayer [19, 25–27] and dangling bonds [39]. A constraint in the scope of such studies thus far is the limited coherent lifetime of the engineered electron states [40, 41], which prohibits investigations of many-body states and electronic correlations.

A similar simulative approach can be applied to the study of magnetism—a collective phenomena that arises when individual atomic spins interact to form an ordered array. In this case, local spins are manipulated in place to construct extended magnetic architectures, and probed using spin-sensitive spectroscopic techniques. The choice of surface can be critical to the atom manipulation possibilities, as well as to the lifetime and nature of the spin states, with the most common substrates consisting of metal surfaces, such as Cu(111) [29] or Pt(111) [42], or ultra-thin insulators grown on bulk metallic crystals, such as Cu_2N on Cu(100) [30, 32, 43–45] or MgO on Ag(100) [46–48]. Equally relevant is the choice of adsorbate: this determines the magnitude of the magnetic moment and the relevance of spin-orbit interactions, with transition metal atoms—such as iron, manganese, and cobalt—constituting typical choices. Much like their electronic analog, a certain degree of freedom is permitted in designing artificial magnetic lattices through the choice of surface and adsorbate: in this case, the relevant parameters are the magnet moment, the spin-spin interactions, the magnetic anisotropy, and the lifetime of the magnetic states. In conjunction with control over the magnitude and direction of the external magnetic field, these parameters allow for creating spin lattices that exist in distinct coupling regimes and exhibit, for instance, bistable magnetic states [44, 45, 49, 50], frustrated spin textures [29], non-collinear spin states [51], and long-range spin correlations [44, 52].

Finding an appropriate and versatile platform is part of the challenge facing experimental realizations of artificial electronic and magnetic lattices. In both cases, the scope of study is largely limited by the characteristics of the individual building blocks, which is in turn partly determined by the choice of material platform. This constitutes the main focus of this thesis: exploring and addressing candidate building blocks for constructing extended artificial lattices from the bottom-up.

Chapters 2 and 3 will address the relevant theoretical and experimental groundwork necessary for descriptions of low-dimensional magnetism and the electronic structure of lattices. From there, we will turn our focus to a promising spin system for the study of magnetic lattices: an Fe atom coordinated atop the four-fold symmetric nitrogen binding site of the $Cu_2N/Cu(100)$ surface. Our findings, detailed in chapter 4, indicate that the highly symmetric local environment preserves the free-atom value of the orbital momentum along the out-of-plane direction, which, in conjunction with a sufficiently weak spin-orbit coupling, enables the decoupling of the spin and orbital angular momentum. This forms a promising basis for constructing magnetic lattices that rely on interactions mediated by both these magnetic degrees of freedom.

Subsequently, we shift gears to address a new avenue for building electronic artificial lattices: laterally confined vacuum resonances. In chapter 5, we characterize the resultant discretized states and model the transport through them to estimate the electronic lifetime. Our results demonstrate that we can tune the average lifetime and occupation of these states by changing the overall confining potential, be it through atomic assembly or variations in the tip-sample distance. We more directly address the suitability of using these confined vacuum resonances as a platform for artificial lattices in chapter 6, where we characterize the coupling parameters for dimers and trimers of various geometries. As a proof of principle, we construct a well-understood looped dimerized chain and recover the expected behaviour. We additionally indicate possible routes for studying topological states in higher energy bands with this platform. Finally, chapter 7 addresses the theoretical and experimental challenges in deriving quantitative information from differential conductance measurements of these vacuum resonances, and proposes solutions—such as a normalization method for extracting the local density of states, and a simple transport model for deducing the lifetime—for overcoming such hurdles.

2

THEORETICAL FRAMEWORK

The atom-by-atom realization of quantum states of matter generally relies on understanding and controlling the interactions between electrons, orbitals, and spins. In this chapter, we present two theoretical frameworks for treating the constituent building blocks of artificial spin and electronic lattices: first, we will discuss low-dimensional magnetism in the context of an effective Hamiltonian that treats the relevant interactions at play—such as the crystal field, spin-orbit coupling, and Zeeman interaction. Second, we will present a basic overview of the tight-binding method for describing the electronic structure of coupled spinless atoms in extended structures.

2.1. DESCRIBING SINGLE ATOM MAGNETISM

The magnetic moment of an atom is typically determined by the orbital magnetic moment, whose origin lies in the orbital motion of the valence electrons in space, and the spin magnetic moment, which arises from the valence electrons' intrinsic angular momentum, i.e. their spin. These two contributions are usually of similar magnitude in an isolated atom with full rotational symmetry. Accordingly, the state of an electron in a free atom is defined—in the absence of strong spin-orbit coupling—by four quantum numbers: the orbital momentum ℓ and its associated magnetic quantum number m_ℓ, the magnetic spin quantum number m_s, which specifies the component of the total spin s along the quantization axis, and, the principal quantum number n. The spherical symmetry of the isolated atom preserves the degeneracy between the m_ℓ subshells that correspond to a specific orbital momentum ℓ, which, in combination with the spin multiplicity, results in $(2\ell+1)(2s+1)$ states in the ground state multiplet [53, 54]. As such, the electron configuration of the ground state can be trivially predicted by Hund's rules [55].

However, the electron states can dramatically change when the atom is placed in a crystal environment: in this case, the atom is subject to a static electric field generated by the ions in the crystal, referred to as the crystal field. The crystal field violates the spherical symmetry of the free atom, and imposes the local (point) symmetry of the crystal structure. Interactions between the valence electrons of the central atom and the surrounding ions (ligands) can raise or lower the energies of the valence atomic orbitals, thereby breaking the degeneracy characteristic of an isolated atom. This crystal field splitting can complicate predictions of the ground state multiplet and carry implications for the magnetic moments of the central atom [53, 55, 56].

A common method for simplifying this problem is to condense the relevant interactions at play into an effective Hamiltonian framework. This approach has been widely used to predict and understand the magnetic properties of surface-adsorbed magnetic atoms, where it is possible to only consider the magnetic degrees of freedom: the orbital moment and the spin. We will discuss the interactions pertinent to surface-adsorbed magnetic atoms—such as the crystal field (section 2.1.1), the spin-orbit coupling (section 2.1.2), and the Zeeman interaction (section 2.1.3)—and how they are incorporated into an effective Hamiltonian that solely accounts for the relevant magnetic degrees of freedom.

2.1.1. THE ORIGIN AND EFFECTS OF CRYSTAL FIELDS

Crystal fields can have a significant impact on the magnetic properties and ground-state multiplets of surface-adsorbed atoms—but the magnitude and nature of these effects critically depends on the symmetry of the local environment and the degree of orbital overlap between the central atom and the neighbouring ligands. To better elucidate the role of the crystal field, we will initially restrict our focus to the point-charge contribution to the crystal field splitting: in this case, the ions in the crystal can be simply represented by point charges that interact with the valence electrons of the central atom.

Consider, for instance, an open-shell $3d$ transition metal atom in an octahedral environment comprised of negatively charged ligands (Fig. 2.1). Electrostatic repulsion between the valence d-electrons and the surrounding point-charges will result in a crystal field splitting: for example, the d_{z^2} and $d_{x^2-y^2}$ orbitals will experience strong Coulomb

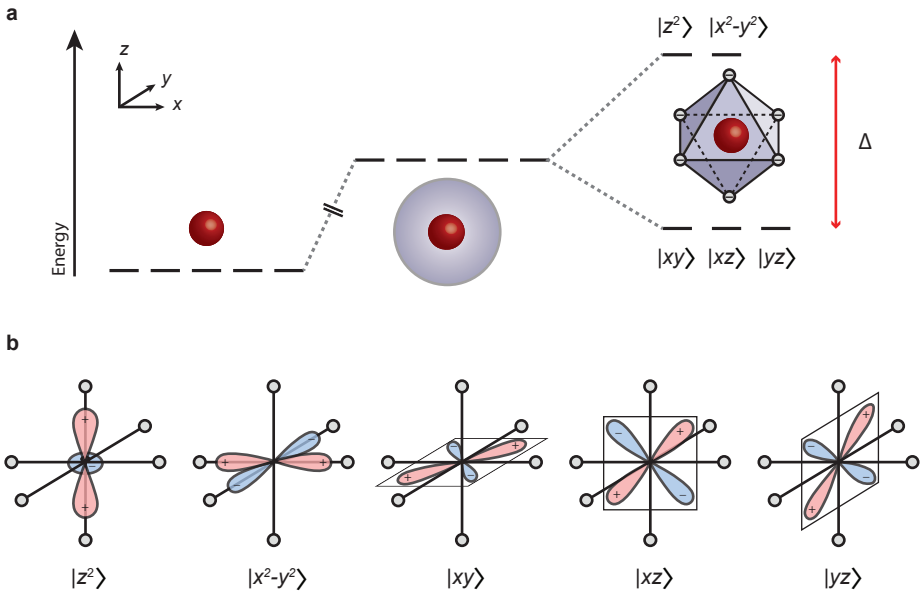

Figure 2.1: **Effects of a spherical or octahedral crystal field on a 3d transition metal. a** The degenerate valence d-orbitals of a free 3d transition metal. The degeneracy is preserved in a rotationally invariant crystal field, but the levels are raised in energy; this is not the case for an octahedral coordination, in which a crystal field splitting (Δ) separates the $|z^2\rangle$ and $|x^2-y^2\rangle$ states from the $|xz\rangle$, and $|yz\rangle$ states. Adapted from [57]. **b** Illustration of the electron densities associated with the d-orbitals of a free atom. The point-charge distribution associated with an octahedral environment is schematically represented with grey circles.

repulsion, as the lobes of their corresponding wave functions directly point toward the neighbouring anions in this environment (Fig. 2.1b). On the other hand, the d_{xy}, d_{xz}, and d_{yz} states are characterized by electron densities directed away from the surrounding negative point-charges, meaning they experience significantly weaker repulsion. This interaction acts to lower the energy of the d_{xy}, d_{xz}, and d_{yz} orbitals relative to that of the d_{z^2} and $d_{x^2-y^2}$ orbitals.

In addition to the point-charge contribution, the covalency between the d-electrons and the neighbouring ligands can play an important role in understanding the effects of the crystal environment. For such considerations, it is insufficient to regard the crystal as merely comprised of point-charges—the particular valency and orbital nature of the surrounding ligands becomes relevant in this framework, which is often referred to as ligand field theory. For example, consider a scenario in which the neighbouring ligands are characterized by 2p valence orbitals; in this case, the $d_{x^2-y^2}$ orbital will strongly overlap with the p orbitals oriented along the x or y axes, engendering a large hopping matrix element between the two (see Fig. 2.2a). This hybridization between the p and d orbitals results in the formation of bonding and antibonding states (Fig. 2.2c), with an energy splitting determined by the degree of overlap between the valence orbitals. Of course, this overlap depends on the symmetry and spatial orientation of the specific d and p orbitals in question: for instance, the d_{xy} orbital will form weak π bond with

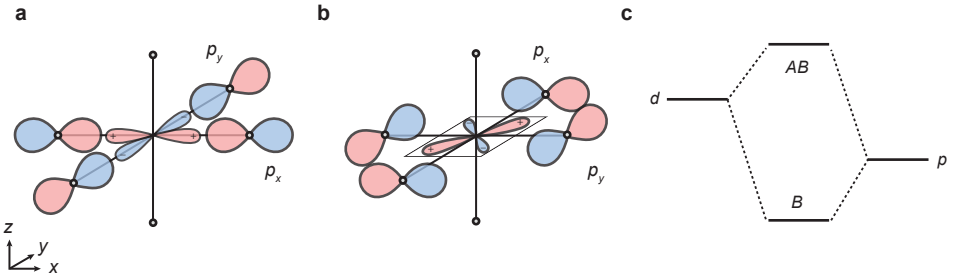

Figure 2.2: **Simplified illustration of ligand field effects in an octahedral coordination. a, b** Spatial orientation of the $|x^2 - y^2\rangle$ (**a**) and $|xy\rangle$ (**b**) orbitals of a $3d$ metal, with the relevant p-orbitals of the surrounding ligands illustrated. The overlap between the central atom and surrounding ligands will result in σ (**a**) or π (**b**) hybridization. **c** Illustration of the ligand field splitting due hybridization between a single d and p level, and the resultant bonding (B) and antibonding (AB) levels. Figure adapted from [55].

the orbitals shown in Fig. 2.2b, but will be orthogonal to the ligand orbitals shown in Fig. 2.2a.

ORBITAL QUENCHING

A common consequence of crystal field splitting is orbital momentum quenching—an effect in which the orbital moment of an atom tends to zero when it's placed in a crystal environment. Qualitatively, this occurs because the potential the atom experiences in the crystal breaks rotational invariance. A more rigorous description can be given by considering the five wave functions corresponding to the d-orbitals: these atomic orbitals are linear combinations of the orbital angular momentum eigenstates, also known as the spherical harmonics $Y_\ell^{m_\ell}$, and take the form:

$$|xy\rangle = \frac{i}{\sqrt{2}}\big(|-2\rangle - |2\rangle\big), \qquad |x^2-y^2\rangle = \frac{1}{\sqrt{2}}\big(|-2\rangle + |2\rangle\big),$$
$$|xz\rangle = \frac{1}{\sqrt{2}}\big(|-1\rangle - |1\rangle\big), \qquad |yz\rangle = \frac{i}{\sqrt{2}}\big(|-1\rangle + |1\rangle\big),$$
$$|z^2\rangle = |0\rangle,$$

where we have denoted the orbital angular momentum states with the associated magnetic number $|m_\ell\rangle$. Note that the expectation value of the orbital momentum is strictly zero for these atomic orbitals, as each one is a linear combinations of $\pm m_\ell$ states. However, in a spherically symmetric environment—where the degeneracy of all the d-levels is preserved—you can freely make a change of basis between the orbital angular momentum states and the atomic orbitals. In other words, the presence of rotational invariance ensures that the L_z and $\mathbf{L}^2$ orbital angular momentum operators commute with the Hamiltonian, i.e. $[\mathbf{L}^2, H] = 0$, $[L_z, H] = 0$, where the orbital angular momentum operator is defined as $\mathbf{L} = (L_x, L_y, L_z)$.

However, if this degeneracy is (partially) lifted, then such a change of basis may not be allowed, possibly leading to a quenched orbital momentum ($\langle L_z\rangle = 0$) for the eigenstates of the Hamiltonian. For instance, consider the splitting between the atomic d-levels in an octahedral environment composed of point-charges (Fig. 2.1a): as we saw,

this will result in two degenerate states $|z^2\rangle$ and $|x^2-y^2\rangle$ that are higher in energy than the three fold degenerate states, $|xy\rangle$, $|xz\rangle$, and $|yz\rangle$. In the lower energy states, the degenerate $|xz\rangle$ and $|yz\rangle$ states can be written in terms of the orbital momentum eigenstates:

$$|1\rangle = -\frac{1}{\sqrt{2}}(|xz\rangle - i|yz\rangle) \qquad |-1\rangle = -\frac{1}{\sqrt{2}}(|xz\rangle - i|yz\rangle),$$

meaning that the orbital moment is well-defined in this case, i.e. $L_z|\pm 1\rangle = \pm\hbar|\pm 1\rangle$ [55]. However, the energy splitting between $|xy\rangle$ and $|x^2-y^2\rangle$ means that these states cannot be written in terms of a single orbital angular momentum eigenstate—as such, $\langle L_z\rangle = 0$ and the orbital momentum is said to be quenched. In other words, orbital states composed of the same $\pm m_\ell$ states contribute to the angular momentum only if the one such orbital can rotationally transformed into the other (degenerate) orbital; however, if there is an energy cost associated with this rotation (i.e. the orbitals are not degenerate), then the orbital momentum is quenched on those states.

In general, crystal field effects can also lend the orbital moment a preferred direction. For instance, in the simple octahedral coordination considered here, we saw that the $|xy\rangle$, $|xz\rangle$, and $|yz\rangle$ states form an effective $\tilde{\ell} = 1$ triplet ($m_{\tilde{\ell}} = 0, \pm 1$), whereas the orbital momentum of the higher energy doublet is quenched. As we will see in the following section, the crystal field effects on the orbital momentum can carry consequences for the spin momentum as well, since these two magnetic degrees of freedom may be coupled via spin-orbit interaction.

2.1.2. SPIN-ORBIT INTERACTION

Spin-orbit coupling arises due to the relativistic interaction between the electron's spin and orbital momentum: in the inertial frame, the orbiting nucleus constitutes a current that generates an effective magnetic field at the origin. This magnetic field interacts with the electron spin at rest, which results in a coupling between the spin and orbital momentum. This interaction can be described by [53, 55, 56, 58]:

$$H_{\mathrm{SO}} = \lambda \mathbf{L}\cdot\mathbf{S}, \tag{2.1}$$

where $\mathbf{L}$ and $\mathbf{S}$ are the orbital momentum and spin operators, respectively, and λ is the spin-orbit coupling constant. The above expression assumes that the individual electron spins ($\mathbf{s}_i$) can be summed to form a total spin momentum $\sum_i \mathbf{s}_i = \mathbf{S}$; analogously, the total orbital momentum is approximated by the sum of the individual orbital moments, whereby $\sum_i \boldsymbol{\ell}_i = \mathbf{L}$—this is the so-called Russell-Saunders scheme, which can be applied to light atoms (atomic number $Z < 30$, where $\lambda \sim Z^2$), where the spin-orbit interaction is sufficiently weak [53, 55].

An important consequence of LS coupling is that it generates total angular momentum states $\mathbf{J} = \mathbf{L} + \mathbf{S}$, meaning that states with a specific orbital and spin momentum are split in energy according to the total angular momentum. In other words, the spin and orbital momentum are not separately conserved in the presence of the spin-orbit coupling ($[\mathbf{L}, H] \neq 0$, $[\mathbf{S}, H] \neq 0$), whereas the total angular momentum is conserved ($[\mathbf{J}, H] = 0$). Often the spin-orbit interaction can be treated as a perturbation, which means one can consider the magnitudes of the spin and orbital momentum to be conserved as well $[\mathbf{S}^2, H] = 0$, $[\mathbf{L}^2, H] = 0$) [56].

To better elucidate this, consider the square of the total angular momentum:

$$\mathbf{J}^2 = \mathbf{L}^2 + \mathbf{S}^2 + 2\mathbf{L}\cdot\mathbf{S}, \tag{2.2}$$

where J can take values from $L+S$ to $|L-S|$, and the multiplicity of each level is given by $2J+1$. From Eq. 2.2, we can deduce the energy contribution of the spin-orbit term, $\langle\psi|H_{SO}|\psi\rangle$:

$$\langle\lambda\mathbf{L}\cdot\mathbf{S}\rangle = \frac{\lambda}{2}\left[J(J+1) - L(L+1) - S(S+1)\right]. \tag{2.3}$$

This contribution to the multiplet structure is often treated using a perturbative approach—or even neglected—when describing open-shell, isolated $3d$ transition metals, where $\lambda \sim 50$ meV [59].

CRYSTAL-FIELD AND SPIN-ORBIT COUPLING

In the above description of the spin-orbit interaction, we implicitly assumed L and J to be good quantum numbers—strictly speaking, this is not the case for an atom in a crystal environment. This is a particularly relevant consideration for $3d$ transition metals, where the spin-orbit coupling is typically much smaller than the crystal field splitting, meaning the crystal field cannot be treated pertubatively. However, it is usually possible to define an effective orbital momentum in such cases, which allows for a straightforward understanding of spin-orbit interactions.

Consider the crystal-field split triplet and doublet states for an atom in a octahedral coordination (Fig. 2.1a): the lower energy triplet has an effective orbital momentum $\tilde{\ell} = 1$, whereas the orbital momentum is quenched in the higher energy doublet. The spin-orbit interaction does not act on states with $\langle L_z\rangle = 0$ to first order—higher-order effects are still possible, and it is precisely these effects that typically generate single-site magnetic anisotropy in atoms with a quenched orbital moment [58]. The spin-orbit interaction is more important for the triplet states, where it can act to first order via $\tilde{\lambda}\tilde{\boldsymbol{L}}\cdot\mathbf{S}$, where $\tilde{\lambda}$ is an effective spin-orbit coupling and $\tilde{\boldsymbol{L}} = \sum_i \tilde{\boldsymbol{\ell}}_i$.

2.1.3. ZEEMAN SPLITTING

The Zeeman effect describes the energy level splitting experienced by an atom in a uniform external field $\mathbf{B}$, which occurs due to the interaction between the atom's net magnetic moment and the external magnetic field. For a single electron, this effect can be described by accounting for the orbital magnetic moment ($\boldsymbol{\mu}_\ell = -\mu_B\boldsymbol{\ell}$, where μ_B is the Bohr magneton) and the spin magnetic moment ($\boldsymbol{\mu}_s = -g_e\mu_B\boldsymbol{s}$, where $g_e \approx 2$ is the anomalous gyromagnetic factor) in defining the total magnetic moment ($\boldsymbol{\mu} = \boldsymbol{\mu}_\ell + \boldsymbol{\mu}_s$). In the Russell-Saunders framework ($\boldsymbol{L} = \sum_i \boldsymbol{\ell}_i$, $\boldsymbol{S} = \sum_i \boldsymbol{s}_i$), this can be readily extended for multi-electronic atoms to arrive at a general description of the Zeeman contribution to the Hamiltonian:

$$H_Z = -(\boldsymbol{\mu}_L + \boldsymbol{\mu}_S)\cdot\mathbf{B} = \mu_B(\mathbf{L} + 2\mathbf{S})\cdot\mathbf{B}. \tag{2.4}$$

If this interaction term is smaller than the spin-orbit coupling, then the orbital and spin momenta are not separately conserved and $\mathbf{L}$ and $\mathbf{S}$ do not commute with the Hamiltonian—this is the so-called weak field limit. In this regime, the Zeeman correction to the energy can be determined using first order perturbation theory:

$$E_Z = \mu_B\langle\mathbf{L} + 2\mathbf{S}\rangle\cdot\mathbf{B} \tag{2.5}$$

Since the total momentum is conserved, it is helpful to reframe the expectation value above in terms of J, such that $\mathbf{L}+2\mathbf{S}=\mathbf{J}+\mathbf{S}$, and consider the projection of of the spin momentum onto the total angular momentum:

$$\langle \mathbf{L}+2\mathbf{S}\rangle = \left\langle \left(1+\frac{\mathbf{S}\cdot\mathbf{J}}{J^2}\right)\mathbf{J}\right\rangle = \left[1+\frac{J(J+1)-L(L+1)+S(S+1)}{2J(J+1)}\right]\langle \mathbf{J}\rangle. \tag{2.6}$$

The term in square brackets is known as the Landé g-factor, typically denoted by g_J. Thus, the Zeeman energy contribution in the weak-field limit can be written as:

$$E_Z = \mu_B g_J m_j B, \tag{2.7}$$

where B is the magnitude of the external field along the quantization axis.

2.1.4. EFFECTIVE HAMILTONIANS

An effective Hamiltonian framework is often adopted to predict and understand the magnetic properties of single atoms in a crystal environment: in this context, the relevant degrees of the freedom are the spin and the orbital momentum—or, in the presence of strong spin-orbit coupling, the total angular momentum. Here, we will restrict our focus to effective Hamiltonians specifically applied to surface-adsorbed magnetic atoms with relatively weak spin-orbit coupling. We will initially consider the case in which the orbital momentum of the adatom is quenched or largely diminished due to ligand field effects [48, 60, 61]. In this scenario, an effective spin Hamiltonian that accounts for the Zeeman splitting and the magnetic anisotropy induced by the surface is sufficient for describing the ground state multiplet of the adatom.

However, it is possible that the binding site symmetry and ligand field preserve the orbital moment—in which case the effects of the crystal field on the orbital moment and the role of the spin-orbit coupling have to be explicitly accounted for in order to map the ground state multiplet onto an effective Hamiltonian [46, 48, 62, 63]. We will first address the effective spin Hamiltonian, and from there expand our view to account for the effects of an unquenched orbital moment on the ground state multiplet.

EFFECTIVE SPIN HAMILTONIAN

One approach to describing the low energy physics of individual, surface-adsorbed atoms is by means of an effective spin Hamiltonian that only considers the spin degree of freedom [61, 64–66]. This means the relevant interaction terms are described within the subspace of the ground state spin [58]—a valid approach when the ligand field interaction quenches the orbital momentum, as often happens for surface-adsorbed atoms [30, 46, 48, 59, 61].

Magnetic anisotropy is the directional dependence of the local spin, and is responsible for conferring the spin with a preferred orientation in space—as such, it is a critical consideration in the description of an atom's spin states. This anisotropy arises from the interplay between the ligand field produced by the surface and the adatom's intrisic spin-orbit coupling: generally, the ligand field splitting lends the orbital moment a preferred orientation relative to the crystallographic axes, and this directionality is translated to the spin magnetic moment via higher-order spin-orbit interactions. In the context of

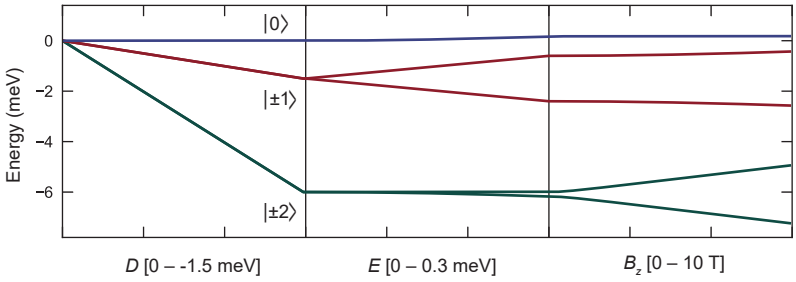

Figure 2.3: **Multiplet calculations using an effective spin Hamiltonian** Energy levels obtained by diagonalization of the effective spin Hamiltonian ($S = 2$), as a function of the uniaxial magnetic anisotropy strength D, the transverse magnetic anisotropy E, and the external magnetic field B_z. The energy scale is defined relative to the ground state energy. The uniaxial anisotropy breaks the degeneracy $(2S+1)$ between the spin states according to their m_s quantum number: since $D < 0$, the lowest energy doublet corresponds to the $|m_s\rangle = |\pm 2\rangle$ states; the second lowest energy doublet corresponds to the $|\pm 1\rangle$ states; the highest energy level is the $|0\rangle$ state. The energy splitting between the lowest and highest energy states is given by $4D$. The transverse anisotropy mixes the $|m_s\rangle$ states, and the resulting levels are no longer eigenstates of the S_z operator. The Zeeman interaction splits the levels according to their net magnetic moment and the strength of the field.

an effective spin Hamiltonian, the combined role of the ligand field splitting and spin-orbit interaction is condensed into descriptions of the magnetic anisotropy, which can be written in terms of a complete set of high-order spin operators:

$$\sum_{k=2,4,6} \sum_{q=-k}^{k} B_k^q \mathbf{O}_k^q \tag{2.8}$$

where $\mathbf{O}_k^q$ are the hermitian Stevens operators applied to the spin eigenstates, and B_k^q are their associated real coefficients [53]. However, these anisotropy coefficients are generally difficult to determine, even from first principles calculations [67–69]. A simplified approach towards describing the magnetic anisotropy is to solely consider the lowest order uniaxial ($B_2^0\mathbf{O}_2^0$) and in-plain ($B_2^2\mathbf{O}_2^2$) anisotropy terms—the magnitudes of which can be deduced from STM-based experimental techniques, such as inelastic electron tunneling spectroscopy (see section 3.2.3).

This phenomenological approach towards the single spin Hamiltonian has been successfully applied to describe the spin states of transition metals [61, 70–74], and in its standard form is written as:

$$H = -g\mu_B \mathbf{B}\cdot\mathbf{S} + DS_z^2 + E(S_x^2 - S_y^2), \tag{2.9}$$

where g is the (isotropic) g-factor. The first term of this Hamiltonian describes the Zeeman effect, whereas the second and third terms are phenomenological representations of the uniaxial and transverse magnetic anisotropies, the strength of which is characterized by D and E, respectively [59, 64].

As shown in Fig. 2.3, the uniaxial magnetic anisotropy splits the zero-field degeneracy of the spin states according to spin's projection along the quantization axis (z): for instance, a negative uniaxial magnetic anisotropy ($D < 0$) means that states with a

maximal projection along the quantization axis are preferred, thereby engendering a so-called easy axis. Conversely, a positive uniaxial magnetic anisotropy ($D > 0$) indicates that states with minimal projection along the z-axis lie lower in energy, resulting in an easy-plane orthogonal to the quantization axis. The transverse term, on the other hand, is typical of adsorption sites with C_{2v} symmetry and acts to mix states with different m_s quantum numbers—this becomes evident when we rewrite this contribution in terms of the raising and lowering operators, such that $S_x^2 - S_y^2 = \frac{1}{2}(S_+^2 + S_-^2)$.

EFFECTIVE SPIN-ORBIT HAMILTONIAN

In the context of surface-adsorbed magnetic atoms with an unquenched orbital moment, the ligand field is incorporated into the effective Hamiltonian to reflect the symmetry of the adatom binding site via a set of effective ligand field parameters that are applied to the orbital momentum eigenstates [46–48]. Furthermore, the spin-orbit term is explicitly included—an important distinction, since this interaction can induce a splitting that is linear in λ, thereby engendering an enhanced magnetic anisotropy. The general form of the effective spin-orbit Hamiltonian is given by:

$$H = H_{\mathrm{LF}} + \lambda \mathbf{L}\cdot\mathbf{S} + \mu_B(\mathbf{L} + 2\mathbf{S})\cdot\mathbf{B} \tag{2.10}$$

The ligand field contribution to the Hamiltonian, H_{LF}, is specific to the surface and the adsorption site in question; typically, however, it contains terms that account for the axial and transverse contributions to the ligand field [46–48]:

$$H_{\mathrm{LF}} = B_2^0\mathbf{O}_2^0 + B_4^0\mathbf{O}_4^0 + B_4^4\mathbf{O}_4^4. \tag{2.11}$$

In this case, the Stevens operators are applied to the eigentates of the orbital momentum.

The effective Hamiltonian framework is a powerful conceptual tool, as it provides a relatively simple framework for understand the magnetism of single atoms, and can be readily extended to include spin-spin interactions. In the following, we will be shifting gears away from magnetism: rather, we will discuss the tight-binding method, in which we will consider the single-electron Hamiltonian for describing the electronic structure of lattices.

2.2. DESCRIBING ELECTRONIC STRUCTURE: THE TIGHT-BINDING METHOD

A quantitative description of the electronic structure of a solid can be obtained by viewing it as a structured array of weakly interacting atoms—this is the framework of the tight binding method. In this case, the interaction (or overlap) between neighbouring sites is sufficient to necessitate corrections to the description of isolated atoms, but not enough to render the atomic wave functions extraneous [75]. This approximation is well-suited to the description of insulators or to more localized electrons in metals, such as d-level electrons in transition metal atoms.

We will outline the general framework of tight binding in its simplest form, neglecting the effects of spin-orbit coupling and electron-electron interactions. This approach

makes use of the single atom Hamiltonian as its starting point [75, 76]:

$$H_{\text{at}} = -\frac{\hbar^2\nabla^2}{2m_e} + V_{\text{at}}(\mathbf{r}), \tag{2.12}$$

where m_e is the electron mass and V_{at} is the one-electron atomic potential. The single particle Hamiltonian of the solid can be phrased in terms of H_{at}:

$$H_{\text{s}} = -\frac{\hbar^2\nabla^2}{2m_e} + V_{\text{at}}(\mathbf{r}) + \sum_{\mathbf{R}\neq 0} V_{\text{at}}(\mathbf{r}-\mathbf{R}), \tag{2.13}$$

$$= H_{\text{at}} + v(\mathbf{r}), \tag{2.14}$$

where we have considered that every point $\mathbf{R}$ of the Bravais lattice hosts an atom of the same type. The first term in the Eq. 2.13 accounts for the kinetic energy of the single electron; the second term is the potential at the origin ($\mathbf{R} = 0$); and the third term accounts for the potential of the rest of the solid, $v(\mathbf{r}) = \sum_{\mathbf{R}\neq 0} V_{\text{at}}(\mathbf{r}-\mathbf{R})$. Keeping in mind that the single particle states must abide by Bloch's theorem, we can approximate the wave function of the solid, $\psi_{n\mathbf{k}}(\mathbf{r})$, as a linear combination of the atomic wave functions on each lattice site:

$$\psi_{n\mathbf{k}}(\mathbf{r}) = \frac{1}{\sqrt{N}} \sum_{\mathbf{R}} e^{i\mathbf{k}\cdot\mathbf{R}} \phi_n(\mathbf{r}-\mathbf{R}), \tag{2.15}$$

where the nth atomic wave function, $\phi_n(\mathbf{r})$, is an eigenstate of the single atom Hamiltonian, i.e. $H_{\text{at}}\phi_n(\mathbf{r}) = E_n\phi_n(\mathbf{r})$; additionally, we have considered N lattice sites and normalized the wave function accordingly. The coefficient $e^{i\mathbf{k}\cdot\mathbf{R}}$ is determined by Bloch's condition, which necessitates that $\psi_{n\mathbf{k}}(\mathbf{r}+\mathbf{R}') = e^{i\mathbf{k}\cdot\mathbf{R}'}\psi_{n\mathbf{k}}(\mathbf{r})$.

To calculate the band structure $\varepsilon(\mathbf{k})$ arising from a single electronic level, we will only consider the Bloch state constructed from the same orbital at each site, such that $\psi_{\mathbf{k}}(\mathbf{r}) = \frac{1}{\sqrt{N}}\sum_{\mathbf{R}} e^{i\mathbf{k}\cdot\mathbf{R}}\phi(\mathbf{r}-\mathbf{R})$:

$$\varepsilon(\mathbf{k}) \int \psi^*_{\mathbf{k}}(\mathbf{r})\psi_{\mathbf{k}}(\mathbf{r})\,d\mathbf{r} = \int \psi^*_{\mathbf{k}}(\mathbf{r}) H_{\text{s}} \psi_{\mathbf{k}}(\mathbf{r})\,d\mathbf{r}, \tag{2.16}$$

$$= \frac{1}{N} \sum_{\mathbf{R},\mathbf{R}'} e^{i\mathbf{k}\cdot(\mathbf{R}-\mathbf{R}')} \int \phi^*(\mathbf{r}-\mathbf{R}') H_{\text{s}} \phi(\mathbf{r}-\mathbf{R})\,d\mathbf{r}, \tag{2.17}$$

$$= \frac{1}{N} \sum_{\mathbf{R}} e^{i\mathbf{k}\cdot\mathbf{R}} \int \phi^*(\mathbf{r}) H_{\text{s}} \phi(\mathbf{r}-\mathbf{R})\,d\mathbf{r}, \tag{2.18}$$

where we have made use of the arbitrariness of $\mathbf{R}'$: namely, the particular choice of $\mathbf{R}'$ does not affect the sum due to the assumed periodic boundary conditions of the solid—this has two implications: first, we can remove the double sum by realizing the sum over $\mathbf{R}'$ simply gives a factor N; second, we can arbitrarily set $\mathbf{R}' = 0$. This also applies to the normalization integral:

$$\int \psi^*_{\mathbf{k}}(\mathbf{r})\psi_{\mathbf{k}}(\mathbf{r})\,d\mathbf{r} = \frac{1}{N} \sum_{\mathbf{R},\mathbf{R}'} e^{i\mathbf{k}\cdot(\mathbf{R}-\mathbf{R}')} \int \phi^*(\mathbf{r}-\mathbf{R}')\phi(\mathbf{r}-\mathbf{R})\,d\mathbf{r} \tag{2.19}$$

$$= 1 + \sum_{\mathbf{R}\neq\mathbf{0}} e^{i\mathbf{k}\cdot\mathbf{R}} \int \phi^*(\mathbf{r})\phi(\mathbf{r}-\mathbf{R})\,d\mathbf{r} \tag{2.20}$$

Putting Eqs. 2.18 and 2.20 together, we arrive at [75]:

$$\varepsilon(\mathbf{k}) = \frac{\sum_{\mathbf{R}} e^{i\mathbf{k}\cdot\mathbf{R}} \int \phi^*(\mathbf{r}) H_s \phi(\mathbf{r}-\mathbf{R}) d\mathbf{r}}{1 + \sum_{\mathbf{R}\neq\mathbf{0}} e^{i\mathbf{k}\cdot\mathbf{R}} \int \phi^*(\mathbf{r})\phi(\mathbf{r}-\mathbf{R}) d\mathbf{r}}, \tag{2.21}$$

$$= E_n - \frac{\beta + \sum_{\mathbf{R}\neq\mathbf{0}} e^{i\mathbf{k}\cdot\mathbf{R}} \gamma(\mathbf{R})}{\left(1 + \sum_{\mathbf{R}\neq\mathbf{0}} e^{i\mathbf{k}\cdot\mathbf{R}} \mathfrak{s}(\mathbf{R})\right)}, \tag{2.22}$$

which describes how the atomic levels form bands when the constituent atoms are placed in a lattice. The above expression makes use of the following shorthands:

$$\beta = -\int \phi^*(\mathbf{r}) v(\mathbf{r}) \phi(\mathbf{r}) d\mathbf{r}, \tag{2.23}$$

$$\mathfrak{s}(\mathbf{R}) = \int \phi^*(\mathbf{r})\phi(\mathbf{r}-\mathbf{R}) d\mathbf{r}, \tag{2.24}$$

$$\gamma(\mathbf{R}) = -\int \phi^*(\mathbf{r}) v(\mathbf{r}) \phi(\mathbf{r}-\mathbf{R}) d\mathbf{r}. \tag{2.25}$$

The first integral, β, describes the shift in the atomic energy caused by the potentials of the surrounding atoms; the so-called overlap integral, $\mathfrak{s}(\mathbf{R})$, quantifies the degree of overlap between adjacent orbitals—this term is usually neglected for simplicity, and is strictly zero for an orthogonal choice of basis; lastly, $\gamma(\mathbf{R})$ is the interatomic Hamiltonian matrix element, which corresponds to the hopping integral t in second-quantization formalism.

2.2.1. APPLICATION TO AN *s*-VALENT DIMER

We will now apply the tight-binding description to a *s*-homovalent or *s*-heterovalent diatomic molecule. In this case, the single-particle Hamiltonian can be approximated by [77–79]:

$$H_d = -\frac{\hbar^2}{2m}\nabla^2 + V_A + V_B, \tag{2.26}$$

where we have phrased the effective total potential in terms of V_A and V_B, the atomic-centered potentials. We can write the molecular orbitals $\psi_{\mathrm{MO}}(\mathbf{r})$ as a linear combination of the atomic orbitals:

$$\psi_{\mathrm{MO}}(\mathbf{r}) = c_A \phi_A(\mathbf{r}) + c_B \phi_B(\mathbf{r}-\mathbf{R}), \tag{2.27}$$

where $\phi_{A,B}$ are eigenstates of the free-atom Hamiltonian for the two atomic centers. We can determine the energies of the molecular states in the usual way:

$$H_d|\psi_{\mathrm{MO}}\rangle = \varepsilon|\psi_{\mathrm{MO}}\rangle, \tag{2.28}$$

which readily yields the so-called tight-binding secular equation:

$$\begin{pmatrix} \mathcal{E}_{AA} & \gamma_{AB} \\ \gamma_{BA} & \mathcal{E}_{BB} \end{pmatrix} \begin{pmatrix} c_A \\ c_B \end{pmatrix} = \varepsilon \begin{pmatrix} 1 & \mathfrak{s} \\ \mathfrak{s} & 1 \end{pmatrix} \begin{pmatrix} c_A \\ c_B \end{pmatrix}, \tag{2.29}$$

where $\mathcal{E}_{AA,BB} = \int \phi_{A,B}(\mathbf{r}) H_d \phi_{A,B}(\mathbf{r}) d\mathbf{r}$ is the on-site energy of site A or B. The inter-site matrix element is $\gamma_{AB,BA} = \int \phi_{A,B}(\mathbf{r}) H_d \phi_{B,A}(\mathbf{r}) d\mathbf{r}$, and the overlap integral is $\mathfrak{s} = \int \phi_A \phi_B d\mathbf{r}$.

In general, the eigenvalues ε can be determined by solving the determinant:

$$\begin{vmatrix} \mathcal{E}_{AA} - \varepsilon & \gamma_{AB} - \varepsilon\mathcal{S} \\ \gamma_{BA} - \varepsilon\mathcal{S} & \mathcal{E}_{BB} - \varepsilon \end{vmatrix} = 0. \tag{2.30}$$

For the particular case of a homovalent dimer—in which the two atomic centers are equivalent ($\mathcal{E}_{AA} = \mathcal{E}_{BB} = \mathcal{E}$ and $\gamma_{BA} = \gamma_{AB} = \gamma$)—the eigenenergies are simply given by:

$$\varepsilon_{\pm} = \frac{\mathcal{E} \pm \gamma}{1 \pm \mathcal{S}}, \tag{2.31}$$

corresponding to the energies of the bonding and anti-bonding molecular orbitals.

3

EXPERIMENTAL BACKGROUND AND METHODS

The scanning tunneling microscope is a powerful tool for high resolution surface imaging and characterization. When operated at sufficiently low temperatures, the probe tip can be used to manipulate individual atoms and to coordinate them on various binding sites or to construct atomic assemblies, the electronic and magnetic properties of which can be locally probed with scanning tunneling spectroscopic techniques. In this chapter, we will discuss the basics of this form of microscopy, such as obtaining spatially resolved topographic maps, as well as the connection between the tunneling current and the differential conductance to the local sample density of states. Furthermore, we will delineate the experimental implementation and governing principles behind several spectroscopic methods used in this thesis—such as spin-polarized and inelastic electron tunneling spectroscopy—and explain the mechanisms behind vertical and lateral atom manipulation.

3.1. SCANNING TUNNELING MICROSCOPY

The spatial resolution of traditional optical microscopy methods is determined by the diffraction limit, which is set by the wavelength of visible light; attempts to surpass this constraint spurred the invention of different forms of microscopy, such as the electron microscope [80] and the field-ion microscope [81], the former of which led to the first atomically resolved images in the early 1950s. The scanning tunneling microscope (STM) was introduced some 30 years later [82], constituting a significant paradigm shift in the study of matter at the smallest length scales [83–87].

The basic principle governing this type of microscopy is quantum tunneling of electrons: a metal tip is brought sufficiently close to a sample surface, and the resultant wave function overlap leads to a net measurable current under an applied bias voltage across the tip-sample junction. More specifically: when, for instance, a positive bias voltage V is applied to the sample with respect to the tip, the sample Fermi level is shifted down by $-eV$ with respect to the tip Fermi level, resulting in net directed electron tunneling from occupied states on the tip side into empty states on the sample side (see section 3.2).

The tunneling current depends on several factors [88–92], such as the tip position, the tip and sample electronic densities of states, and the transmission through the tunnel barrier, which is itself determined by considerations such as the tip-sample distance, tip shape, as well as the tip and sample work-functions [86, 93–95]. The atomic spatial resolution afforded by STM is due to the exponential dependence of the tunnel current on the tip-sample distance: a few angstroms change in tip-height can cause an order of magnitude change in the tunnel current. Another key ingredient is the tip position relative to the sample surface, which is finely controlled by piezoelectric elements: as the tip is displaced across the sample surface, changes in the sample density of states or surface height can be closely monitored by the accompanying variations in the tunnel current.

In practice, the tip-sample distance is regulated by a feedback loop. As such, obtaining topographic maps of a surface amounts to raster scanning the tip across the area of interest, and recording the change in tip-height needed to maintain a constant current—this type of scan is performed in so-called *constant current mode*. Conversely, if the tip-sample distance is not regulated, the surface topography can be mapped by tracing the variations in the measured current—this is referred to as *constant height mode*. Such topographic maps can allow us to closely trace the surface corrugation and detect adsorbed atoms or molecules. Finally, we note that it is usually preferable to obtain topographic maps in constant-current mode as the engagement of the feedback loop helps to prevent tip crashes; on the other hand, constant-height mode can be advantageous in scenarios in which it is necessary to remove the contribution of a varying tip height to the current.

Aside from its imaging and resolution capabilities, scanning tunneling microscopy can also provide spectroscopic information about the local density of states [89, 90, 92, 96, 97] (section 3.2), probe vibrational modes or spin excitations in single atoms [94, 98, 99] (sections 3.2.3 and 3.2.4), and allow for the controlled manipulation of surface-bound adatoms or molecules [100–102] (section 3.3).

3.2. SCANNING TUNNELING SPECTROSCOPY

There are several measurement techniques employed in STM-based spectroscopic studies, such as time-resolved spectroscopy [103–105], current-distance spectroscopy [96, 97, 106], single-electron tunneling spectroscopy [107], amongst others. Here, we will focus on current-voltage spectroscopy, which allows us to trace variations in the tunnel current I and differential conductance $\mathrm{d}I/\mathrm{d}V$ as a function of the applied bias voltage. Usually, the most useful quantity here is not the current itself, but rather the differential conductance, which maps more directly to the local density of states [89, 92, 96, 97] and can be used to detect the spin excitations in atoms, assembled atomic structures, or molecules [30, 64, 98, 108–110].

To demonstrate the connection between the measured conductance and the sample density of states, we turn to a theoretical description of the tunnel current. This can be obtained by considering the tip and sample wave functions to be independent entities that describe two undisturbed systems. The wave function of the entire system can be evaluated by treating the tip potential, $V_t(\tau)$, as a time-dependent perturbation, namely [90]:

$$i\hbar\frac{\partial\psi_\nu}{\partial\tau} = \left[\frac{-\hbar^2}{2m}\frac{\partial^2}{\partial x^2} + V_s + V_t(\tau)\right]\psi_\nu, \tag{3.1}$$

where V_s denotes the sample potential and ψ_ν is the wave function of the ν-th state. In this framework, the rate of electron transfer can be determined from Fermi's golden rule [111], where the probability that an electron tunnels from a state ψ_μ to a state ψ_ν is:

$$\frac{2\pi}{\hbar}|M_{\mu\nu}|^2\delta(E_\nu - E_\mu), \tag{3.2}$$

where E_ν (E_μ) is the energy of the ν-th (μ-th) state and $M_{\mu\nu}$ is the transition probability matrix element. We are implicitly only considering elastic tunneling in the above expression: the Dirac delta function indicates that tunneling can only occur between states at the same energy.

An expression can be derived for the tunneling current by neglecting interactions between tunneling electrons; in this case, the current flowing from the tip to sample under an applied bias V can be expressed as [91]:

$$I_{t\to s} = \frac{4\pi e}{\hbar}\int_{-\infty}^{\infty}\rho_t(E-eV)\rho_s(E)f_t(E-eV)(1-f_s(E))|M_{\mu\nu}|^2 dE, \tag{3.3}$$

where e is the electron charge, $f(E) = (1+\exp[(E-E_f)/k_BT)]^{-1}$ is the Fermi-Dirac distribution function (k_B: Boltzmann constant; T: temperature; E_f: Fermi energy), and ρ_s and ρ_t are the sample and tip densities of states, respectively. Note that we have defined the energies E relative to the Fermi energy. The current in Eq. 3.3 is determined by the tip and sample densities of states, and only accounts for tunneling from the occupied states on the tip side ($f_t(E-eV)$) to the unoccupied states on the sample side ($1-f_s(E)$).

The total tunneling current I can be determined by accounting for the current in both directions, i.e. $I = I_{t\to s} + I_{s\to t}$, arriving at:

$$I = \frac{4\pi e}{\hbar}\int_{-\infty}^{\infty}\rho_t(E-eV)\rho_s(E)\left(f_t(E-eV) - f_s(E)\right)|M_{\mu\nu}|^2 dE. \tag{3.4}$$

Different frameworks have been developed for evaluating the tunneling matrix element $M_{\mu\nu}$ [88, 89, 92], with the simplest being the one-dimensional Wentzel-Kramer-Brillouin approach where the transmission through the tunnel barrier determines $M_{\mu\nu}$:

$$|M_{\mu\nu}|^2 = \exp\left[\frac{-2z}{\hbar}\sqrt{m_e(\phi_t + \phi_s - eV + 2E}\right], \tag{3.5}$$

where z is tip-sample distance, m_e is the electron mass, and ϕ_t and ϕ_s are the tip and sample work functions, respectively. It should be noted that the above expression is only valid in the low-bias regime, where the tunnel junction can be approximated by a rectangular potential barrier—this will become relevant in chapter 7. Additionally, substituting Eq. 3.5 into the expression for the overall current (Eq. 3.4), we can see that the states closest to the tip (sample) Fermi energy contribute the most to the current under a positive (negative) voltage applied to the tip—this is a particularly relevant consideration at high applied bias voltages, as we will see in chapter 7.

While the current contains information about the local density of states, the differential conductance is a better direct measure of it. To demonstrate this, we will consider the low temperature limit ($T \ll eV/k_B$), where the Fermi-Dirac distributions can be approximated as step functions. In this case, Eq. 3.4 reduces to:

$$I \propto \int_0^{eV} \rho_t(E - eV)\rho_s(E)|M_{\mu\nu}|^2 dE. \tag{3.6}$$

It follows from this expression that the differential conductance at an energy eV is:

$$\frac{\mathrm{d}I}{\mathrm{d}V} \propto \rho_s(eV)\rho_t(0)|M_{\mu\nu}|^2 + \int_0^{eV} \rho_t(E - eV)\rho_s(E)\frac{\mathrm{d}|M_{\mu\nu}|^2}{\mathrm{d}V} + \int_0^{eV} \frac{\mathrm{d}\rho_t(E - eV)}{\mathrm{d}V}\rho_s(E)|M_{\mu\nu}|^2 \tag{3.7}$$

We will use two approximations to simplify the expression for the differential conductance further: firstly, we will assume the metal tip has a featureless density of states, such that $\mathrm{d}_V\rho_t = 0$. Secondly, we will assume the tunneling matrix element (Eq. 3.5) does not appreciably change in the interval of interest [90], meaning $\mathrm{d}_V M_{\mu\nu} = 0$; this is a valid approximation when the applied bias is small compared to the tip and sample work functions. With this, only the first term in the above expression remains:

$$\frac{\mathrm{d}I}{\mathrm{d}V} \propto \rho_s(eV)\rho_t(0)|M_{\mu\nu}|^2 \tag{3.8}$$

As such, the differential conductance obtained at a given bias voltage V is a direct probe of the local density of states of the sample at the energy eV.

3.2.1. LOCK-IN DETECTION & SPECTROSCOPIC MEASUREMENT MODES

The tunneling current and differential conductance can be measured concurrently by means of a lock-in detection scheme. While it is possible to simply record the current and numerically differentiate it to obtain the differential conductance, the lock-in method offers a much better signal-to-noise ratio. This technique relies on adding a small ac voltage (of amplitude V_m and frequency ω_m) to the dc bias voltage (V_{DC}), such

that the total voltage is $V = V_{\mathrm{DC}} + V_m \sin(\omega_m t)$. Typically, the frequency of the ac component (ω_m) is set to higher values than the regulation speed of the feedback loop, thereby ensuring the modulation does not influence constant-current images or spectroscopy.

The resultant tunnel current can be Taylor expanded to obtain

$$I \propto I\left(V_{\mathrm{DC}}\right) + I'\left(V_{\mathrm{DC}}\right) V_m \sin(\omega_m t) + \mathcal{O}(V_m^2),$$

where I' denotes the derivative with respect to the voltage, i.e. $\mathrm{d}I/\mathrm{d}V$. The modulation gives rise to a component of the total current that oscillates at the frequency ω_m and is proportional to the differential conductance $I'\left(V_{\mathrm{DC}}\right)$. This contribution to the current can be selectively measured via homodyne detection by means of a lock-in amplifier [112].

This technique makes use of phase-sensitive detection to recover the component of the input at the frequency of interest; to achieve this, the lock-in performs a multiplication (demodulation) of its input with a phase-shifted reference signal $V_r \cos(\omega_r t + \phi_r)$. The product of the multiplier is:

$$I\left(V_{\mathrm{DC}}\right) V_r \cos(\omega_r t + \phi_r) + \frac{1}{2} I'\left(V_{\mathrm{DC}}\right) V_m V_r \Big(\cos\left((\omega_m - \omega_r) t + \phi_m - \phi_r\right) - \cos\left((\omega_m + \omega_r) t + \phi_m + \phi_r\right)\Big),$$

where we have explicitly accounted for the phase of the modulation, ϕ_m. For homodyne detection, the frequency of the input and reference signal are the same ($\omega_r = \omega_m$), meaning that only the component of the input oscillating at the frequency of the reference is down-mixed to zero frequency. A low-pass filter applied to this product readily isolates the phase-sensitive dc term that is proportional to the differential conductance, $\frac{1}{2} I'\left(V_{\mathrm{DC}}\right) V_m V_r \cos\left(\phi_m - \phi_r\right)$. This allows for parallel measurements of the tunneling current and the differential conductance, while largely suppressing $1/f$ Shottky noise in the measurement of the latter [112].

The differential conductance can be measured in two spectroscopic modes: constant-height or constant-current. For the former, tip-sample distance is held constant while the bias voltage is swept, i.e. the feedback loop is opened, such that the height is not regulated to maintain a constant current. Conversely, the feedback is always engaged during constant-current measurements. Differential conductance spectra obtained at constant tip-height are more closely related to the density of states [113], but are not always an experimentally feasible option, for instance when spanning a wide voltage range (see chapter 7 for a more detailed discussion on the matter).

3.2.2. SPECTROSCOPIC MAPS

Heretofore, we have considered spectroscopy performed at a single point on the surface, where the differential conductance is traced as the applied bias voltage is ramped—in other words, we have considered the energy-dependent LDOS at one location. To gain insight into the spatial evolution of the differential conductance, it can be preferential to perform differential conductance maps, where we consider the spatial variation of the LDOS at a given energy: this entails scanning the surface at a set bias and simultaneously recording the differential conductance.

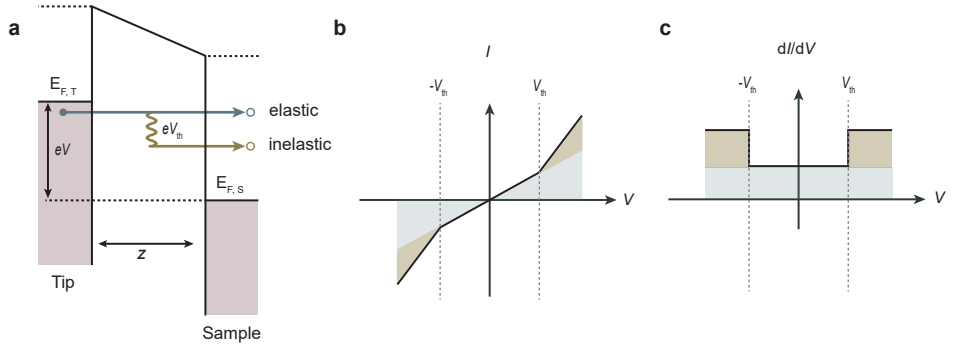

Figure 3.1: **Schematic of inelastic tunneling spectroscopy. a** Energy diagram of the STM junction, with the two electrodes—the tip and sample—separated by a distance z, with a bias voltage eV applied to the sample side. Electrons with sufficient energy ($eV > eV_{\text{th}}$) have two tunneling paths available to them: an elastic one, which occurs between two states at the same energy (green); or an inelastic one (yellow), in which the electrons lose part of their energy to excite the system. A filled circle denotes an occupied state, an empty circle an unoccupied one. **b** The elastic tunneling path (shaded, green) results in a linear increase in current with bias voltage; at the threshold voltage, a new inelastic tunneling path (yellow) opens, causing an increase in the total tunnel current. **c** This corresponds to steps in the differential conductance at the threshold voltage. Adapted from [99].

Similar to topographic maps, these types of measurements can be performed while maintaining a constant current or constant tip-sample distance; it is worth noting the former is more removed from the local density of states due to effects of the tip displacement during data acquisition [114–116]. Other measurement schemes, wherein maps are obtained by regulating the feedback on the differential conductance itself, have been proposed as a useful alternative when high surface corrugation renders constant-height measurements impractical [116].

3.2.3. INELASTIC ELECTRON TUNNELING SPECTROSCOPY

Thus far, we have limited our discussion on scanning tunneling spectroscopy (section 3.2) to elastic processes (Eq. 3.2), where tunneling occurs between states at the same energy. However, it is possible for tunneling electron to lose part of their energy in an inelastic tunneling event: for instance, the tunneling electron may couple to the spin or vibrational degrees of freedom of an adsorbate, and through inelastic scattering processes forfeit energy to induce excitations amongst these internal states [99, 117].

Inelastic electron tunneling spectroscopy (IETS) is a tool for detecting these inelastic processes with high spatial and energy resolution [109, 118]. Developed in the mid-1960s [119], IETS relies on the following basic principle: once tunneling electrons have sufficient energy to overcome the threshold energy eV_{th} associated with an inelastic process—be it a spin excitation [109] or vibrational mode [98, 119, 120]—a new transport channel opens, causing the overall tunneling probability to increase (see Fig. 3.1a, b). This means that for applied bias voltages exceeding the threshold voltage, wherein $V \gg V_{\text{th}}$, two transport paths—involving elastic or inelastic processes—are available to the tunneling electrons.

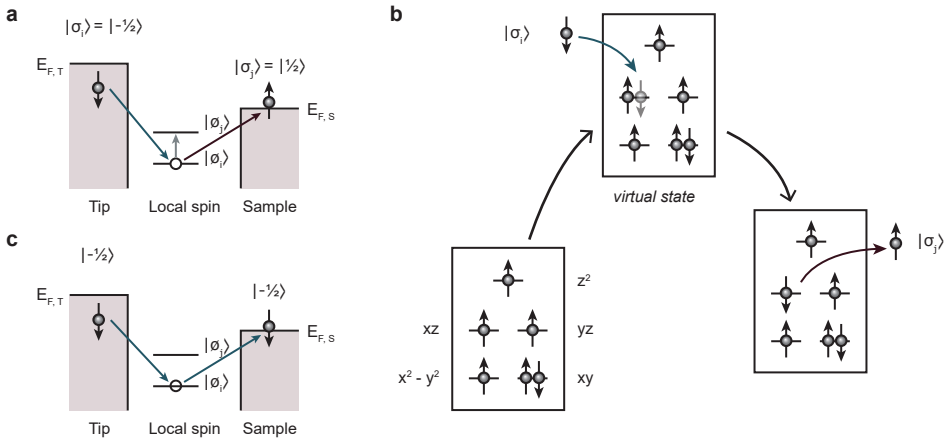

Figure 3.2: **Inelastic cotunneling mechanism for spin excitations. a** Inelastic cotunneling process: the tunneling electron transfers $\hbar$ of spin angular momentum to the local spin (corresponding to $\Delta\sigma = 1$), inducing an excitation of the local spin from the state $|\phi_i\rangle \rightarrow |\phi_j\rangle$ (corresponding to $\Delta m_s = -1$). Adapted from [64]. **b** An example of an inelastic cotunneling process for a surface-adsorbed spin experiencing a uniaxial crystal field, with six valence d-electrons; the quantization axis is along the z-direction. In the initial configuration, the expectation value of the spin along the quantization axis is $\langle S_z \rangle = 2$ (left). A spin-down electron tunnels from the tip onto the d_{xz} orbital of the surface-adsorbed spin, creating a short lived charged virtual state (middle). A spin-up electron tunnels from the same orbital to the substrate, rendering $\langle S_z \rangle = 1$ in the final configuration, thereby completing the $\Delta m_s = -1$ transition (right). **c** Elastic cotunneling process: the tunneling electron maintains the same spin state during the cotunneling process and so does the local spin, meaning that $\Delta\sigma = 0$, $\Delta m_s = 0$.

This new tunneling path leads to a kink in the overall tunnel current at the threshold voltage V_{th}, which translates to an upward step in the corresponding differential conductance (see Fig. 3.1b, c). The step height is determined by the cross-section of the excitation process [121], whereas the step width is determined by intrinsic lifetime broadening and experimental conditions, such as the temperature and the amplitude of the lock-in modulation voltage [122, 123].

It should be noted that the framework presented here is only valid in the regime in which the lifetime of the excited states is shorter than the average time between two tunneling events, e/I—higher-order excitations and dynamical effects that we have not explicitly accounted for may occur otherwise [65, 124].

INELASTIC SPIN EXCITATIONS

Using inelastic spectroscopic methods to induce and detect species-specific spin excitations can be a powerful tool for chemically identifying adsorbates, but further interpreting the measured spectra requires understanding the underlying processes governing the spin excitations. Here, we will consider the elastic and inelastic tunneling paths through a local, surface-bound spin.

In general, tunneling processes through the local spin must conserve angular momentum—a principle that imposes selection rules for the spin transitions: the spin angular momentum of the local spin is allowed to change by $-\hbar$, 0, or $+\hbar$. To understand

this, we can model the exchange interaction between the tunneling electron and the localized spin in the usual way, $\hat{\mathbf{S}} \cdot \hat{\boldsymbol{\varsigma}}$, where $\hat{\mathbf{S}}$ and $\hat{\boldsymbol{\varsigma}}$ are the spin vector operators for the local spin and the tunneling electron spin, respectively [61, 64, 65]. Based on this interaction, the total transition intensity Y from the ith to jth eigenstate takes the form [61, 64, 65, 121]:

$$Y(\phi_j,\sigma_j,\phi_i,\sigma_i) = \left| \left\langle \phi_j,\sigma_j \left| \left(\hat{\mathbf{S}} \cdot \hat{\boldsymbol{\varsigma}} + u\hat{\boldsymbol{I}} \right) \right| \phi_i,\sigma_i \right\rangle \right|^2, \tag{3.9}$$

where u is a real constant that accounts for spin-independent elastic contributions (*i.e.*, $i = j$), and $|\phi_i,\sigma_i\rangle$ denotes the product state of the local spin $|\phi_i\rangle$ and tunneling electron spin $|\sigma_i\rangle$. The spin states are labelled by their m_s value; for example, the tunneling electron states are denoted by $\sigma_i = \langle \sigma_i | \hat{\varsigma_z} | \sigma_i \rangle$, rendering $\sigma_{i,j} = +1/2$ or $-1/2$ (here we use $\hbar = 1$ for ease, and we define the z-axis as the quantization direction). Expanding the inner product and rewriting the $\hat{S}_x$, $\hat{S}_y$ operators in terms of the lowering and raising spin operators, $\hat{S}_\pm = \hat{S}_x \pm i\hat{S}_y$, we find that:

$$Y(\phi_j,\sigma_j,\phi_i,\sigma_i) = \left| \left\langle \phi_j,\sigma_j \left| \left(\frac{1}{2}\left(\hat{S}_+\hat{\varsigma}_- + \hat{S}_-\hat{\varsigma}_+ \right) + \hat{S}_z\hat{\varsigma}_z + u \right) \right| \phi_i,\sigma_i \right\rangle \right|^2. \tag{3.10}$$

As such, the transition intensity is nonzero solely for transitions that conserve total angular momentum: for a tunneling electron, the raising and lowering operators $\hat{\varsigma}_\pm$ can, at most, cause a change of $\Delta\sigma = \pm 1$ in the spin angular momentum between the ith and jth state; consequently, the spin angular momentum of the local, surface-bound spin can in turn change by a maximum value of $\Delta m_s = \mp 1$. The remaining $\hat{S}_z\hat{\varsigma}_z$ term accounts for spin-dependent elastic tunneling paths.

The spin-dependent tunneling processes can be cast in the cotunneling framework, wherein electrons from the tip and substrate tunnel off and on orbital states in the local, surface-bound spin, possibly exchanging energy and orbital angular momentum in the process. This is schematically depicted in Fig. 3.2: in an inelastic process, the tunneling electron transfers $\hbar$ of angular momentum to the local spin, causing a change in the spin state of the tunneling electron and that of the local spin; in an elastic process, the tunneling electron and the local spin remain in the same spin state through the tunneling process.

3.2.4. SPIN POLARIZED MICROSCOPY

Spin-polarized microscopy [65, 95, 110, 125, 126] is a measurement technique in which a spin-dependent density of states of the tip and/or sample results in a spin polarized tunneling current. This spin-sensitivity in the current makes it possible to probe magnetic and spin-dependent physics in single spins [45, 65, 127, 128], measure spin relaxation times [105], detect long-range spin order [129], and visualize novel spin structures [130, 131].

We can conventionally describe the polarization of the tip and sample, P_t and P_s, by considering their respective spin-resolved densities of state, $\eta^{\uparrow}_{t,s}$ and $\eta^{\downarrow}_{t,s}$ at the Fermi

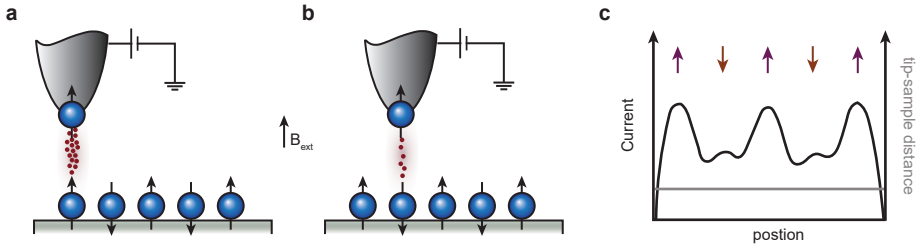

Figure 3.3: **Schematic of the effects of a spin-polarized current. a, b** A non-magnetic tip terminated with a magnetic atom in an external magnetic field, B_{ext}, resulting in the tip acquiring a spin-polarization parallel to the field. Consequently, the tunnel current will vary depending on whether the spin on the tip and the surface are aligned (**a**) or anti-aligned (**b**), resulting in a higher or lower net current, respectively. **c** Schematic illustration of the tunnel current (black line) obtained as the tip is laterally displaced along the length of the antiferromagnetically coupled chain (spin orientation of surface-bound atoms indicated by colored arrows): at a constant tip-sample distance (grey line), the effects of the spin-polarized tip density of states translates into variations in the tunnel current, which increases when the orientation of the tip and surface-bound spin are the same, and decreases otherwise.

energy [64, 126, 132]:

$$P_{t,s} = \frac{\eta^{\uparrow}_{t,s} - \eta^{\downarrow}_{t,s}}{\eta^{\uparrow}_{t,s} + \eta^{\downarrow}_{t,s}}. \tag{3.11}$$

The tunnel current then depends on the relative orientation of the tip and sample polarization (Fig 3.3), becoming spin polarized itself [132]:

$$I_{\text{sp}} = I_0(1 + P_t P_s \cos\varphi), \tag{3.12}$$

where I_{sp} is the spin-polarized current, I_0 is the non-polarized tunnel current, and φ is the angle between the tip and sample magnetization directions.

Preparation of probe tips for spin-polarized spectroscopy can present a challenge, as a suitable tip must concurrently offer spatial resolution down to the atomic scale and adequate spin-polarization. There are several well-established routes for achieving this [132]: it is possible to employ tips made from bulk magnetic material, use nonmagnetic tips coated with a thin film of magnetic material, or take advantage of nonmagnetic tips terminated by a cluster of magnetic atoms [20, 64]. Similarly, the sample polarization may assume many forms—for instance, it is possible to study a bulk magnetic materials, magnetic monolayers, or even single spins adsorbed onto a surface.

In this thesis, we will focus on the study of single spins probed by a nonmagnetic tip that hosts a magnetic cluster at its apex (see chapter 4), as shown in Fig 3.3. In this case, the tip preparation method typically entails picking up one or more magnetic atoms from the surface (see section 3.3 for details on atom manipulation) which come to define the tip apex, rendering it paramagnetic [20]. In an external magnetic field, the tip apex will acquire a net magnetization that tends to follow the direction of the applied field. This method of obtaining a spin-polarized tip offers many advantages, particularly in the study of single spins: it is a controlled, reversible process that allows for some degree of control over the orientation and strength of the tip magnetization [20, 64].

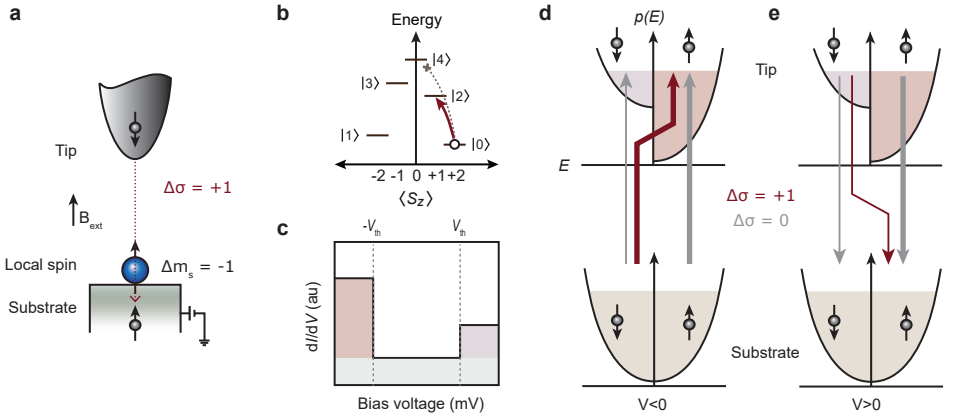

Figure 3.4: **Schematic of the effects of a spin-polarized current in inelastic electron tunneling spectroscopy.** **a** Schematic of an inelastic tunneling process considering a positive bias voltage applied to the sample. The local spin can be excited from its ground state due to an exchange interaction with the tunneling electron, resulting in a spin flip of $\Delta\sigma = +1$ in the tunneling electron and an excitation of $\Delta m_s = -1$ in the local spin. **b** An example schematic of the energy level diagram for the spin states of the surface-bound spin, considering $S = 2$, a large uniaxial magnetic anisotropy, and finite magnetic field; states are labelled in order of increasing energy. The inelastic $\Delta m_s = -1$ excitation (red arrow) changes the state of the local spin; other direct tunneling paths to higher energy states are forbidden (gray dotted line). **c** Schematic differential conductance spectrum, with steps at the threshold voltage corresponding to the $|0\rangle \rightarrow |2\rangle$ transition. The different contributions to the differential conductance are delineated by the shaded areas, showing the spin-dependent and spin-independent elastic components (grey), as well as the inelastic contributions at negative (orange) and positive (purple) voltage. **d, e** Spin-dependent densities of states $D(E)$ of the tip (top) and substrate (bottom), showing the spin-dependent inelastic (red) and elastic (grey) tunneling paths (relative strenght denoted by line thickness) considering a negative (**d**) or positive (**e**) applied bias voltage. Adapted from [64].

Additionally, it is worth mentioning that the description of the spin-polarization offered for the conventional case (Eq. 3.11) cannot be successfully applied to a local, surface-bound spin. In this case, the spin dependence arises due to the exchange interaction between the local spin and the tunneling electrons, $\hat{\mathbf{S}} \cdot \hat{\boldsymbol{\zeta}}$ (similar to section 3.2.3). As such, the spin-polarization of the local spin ρ_s can be expressed in terms of the spin transition intensities previously defined (Eq 3.9) [64]:

$$\rho_s = \frac{\sum_{\sigma_j} Y(\phi_j, \sigma_j, \phi_i, +1/2) - Y(\phi_j, \sigma_j, \phi_i, -1/2)}{\sum_{\sigma_i, \sigma_j} Y(\phi_j, \sigma_j, \phi_i, \sigma_i)}. \tag{3.13}$$

While this expression is analogous to Eq. 3.11, it is distinct in that it treats the local spin quantum mechanically and thus negates the need to assign it a spin-polarized density of states at the Fermi energy—a concept that breaks down in the face of quantum superpositions of spin states [64].

SPIN POLARIZED ELASTIC AND INELASTIC TUNNELING

In general, the probability for an electron to tunnel to a local spin in a certain spin state depends on the specific spin state of the tunneling electron—up $(+1/2)$ or down $(-1/2)$.

In spin-polarized spectroscopy, where the spin-resolved densities of states are not equivalent, this distinction in the tunneling probabilities can be resolved via the relative intensity with which spin transitions occur.

To better understand this, we can consider the case of a surface-adsorbed $S = 2$ spin with uniaxial magnetic anisotropy (defined as $\hat{z}$) in a finite external field applied along the quantization axis (see Fig 3.4a and b). For simplicity, we will neglect any thermal population in the first excited state $|1\rangle$ (zero temperature limit) and only consider transitions from the ground state. In this case, there are three tunneling paths contributing to the overall conductance: spin-independent elastic processes; spin-dependent elastic processes corresponding to the $\hat{S}_z\hat{\varsigma}_z$ component of the exchange interaction (Eq. 3.10); and spin-dependent inelastic processes corresponding to the $\hat{S}_+\hat{\varsigma}_- + \hat{S}_-\hat{\varsigma}_+$ exchange term.

In both spin-dependent processes the tunneling electron interacts with the local spin, but in an elastic process the local spin remains in the ground state ($\Delta m_s = 0$), whereas an inelastic tunneling event induces a transition to the excited state $|2\rangle$ ($\Delta m_s = -1$), as shown in Fig 3.4b. We note that transitions directly from the ground state to higher energy spin states, such as from $|0\rangle \rightarrow |4\rangle$, are forbidden due to the selection rules; additionally, higher order sequential excitations (e.g, from states $|0\rangle \rightarrow |2\rangle \rightarrow |4\rangle$) are neglected for simplicity (low current regime).

The spin polarized density of states in the tip significantly impacts the intensity with which the $\Delta m_s = -1$ transition is observed at positive or negative applied bias voltage, as shown in Fig 3.4c. Considering there is a greater density of $+1/2$ states in the tip at the Fermi energy ($P_t > 0$, Eq 3.11) and that the inelastic process here requires a spin-down electron, we can see that the inelastic contribution at negative bias (Fig 3.4d) will occur with a greater intensity than the same process occurring at positive bias (Fig 3.4e). This is due to the asymmetry in the spin-resolved density of states of the tip: when current flows from the tip ($V > 0$) the inelastic process involves the spin-down states in the positively spin-polarized tip; conversely, when current flows from the sample ($V < 0$) the spin-down states in the non-spin-polarized substrate and spin-up states in the spin-polarized tip are relevant.

This picture becomes more involved once the time between tunneling events is comparable or even shorter than the inherent relaxation time of the excited state. This is possible at high currents, where the probability for a tunneling electron to meet a spin in an excited state is sufficient to allow for excitations into higher energy spin states, resulting in so-called spin pumping [65]. Such processes cause an overall change in the time-average occupation of the spin states that is reflected in the conductance, and which can give rise to novel current-voltage characteristics [124].

In fact, spin-pumping can be used to control the orientation of the local spin: a spin-polarized current can cause a net spin transfer between the tunneling electrons and the local spin via inelastic processes, wherein the sign and efficiency of the spin transfer is determined by the direction and magnitude of the tunnel current, respectively [65, 127]. Consider the example depicted in Fig 3.4a and b, where the tip magnetic moment is parallel to the easy axis of the local spin and $P_t > 0$; and, assume that the first excited state $|1\rangle$ has some finite thermal occupation at equilibrium, meaning inelastic transitions from $|1\rangle \rightarrow |3\rangle$ ($\Delta m_s = +1$) can occur. At negative bias voltage, inelastic transitions induced by the spin-down tunneling electrons from the substrate ($\Delta\sigma = 1$, $\Delta m_s = -1$) dominate,

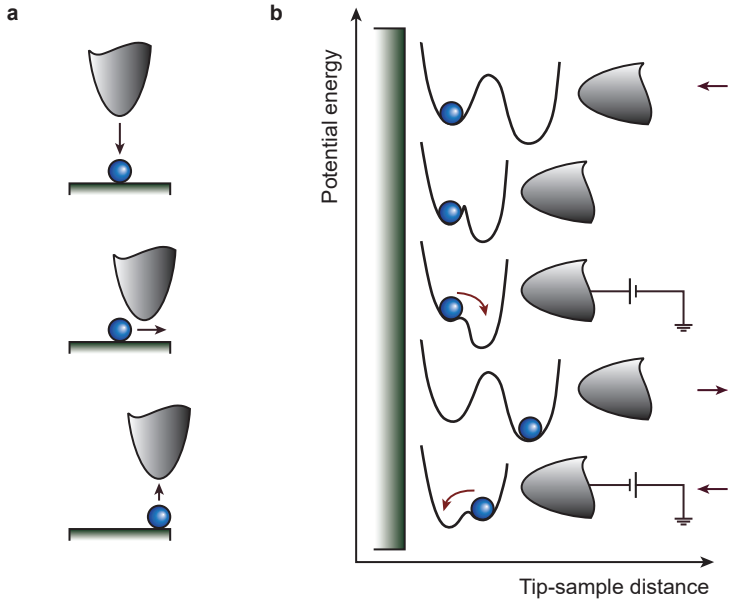

Figure 3.5: **Schematic illustration of lateral and vertical atom manipulation procedures. a** Lateral manipulation scheme, wherein the tip approaches the adatom until the tip-atom interaction is sufficiently strong to overcome the binding force to the surface (top). At this point, the tip is laterally displaced to the desired location, dragging or pulling the atom along (middle); the process is completed, and the tip is retracted to normal imaging heights (bottom). **b** Vertical manipulation scheme, with corresponding changes in the double-well potential illustrated. Top to bottom: the tip approaches the adatom of interest, bringing the two wells (left minima: represents adatom adsorption on the sample side; right minima: the same on the tip side) closer together. An applied electric field lowers the potential barrier between the two minima, allowing for the transfer of the atom to the tip. The tip is retracted and laterally moved to the desired drop-off location, where it is once again lowered toward the surface. Applying a bias voltage with opposite polarity flips the potential, allowing for the transfer of the atom to the surface. Adapted from [133].

thereby driving the local spin out of equilibrium toward a spin-state distribution with greater occupation in the excited states. At positive bias voltage, on the other hand, the spin-split density of states of the tip renders these $\Delta m_s = -1$ transitions much less efficient; in this case, the $\Delta\sigma = -1$, $\Delta m_s = +1$ transitions prevail, thereby driving the spin from the first excited state $|1\rangle$ into the ground state $|0\rangle$.

3.3. ATOM MANIPULATION

Atom-by-atom assembly allows for the construction of fully customizable atomic-scale architectures: in this framework, the tip-sample interactions induced by the STM tip are exerted on individual adsorbates in a systematic manner in order to precisely position them on the sample surface [134–136]. Since the first demonstrations of atom manipulation [100–102], significant progress has been made in the methodology and scale of this technique, with more recent developments demonstrating fully automatable and large-scale implementation of atomic assembly [18]. The ability to coordinate atoms at will

has enabled the study of artificial spin and electronic lattices [3], emergent phenomena in quantum magnetism [29, 32, 45, 50], and spin dynamics in extended chains [43, 44].

There are two basic schemes for implementing atom manipulation: lateral manipulation, wherein the adsorbate is pushed or pulled across the surface [137–140]; and vertical manipulation, which entails picking up and dropping the adsorbate via tip displacements along the surface normal.

Successful lateral manipulation (Fig. 3.5a) relies on the ability to tune the force of the tip-adsorbate interaction such that it overcomes the surface binding force. To achieve this, the tip is approached towards the atom until the attractive (repulsive) tip-adsorbate interaction is strong enough that a lateral displacement of the tip will pull (push) the atom across the surface. Once the adsorbate is coordinated into position, the tip is retracted back to standard imaging heights. This method [18] is used for the manipulation of single chlorine vacancies on the chlorinated Cu(100) surface in chapters 5 and 6.

On the other hand, vertical manipulation involves the transfer of the adsorbate from the surface to the tip, and vice-versa (Fig. 3.5). To achieve this, the tip is lowered in a controlled manner toward the surface until it makes—or nearly makes—mechanical contact with the adsorbate of interest. The initial tip–atom system can be represented by a double potential well: each minima corresponds to a stable configuration, where the adsorbate is either bound to the surface or the tip. As the tip approaches the adsorbate, the double potential well is increasingly distorted as the two minima are moved closer together.

If direct contact is established, the two wells actually merge to create a single potential well, thereby allowing the atom to be readily transferred to the tip side. In lieu of this, the two potential wells remain distinct, but the barrier between them can be lowered by applying an electric field (i.e., applying a bias voltage) [100], making it possible to transfer the atom to the tip in this scenario as well.

From here, the tip is retracted back to typical scanning heights and laterally displaced to the desired drop-off location. To deposit the atom, the tip is once again approached towards the surface, and a bias voltage (with opposite polarity) is applied. Reversing the bias voltage polarity causes the double potential well to flip, making it possible to ensure that binding to the surface now represents the lowest energy configuration for the atom. A vertical manipulation scheme [30] was used for positioning single Fe adatoms on the Cu_2N/Cu_3Au surface in chapter 4.

4

COMPLETE REVERSAL OF THE ATOMIC UNQUENCHED ORBITAL MOMENT

The orbital angular moment of magnetic atoms adsorbed on surfaces is often quenched as a result of an anisotropic crystal field. Due to spin-orbit coupling, what remains of the orbital moment typically delineates the orientation of the electron spin. These two effects limit the scope of information processing based on these atoms to essentially only one magnetic degree of freedom: the spin. In this work, we gain independent access to both the spin and orbital degrees of freedom of a single atom, inciting and probing excitations of each moment. By coordinating a single Fe atom atop the nitrogen site of the Cu_2N lattice, we realize a single-atom system with a large zero-field splitting—the largest reported for Fe atoms on surfaces—and an unquenched uniaxial orbital moment that closely approaches the free-atom value. We demonstrate a full reversal of the orbital moment through a single-electron tunneling event between the tip and Fe atom, a process that is mediated by a charged virtual state and leaves the spin unchanged. These results, which we corroborate using density functional theory and first-principles multiplet calculations, demonstrate independent control over the spin and orbital degrees of freedom in a single-atom system.

This chapter has been published in npj Quantum Materials **5**, 60 (2020)[141]. Theoretical results supporting this work were performed by J. W. González and F. Delgado.

4.1. INTRODUCTION

Efforts to downscale information storage to the single-atom limit have largely focused on readily probing, manipulating, and engineering the spin of magnetic atoms adsorbed on surfaces [31, 45, 62, 142]. This is primarily a consequence of orbital quenching: the orbital angular momentum **L** of these systems is often diminished due to the interaction between the spin-orbit coupling and the crystal field generated by the surface [55, 60], leaving the spin **S** as the only viable parameter for control. Even in the case of a partially preserved orbital moment, the spin-orbit interaction can act to create superpositions of the orbital angular momentum and spin states, meaning that only the total momentum **L** + **S** is preserved. In that case, independent excitations of **L** and **S** cannot occur.

Quenching of the orbital angular momentum directly affects the stability and lifetime of the atom's magnetization [46, 48]. The viability of information processing applications based on single atoms is, however, contingent on the spin stably maintaining its direction, and thus its magnetization, over time—which necessitates a large single-site magnetic anisotropy, as well as a slow relaxation of the magnetization. The energy barrier to flip the magnetic moment is determined by the magnetic anisotropy energy (MAE), which arises from the interplay between the crystal field and spin-orbit coupling. Specifically, the Coulomb potential generated by the crystal breaks the spherical symmetry of the free atom, thereby lending the orbital moment a certain orientation with respect to the crystallographic axes [55]. However, in the case of an almost fully quenched **L**, the spin-orbit coupling only acts to higher order to produce single-site magnetic anisotropy, which leads to MAE values far below the atomic spin-orbit coupling strength. Consequently, the crystal symmetry at the atomic site—and the overlap of the atomic orbitals with the surrounding ligands—plays a crucial role in preserving the orbital angular momentum of the atom and enhancing the MAE.

Engineering the local environment of the single atom to produce an axial crystal field can have significant consequences on preserving the free-atom orbital moment, and consequently, increasing the magnetic anisotropy [46, 48]. 3d transition elements are particularly appealing as the magnetic atoms of choice, as, in addition to their natural abundance, they can be easily deposited on surfaces and probed locally by scanning tunneling microscopy (STM) and spectroscopy. This is illustrated by STM experiments performed on Fe and Co atoms bound to the oxygen site of the MgO/Ag(100) surface, where the local symmetry ensures a nearly axial crystal field. The resultant orbital moment–which is nearly preserved in the out-of-plane direction for the Fe atoms, and fully preserved for the Co atoms— gives rise to large zero-field splittings of, respectively, 14 meV [46] and 58 meV [48]. However, in both of these cases, the energy multiplets evolve under the crystal field and spin-orbit coupling to become a mixture of S and L states, and accordingly, the transitions probed by inelastic tunneling spectroscopy (IETS) show that variations in **L** are associated with variations in **S**.

In this work, we present a single-atom spin system that combines a large MAE with an orbital angular moment that remains fully unquenched along the uniaxial direction. This situation is realized by placing Fe atoms atop the fourfold symmetric nitrogen binding site of the $Cu_2N/Cu_3Au(100)$ surface, thus engendering a zero-field splitting of 18 meV. We demonstrate that we are able to fully rotate the preserved orbital moment via a single-electron process between the tip and atom, without altering the spin state of

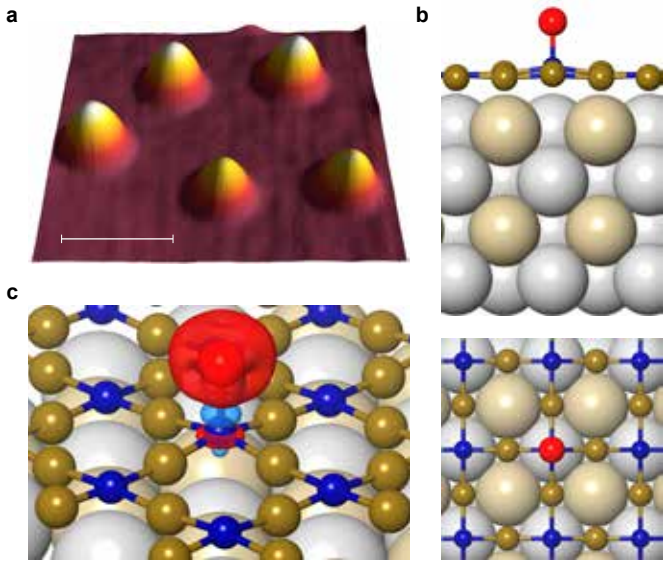

Figure 4.1: **Fe atoms atop the nitrogen site of the Cu_2N surface. a** STM constant-current topography (30 mV, 20 pA) of Fe atoms on a $Cu_2N/Cu_3Au(100)$ surface. To the bottom right, there are two Fe atoms bound to copper sites, and at the top, three Fe atoms atop nitrogen sites with larger apparent heights. Scale bar: 2 nm. **b** Side and top view of the binding geometry for the Fe atom (red) atop a N atom in the Cu_2N network (Cu brown, N blue) on a Cu_3Au crystal (Cu grey, Au yellow). **c** Calculated positive (red) and negative (blue) electron spin density.

the atom. Alternatively, we observe a distinct spin excitation, which does not affect the orbital moment. These finding are understood in terms of first-principles density functional theory (DFT) and electronic multiplet calculations.

4.2. ORIGIN OF THE UNQUENCHED ORBITAL MOMENT

The Cu_2N surface [74], in addition to providing protection to magnetic moments from electronic scattering, enables reliable and large-scale atom manipulation [30, 43, 61, 65, 71, 72]. Fe atoms on the Cu_2N lattice preferentially bind to the Cu-site, where the local C_{2v} symmetry produces a partially unquenched orbital moment resulting in in-plane uniaxial magnetic anisotropy energies of ~ 5 meV [61, 71]. A higher symmetry can be achieved, however, by coordinating the Fe atom atop the N-site instead, which, in principle, could preserve the orbital moment even more, and thus lead to larger anisotropy values. N-site adsorption on Cu_2N is also preferable over Cu-site adsorption, in that placing an Fe atom on an N-site requires one less atom manipulation procedure [50], vastly improving possibilities for building extended spin arrays. However, previous studies reported that no spin-flip excitations could be resolved for Fe atoms bound to N-sites [74].

We use a low-temperature STM to perform controlled single-atom manipulation and inelastic tunneling spectroscopy. We coordinate Fe atoms, deposited on an insulating

layer of Cu_2N that is grown on a $Cu_3Au(100)$ substrate [143], atop the N and Cu sites of the lattice (Fig. Fig. 4.1a). The apparent height of the Fe atoms atop the N-sites is ~ 3.1 Å, roughly 0.4 Å higher than those on Cu sites. The N binding site is fourfold symmetric (C_{4v}), with four Cu atoms as nearest neighbours, a lateral distance of 1.77 Å away (Fig. 4.1b). DFT calculations indicate that the N atom atop which the magnetic atom is bound is displaced upwards by 0.3 Åwith respect to the pristine surface configuration. The calculated magnetic moment for the spin of the Fe atom, considering an on-site Coulomb interactions $U = 5$ eV, is $\mu S \approx 4.36\mu$B, with μB the Bohr magneton; this indicates a local spin $S = 2$. The DFT-calculated valence electron spin density (Fig. 4.1c) shows that the axial symmetry is largely intact. Thus, we can expect the orbital moment to be preserved in the out-of-plane direction, while it is quenched in-plane. The typical overestimation of the orbital momentum quenching by DFT calculations precludes a quantitative description of **L**, and thus, of the resulting MAE [144, 145].

Instead, here we adopt an alternative strategy: we carry out an electronic multiplet calculation based on a point-charge model (PCM) description of the crystal field, where electron-electron repulsion between Fe d-electrons, spin-orbit coupling, and Zeeman contributions are considered explicitly [66, 146]. The atomic positions and charges are extracted from the DFT calculations. A similar method was applied successfully to study the spin excitations of Fe on MgO [46].

4.3. DESCRIBING THE ELECTRONIC MULTIPLET

The lowest energy levels derived from the multiplet calculations are shown in Fig. 4.2a. The crystal field (CF) contribution is separated into its axial and transverse components: the former splits off a tenfold ground state degeneracy, while the latter splits this into two spin quintuplets. The spin-orbit coupling——where we used $\lambda = -9.60$ meV for the PCM, and -9.41 meV for the spin-orbit model——partially lifts the degeneracy within the two quintuplets. Finally, the magnetic field B_z along the out-of-plane direction breaks all remaining degeneracies. At a non-zero field in the out-of-plane direction, the lowest two states have orbital moments $L_z = \pm 1.98$, closely approaching the free-atom value. Below, we will approximate these two states as $L_z = \pm 2$. Notably, the multiplets evolve under the crystal field and spin-orbit coupling to become nearly pure product states of the S_z, L_z eigenstates. This separation of the spin and orbital degrees of freedom is permitted by the relative dominance of the magnetic anisotropy energy over the strength of the spin-orbit coupling. In fact, use of the total angular momentum basis is not adequate here, since the magnetic anisotropy terms do not commute with the total angular momentum ($\hat{\mathbf{J}}^2$ and $\hat{\mathbf{J}}_z$).

When interpreting spin excitation spectroscopy on individual magnetic atoms, it is convenient to employ an effective spin Hamiltonian [61, 72, 147]. However, in this situation the unquenched orbital moment makes the effective spin framework incomplete [53]. Instead, we use the following anisotropic spin-orbit Hamiltonian [53]

$$\hat{\mathcal{H}} = B_2^0 \hat{O}_2^0 + B_4^0 \hat{O}_4^0 + \lambda_{\mathrm{SO}} (\hat{\mathbf{L}} + 2\hat{\mathbf{S}}) \cdot \mathbf{B}, \tag{4.1}$$

where $\hat{O}_k^q$ are the Stevens operators, which in this case are applied to the eigenstates of the orbital moment, and B_p^q are their associated coefficients, respectively. The last term

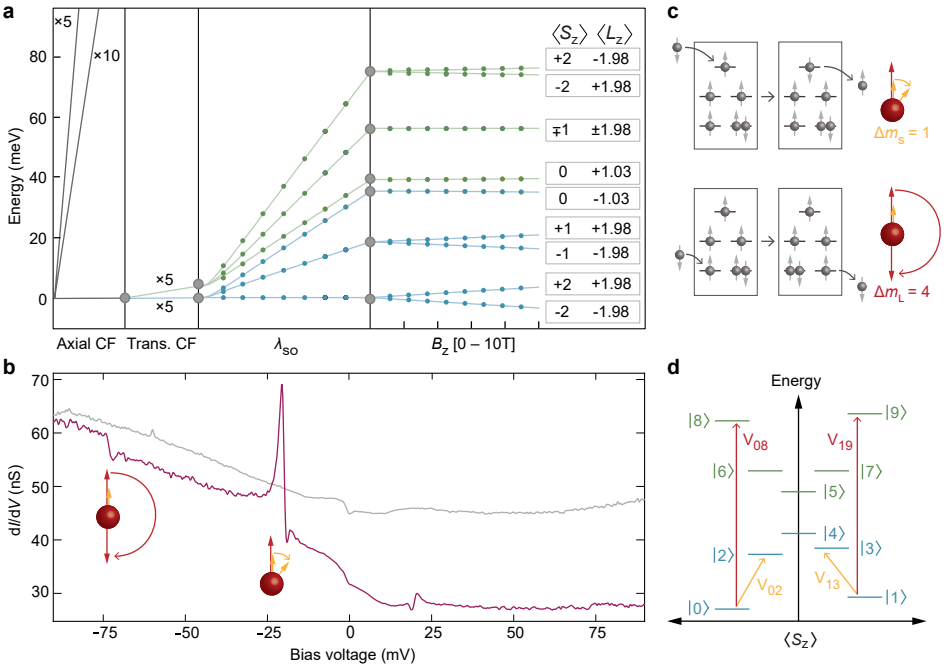

Figure 4.2: **Energy spectra and IETS measurements.** **a** Energy spectra derived using both the PCM (solid lines) and the spin-orbit model (dots). The expectation values of S_z and L_z are indicated for each state. The transverse crystal field generates two distinct spin quintuplets (blue and green). The energy scale is defined relative to the ground state energy, except in the rightmost panel where the Zeeman splitting is considered, in which case the absolute energies are plotted. **b** Differential conductance ($\mathrm{d}I/\mathrm{d}V$) spectroscopy performed with a functionalized tip on a single Fe atom (magenta) and on bare Cu_2N (gray) ($T = 0.3$ K, $B_z = 4$ T, 400μV modulation, taken at -90 mV, 8 nA). **c** Co-tunneling mechanism for inelastic excitations of the spin (top) and orbital (bottom) momenta. Each rectangle represents the energy levels of the five ℓ_z orbitals as follows: $\ell_z = \pm 2$ (bottom), $\ell_z = \pm 1$ (middle), $\ell_z = 0$ (top). In the case of a spin-excitation, the electrons are free to tunnel on and off the same singly-occupied orbital. **d** Schematic representation of the two lowest quintuplets, with the spin and orbital transitions probed by IETS marked with arrows.

represents the Zeeman energy due to an external field **B**. As we consider both the spin **S** and orbital moment **L**, there is no need to invoke the Landé g-factor. The results of this model, implemented with optimal fitting parameters, are also depicted in Fig. 4.2a. Note that there is perfect agreement between the PCM and the spin-orbit model presented in Eq. 4.1. We additionally confirm these results using electronic multiplet calculations derived using the Wannier Hamiltonian to approximate the crystal and ligand fields produced by the surface atoms. This approach provides a more accurate quantitative description, and additionally accounts for charge transfer and surface polarization.

4.4. INDEPENDENT SPIN AND ORBITAL EXCITATIONS

We perform an IETS measurement with an out-of-plane field of 4 T, revealing a splitting of the zero-field spin excitation, with threshold voltages at 17.9 ± 0.7 meV and $19.4 \pm$

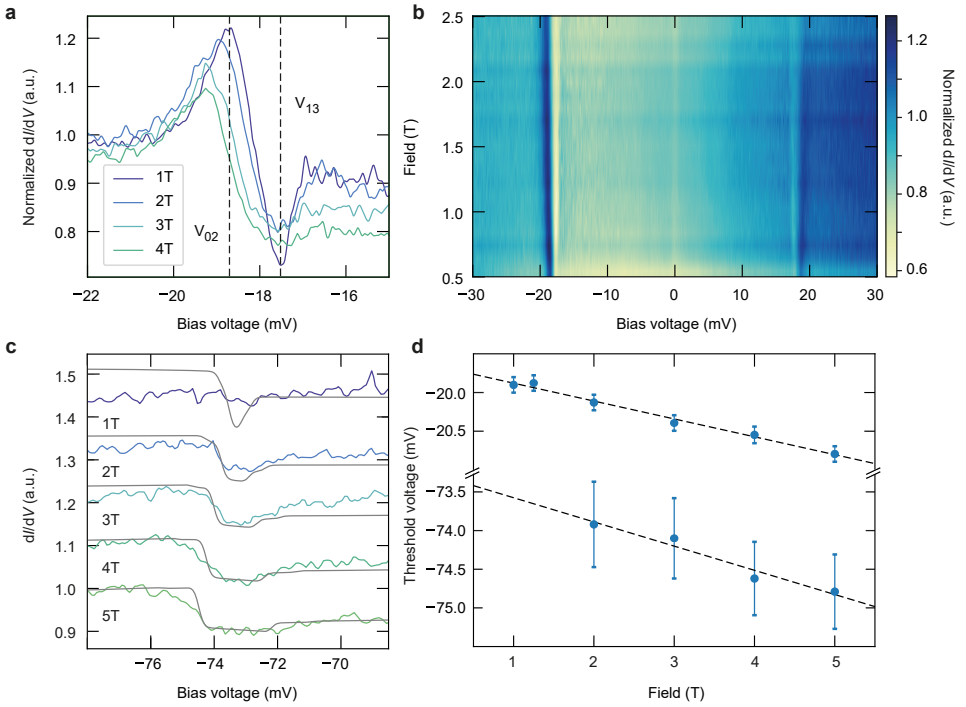

Figure 4.3: **Magnetic field dependence of the spin and orbital excitations.** **a** Differential conductance spectroscopy for different values of the external magnetic field, with the dotted lines denoting threshold voltages V_{02} and V_{13} at 1 T. b Color map of dI/dV spectroscopy as a function of magnetic field. **c** Differential conductance spectroscopy (conductance set-point of -90 mV, 8 nA) showing a transition at ~74 meV, for various magnetic fields, normalized and shifted vertically (with respect to the 5 T spectrum) for clarity. Overlaid are the corresponding transport calculations (grey) derived from the point charge model, horizontally shifted by −1.4 meV to match the experimentally derived threshold voltage. **d** The measured threshold voltages V_{02} and V_{08} as a function of the external magnetic field. The error bars here only account for the uncertainty in the fit of the step position. Dashed lines are linear fits, indicating a shift of 0.23 ± 0.04 meV/T for the V_{02} transition and 0.31 ± 0.05 meV/T for the V_{08} transition

0.7 meV, as shown in Fig. 4.2b. These transitions can only be probed with a tip that is functionalized by picking up individual Fe atoms from the surface. The results of Fig. 4.2a allow us to uniquely assign the observed transitions to excitations between specific states. When describing these states, we choose to use product state notation since S_z and L_z are approximately good quantum numbers here. The lower energy excitations are spin-only transitions ($\Delta S_z = \pm 1$, $\Delta L_z = 0$) corresponding to an excitation from the ground state $|S_z\rangle|L_z\rangle = |-2\rangle|-2\rangle \equiv |0\rangle$ to $|-1\rangle|-2\rangle \equiv |2\rangle$, corresponding to an excitation threshold voltage V_{02}, as well as from the $|+2\rangle|+2\rangle \equiv |1\rangle$ state to $|+1\rangle|+2\rangle \equiv |3\rangle$, with threshold V_{13} (Fig. 4.2d). At zero field, $|V_{02}| = |V_{13}| = 18.4 \pm 0.6$ meV.

In addition, we observe a higher energy excitation at 73.9 ± 0.8 meV (see Fig. 4.2b), which we denote by the threshold voltage V_{08}. This feature corresponds to an excitation from the ground state $|0\rangle$ to the excited state $|-2\rangle|+2\rangle \equiv |8\rangle$; i.e., going from the lower

spin quintuplet to the upper spin quintuplet (see Fig. 4.2d). An analysis of the calculated transition strengths confirms that an excitation from $|0\rangle \rightarrow |8\rangle$ occurs with a much larger amplitude than from other possible paths, such as transitions from $|0\rangle \rightarrow |6\rangle$ or $|2\rangle \rightarrow |8\rangle$. Additionally, the energy at which this transition occurs quantitatively agrees with the energy difference between the states $|0\rangle$ and $|8\rangle$ across the various models we implement, namely the point-charge and Wannier models.

Unlike a conventional spin excitation—in which the tunneling electron spin only interacts with the atom's spin ($\Delta S_s \leq 1$), leaving the orbital moment unchanged—we observe an independent excitation of only the orbital moment, with $\Delta L_z = 4$. Although orbital excitations have been previously reported [148, 149], here we observe a full, independent rotation of an unquenched orbital moment. These transitions are not accounted for by the usual spin exchange terms $J\mathbf{S}\cdot\sigma$ [59, 150], even when the orbital and spin degrees of freedom are accounted for, as in Eq. 4.1.

Rather, this orbital transition can be understood via a co-tunneling path that takes into account both the spin and the orbital momentum of the initial, intermediate and final states, as depicted in Fig. 4.2c [151, 152]. Since the transition is expected to occur with similar amplitude for the hole and electron charged states, we will focus on the latter for the following discussion. In this case, the dominant channel is mediated through the negatively charged intermediate state $|S_z = -3/2\rangle|L_z = 0\rangle$. Accordingly, the co-tunneling transition amplitude between the ground state $|0\rangle$ and the excited state $|8\rangle$ can be understood by introducing the creation and annihilation operators, $\hat{d}^\dagger_{\sigma_z,\ell_z}$ and $\hat{d}_{\sigma_z,\ell_z}$, for an electron with spin σ_z in an orbital with angular momentum ℓ_z (centered on the atom). The dominant transition amplitude between states $|0\rangle$ and $|8\rangle$ is thus proportional to [151, 152]

$$\left\langle +2\middle|\left\langle -2\middle|\hat{d}_{+\frac{1}{2},-2}\middle|-3/2\right\rangle\middle|0\right\rangle\left\langle 0\middle|\left\langle -3/2\middle|\hat{d}^\dagger_{+\frac{1}{2},+2}\middle|-2\right\rangle\middle|-2\right\rangle. \tag{4.2}$$

This co-tunneling path corresponds to a spin-up electron tunneling onto the $\ell_z = +2$ orbital, thus creating a charged virtual state with a net spin $S_z = -3/2$ and orbital moment $L_z = 0$. An electron then tunnels off the $\ell_z = -2$ orbital, restoring the net spin to $S_z = -2$ and changing the orbital moment to $L_z = +2$, thereby completing the $\Delta S_z = 0$, $\Delta L_z = 4$ transition. Thus, we show independent transitions of the spin and unquenched orbital angular momenta, where we can rotate one of these atomic degrees of freedom without affecting the other.

At first sight, a $\Delta L_z = 4$ transition may seem to violate conservation of total angular momentum. However, we point out that the orbital moment of a freely propagating electron is defined relative to an arbitrary origin, and can therefore, unlike the spin, assume an arbitrary value. An electron tunneling from the tip is thus free to carry an orbital moment, and inelastically excite the atomic orbital moment. Within this framework, conservation of total momentum can be understood in terms of the Einstein-de Haas effect, wherein the angular momentum of the tunnelling electron is translated into an infinitesimal rotation of the macroscopic lattice [153, 154].

We trace the evolution of the magnetic behavior of the single atom as a function of external field: in Fig. 4.3a, b, and c we show IETS measurements of the spin and orbital excitations, performed for a range of discrete fields up to 5 T. In both cases, we observe the

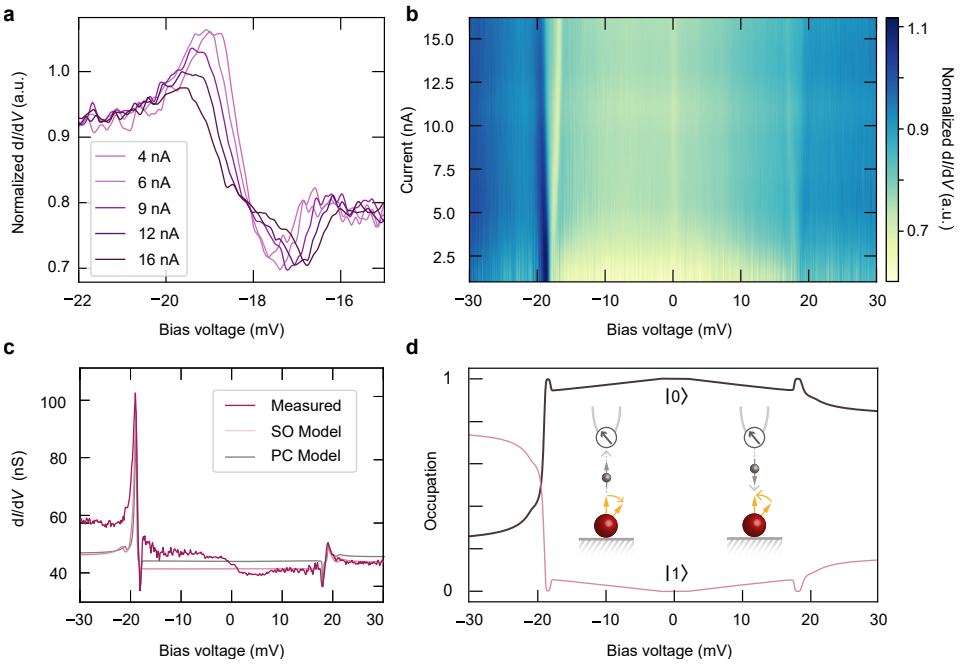

Figure 4.4: **Conductance dependence of non-equilibrium electron transport**. **a** Differential conductance spectroscopy for different conductance values. **b** Color map of conductance-dependent $\mathrm{d}I/\mathrm{d}V$ spectroscopy. The same experimental parameters ($B_z = 4$ T, $T = 0.3$ K, 150 μV modulation) apply for both **a** and **b**. **c** Spectroscopy measurement at $B_z = 2$ T (magenta), taken at a conductance set-point of -90 mV, 8 nA, compared to normalized transport calculations derived from the point-charge (grey) and spin-orbit (pink) models. **d** Calculated voltage-dependent occupation of the two lowest energy states using the point-charge model ($P_T = -0.3$).

Zeeman effect as a shift towards higher threshold voltages at higher field. The measurements indicate a shift in the threshold voltage of 0.23 ± 0.04 meV/T and 0.31 ± 0.05 meV/T for the spin and orbital transitions, respectively (Fig. 4.3d). When expressed in terms of an effective $S = 2$ spin model in the absence of orbital angular momentum, [61] the shift for the spin excitation would correspond to a Landé factor of ~3, on par with previously reported large values [46, 48, 155].

Additionally, we expect the orbital excitation to correspond to two transitions: $|0\rangle \rightarrow |8\rangle$ and $|1\rangle \rightarrow |9\rangle$, which should split as a function of magnetic field due to the Zeeman effect. We observe that the step is broadened as the field is increased, which is compatible with a splitting of V_{08} and V_{19}. We note that V_{19} is marked by a step down in the differential conductance, which is due to spin-polarized elastic conductance, combined with a reconfiguration of the occupation of states $|0\rangle$ and $|1\rangle$ around the threshold voltages.

The observed behavior is well reproduced by the transport calculations derived from the point-charge model. In fact, the high degree of agreement between the experimentally and theoretically derived results here is remarkable, as the point-charge calculations are based solely on DFT results, and thereby don't have any additional fitting parameters, except for a screening factor applied to the free-atom spin-orbit coupling (ad-

justed only to reproduce the energy of the spin excitation). However, the threshold voltage corresponding to the orbital excitation is off by ~1.4 meV when comparing the transport calculations to the experimental data. In order to properly compare the evolution of the step, we correct for this shift in Fig. 4.3c. We note that the measurements shown in panels a and b are obtained on different atoms, using a different functionalized tip, than measurements shown in c and d—this causes a slight offset in the measured threshold voltages, presumably due to the tip field or variations in the local environment. We try to account for these variations, and the ambiguity in defining the threshold energy due to the unusual lineshape of the spin excitations, in the error associated with V_{02}, V_{13}, and V_{08}.

The field dependence of the threshold voltages confirm our assignation of the observed transitions to those belonging to independent excitations of the spin and orbital momentum. The ratio between the rate of change of the V_{08} and V_{02} transitions, amongst the various models we implement, is consistently between 1.6 to 2; experimentally, we observe a ratio of 1.3 ± 0.3. In contrast, the V_{06} and V_{17} transitions, which corresponds to full rotations of the orbital moment along with a partial rotation of the spin, are expected to shift much faster under the effect of external field, with a rate of change 3 times that of V_{02}.

In the absence of non-equilibrium effects, inelastic spin excitations ($\Delta S_z = \pm 1$) are characterized by approximately square steps in the differential conductance [110], which originate from co-tunneling events [59, 150]. However, additional nonlinearities may appear at the threshold voltage due to changes in the instantaneous spin state of the atom, which modify the magnetoresistance of the junction, and thus, the $\mathrm{d}I/\mathrm{d}V$ lineshapes [65, 124]. The dynamical effects that we observe at the inelastic tunneling threshold voltage for the spin excitation (Fig. 4.4a) are indicative of relaxation times from state $|1\rangle$ longer than the average time between two tunneling electrons (~200 ps at 1 nA).

As the presence of non-equilibrium features is attributed to dynamic processes linked to the inelastic electron transport, they are expected to be conductance-dependent. We investigate this dependence by performing $\mathrm{d}I/\mathrm{d}V$ measurements as a function of current set-point, as shown in Fig. 4.4a and b. For this range of conductance values, we observe a decrease in the strength of the non-linearity with increasing tunnel current [124, 156] and a shift in the inelastic steps, both of which are due to the local field from the exchange interaction between the Fe atom and the tip [157].

Further insight can be obtained by simulating the non-equilibrium dynamics of the local spin (Fig. 4.4c). This is done on two fronts: on one hand, starting from the point-charge model calculation, we calculate the transition rates and the non-equilibrium occupations in the weak coupling limit using a co-tunneling description of transport [151, 152]. On the other, we use the spin-orbit model Eq. 4.1 exchange coupled to the itinerant electrons. In both cases, the evolution of the occupation is accounted for by a Pauli master equation [59, 150]. Tracing the occupation of the two lowest spin states as a function of voltage (Fig. 4.4d) delineates that below the inelastic threshold voltage, the ground state occupation exceeds 90%. Once the applied voltage reaches the excitation threshold, spin-flip excitations cause a significant drop in the occupation of $|0\rangle$.

4.5. DISCUSSION

By coordinating a magnetic atom atop the fourfold symmetric nitrogen binding of the Cu_2N lattice, we have realized a single atom system with a large magnetic anisotropy, which follows from a preserved orbital angular momentum, an ingredient that is essential to the application of magnetic atoms in magnetic storage and information processing. In this system, under the effects of the crystal field and spin-orbit coupling, the multiplets emerge as nearly pure **L** and **S** product states, which allows us to treat these parameters as two independent degrees of freedom. We demonstrate independent control over both the spin and orbital moment, showing a full inversion of the orbital moment by means of a single electron, without affecting the spin.

As control over the orbital angular momentum shows many parallels to that of the spin momentum, we believe that this development adds a new dimension to studies on single-atom magnetism. Moreover, as Fe atoms bound to N-sites are easily manipulable, these results form a promising basis for future research on extended lattices, that can interact through both the spin and orbital angular momentum.

4.6. METHODS

4.6.1. MULTIPLET CALCULATIONS FOR FE/Cu_2N/Cu_3Au(100) SYSTEM

For the multiplet calculations of Fe atoms, we used an archetypal value of the Hubbard repulsion $U = 5.208$ eV ($U - J = 5$ eV) [69, 158]. We have taken the atomic values of $\langle r^2 \rangle = 1.393$ and $\langle r^4 \rangle = 4.496$ atomic units [53]. Instead of correcting the $\langle r^2 \rangle$ and $\langle r^4 \rangle$ parameters due to covalency and other known limitations of the point charges, we have taken the spin-orbit coupling λ as a fitting parameter to reproduce the 18 meV step. The optimal fitting is found when the spin-orbit coupling is screened by a factor 0.738, which translates into a (many-body) effective spin orbit coupling of -9.60 meV. The transport calculations under the co-tunneling regime were carried out assuming electron-hole symmetry, i.e., $E_{0-} - E_0 - E_F = E_F - E_0 + E_{0+}$. For the surface hybridization constants, we take $V_{k_F,S} = 0.562$ eV, and for the tip-hybridization $V_{k_F,T,d_{z^2}} = 0.183$ eV= $6V_{k_F,T,d_{x^2-y^2}} = 6V_{k_F,T,d_{xy}}$.

4.6.2. PARAMETERS OF THE ANISOTROPIC SPIN-ORBIT HAMILTONIAN

The parameters B_p^q and λ_{SO} of the spin-orbit Hamiltonian (Eq. 4.1) were obtained by fitting the corresponding energy spectrum to the results of the multiorbital electronic multiplet Hamiltonian at zero magnetic field. The best fit was obtained for $B_2^0 = -1.404$ eV, $B_4^0 = 0.188$ eV, and $B_4^4 = 0.16$ meV, which indicates an almost pure uniaxial easy axis system. The value obtained for the spin-orbit coupling is $\lambda_{SO} = 9.41$ meV. In addition, the coupling to the surface was taken to be $(\rho J_{K,S}) = 0.25$, where ρ is the density of states at the Fermi energy and $J_{K,S}$ is the Kondo exchange coupling with the surface, while $(\rho J_{K,T}) = 0.0484$ for the tip. In addition, a direct tunnelling term of $(\rho T) = 0.25$ was also assumed (we have assumed the same density of states for the surface and the tip).

5

CONFINED VACUUM RESONANCES AS ARTIFICIAL ATOMS WITH TUNABLE LIFETIME

Atomically engineered artificial lattices are a useful tool for simulating complex quantum phenomena, but have so far been limited to the study of Hamiltonians where electron-electron interactions do not play a role—but it's precisely the regime in which these interactions do matter where computational times lend simulations a critical advantage over numerical methods. Here, we propose a new platform for constructing artificial matter that relies on the confinement of field-emission resonances, a class of vacuum-localized discretized electronic states. We use atom manipulation of surface vacancies in a chlorine-terminated Cu(100) surface to reveal square patches of the underlying metal, thereby creating atomically-precise potential wells that host particle-in-a-box modes. By adjusting the shape and size of the confining potential, we can access states with different quantum numbers, making these patches attractive candidates as quantum dots or artificial atoms. We demonstrate that the lifetime of electrons in these engineered states can be extended and tuned through modification of the confining potential, either via atomic assembly or by changing the tip-sample distance. We also demonstrate control over a finite range of state-filling, a parameter which plays a key role in the evolution of quantum many-body states. We model the transport through the localized state to disentangle and quantify the lifetime-limiting processes, illustrating the critical dependency of the electron lifetime on the properties of the underlying bulk band structure. The interplay with the bulk bands also gives rise to negative differential resistance, opening possible avenues for engineering custom atomic-scale resonant tunnelling diodes, which exhibit similar current-voltage characteristics.

This chapter has been published in ACS Nano **16**, 11251–11258 (2022) by R. Rejali, L. Farinacci, D. Coffey, R. Broekhoven, J. Gobeil, Y. M. Blanter, and A. F. Otte [159].

Artificial lattices serve as quantum simulators for realizing and studying fundamental properties of real materials, with the advantage that the relevant interactions can be precisely controlled. While different experimental approaches, such as using ultra-cold atoms [9], optical lattices [6, 14], or trapped ions [12], have been successfully implemented in the study of artificially constructed systems, atom manipulation casts the scanning tunneling microscope (STM) as a particularly appealing platform: the scanning probe framework uniquely allows for creating and characterizing the electronic properties of 2D artificial matter on the atomic scale [3]. Typically, atomic impurities are patterned to construct a potential landscape that mimics a specific physical system, with the aim of studying model Hamiltonians. This approach has led to the realization of a wide range of novel states in, for instance, Dirac materials, like the Lieb lattice [19, 20] and artificial graphene [21, 22], as well as higher order topological insulators [23, 24], among others [25–28, 160]. These studies offer rare insight into the parameters that govern the electronic behaviour of these systems, but are restricted by the short electron lifetime of the constituent artificial atoms to the limiting case in which electron-electron interactions do not play a role. Additionally, short electron lifetimes limit the available energy resolution; the most popular STM approach so far, which relies on confining surface states, lacks flexibility in tuning this parameter [161–163].

Here, we explore a new platform for realizing artificial lattices, based on confining field-emission resonances (FERs): a class of quantized electronic states localized in the vacuum, between the surface and the probe tip, that arise in the high bias regime, i.e. exceeding the sample work function. We show that confining potentials can be engineered to enable the study of states with different orbital character [22, 164, 165], with precise control over the energy and quantum numbers of the states. We study the electron lifetime of these states, and demonstrate that we can finely tune it—and consequently, to some extent, the average occupation—by adjusting the tip-height or patch dimensions. The ability to tune the lifetime and occupation of artificial atoms is a critical first step towards simulating many-body quantum states driven by electron-electron interactions. We also observe specific voltage-current characteristics, namely negative differential resistance, which are analogous to those of resonant tunneling diodes [166], making the confined FERs also suitable to possible applications in creating customizable, atomic scale diodes.

5.1. ENGINEERING LATERAL CONFINEMENT OF VACUUM STATES

We use atom manipulation of single vacancies in the chlorine-terminated Cu(100) surface to engineer lateral confinement of field emission resonances. By coordinating chlorine vacancies— which are easily manipulable and thus suited to large scale atomic assembly [18, 19, 25–27]—adjacent to each other, we construct patches of exposed copper, surrounded by areas of homogeneous, monolayer chlorine coverage (figure 5.1a). The bare and chlorinated Cu(100) surfaces host FERs at bias voltages exceeding the local work function, at 4.6 V [167] and 5.7 V [168], respectively. These resonances can be readily modelled with a one-dimensional potential in the out-of-plane direction (figure 5.1, see supplementary for details). The work function difference between the two surfaces results in a shift in the measured resonance energies (figure 5.1c), in accordance with previous studies [169–172].

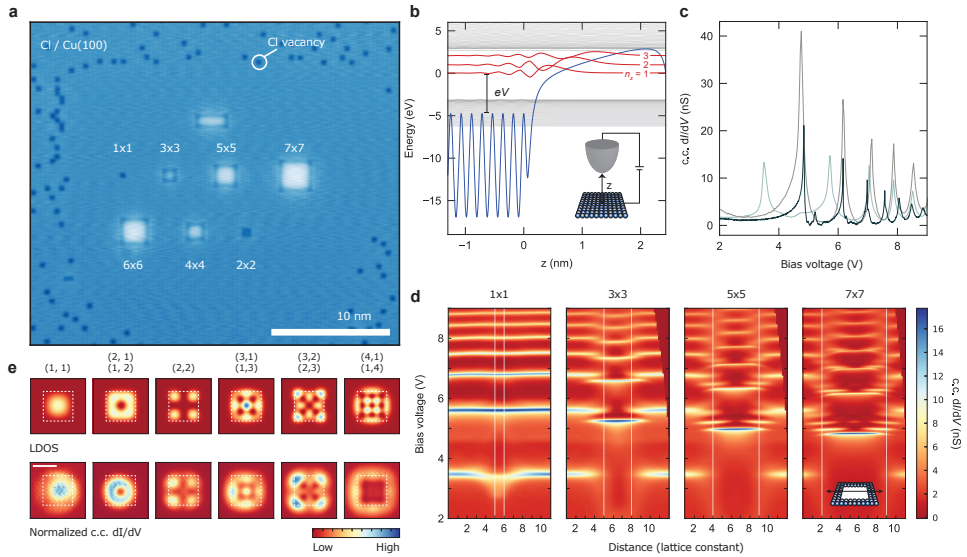

Figure 5.1: **Confinement of field-emission resonances. a** STM constant-current topography (600 mV, 300 pA) of square, atomically assembled patches of Cl vacancies, with sizes indicated in unit cells. **b** Potential landscape (blue) between sample (left) and tip (right) for a finite bias voltage V. Amongst the wave functions (grey) calculated for this potential, are the first three field-emission resonances (red). Inset: schematic of the tip-sample junction. **c** Constant-current differential conductance spectra acquired for bare Cu(100) (grey, 250 pA current setpoint), the chlorine monolayer (turquoise, 100 pA), and the center of the 7 × 7 patch (dark green, 100 pA). The first peak on the chlorine monolayer (3.5 V), being below the surface work function, corresponds to an image-potential state. **d** Stacked constant-current (100 pA) differential conductance spectra taken along a line crossing the center of each patch (shown in inset), with the corresponding patch size indicated (top). A correction is applied to the data to rectify the asymmetry of the tip electric field (see supplementary). White lines indicate the patch boundaries. **e** Calculated LDOS of the particle-in-a-box states ($|\Psi|^2$), obtained using a finite well model (top row). Normalized constant-current (100 pA) differential conductance maps acquired for the 7 × 7 patch at the resonance energies of the first principal FER ($n_z = 1$, $(n_x, n_y) = (1,1)$) and the following sub-resonances. White squares delineate the spatial extent of the simulated potential well (top row) and the physical patch (bottom row).

Spectroscopy acquired at the center of the 7 × 7 patch (dimensions defined in unit cells of the chlorine lattice) exhibits additional resonances, in comparison to the bare and chlorinated Cu(100) surfaces (figure 5.1c). As shown in figure 5.1d, these additional resonances belong to a series of sub-resonances following each primary FER, and can in fact be resolved for each primary FER, up to and including the the fourth primary resonance. We use the principal quantum number n_z for the primary FERs. Note that the additional modes are only observed above the energy of the first resonance ($n_z = 1$) on bare Cu(100) (figure 5.1c). The full in-plane structure of the confined modes for the larger patches is best visualised by constant-current differential conductance maps taken at voltages corresponding to the sub-resonances of the first FER on the 7×7 patch, as shown in figure 5.1e. The observed states can be recognised as two-dimensional particle-in-a-box modes, with quantum numbers n_x and n_y, and can be accurately reproduced by the eigenstates of a finite potential well (see supplementary for details). Similar to previous

works [165], the nodal patterns of the first three modes are analogous to the orbitals of an two-dimensional atom, with the first state corresponding to the *s*-like state, and the second to the *p*-like, and subsequently the *d*-like state. Finally, we note that the energy of the FERs depends on the patch size: as the patch size is increased, the FER energy shifts down, tending toward the limit of bare Cu(100). All in all, the assembled patches can be seen as atomically precise potential wells, wherein the energy, spacing, and order of the states can be tuned by adjusting the shape and size of the confining potential. We note that the single vacancy [19, 25–27] stands out as an exception, as the necessary change in the local work function cannot take place on such small length-scales: as such, the vacancy acts as a scattering center, rather than a confinement potential.

5.2. RESONANT TRANSPORT THROUGH A BOUND STATE

In order to characterize the electron lifetime, we consider the transport through these confined states: two electron baths, one on the tip side and another on the sample side, act as decoherent sources, the contributions of which we can disentangle by investigating the evolution of the differential conductance spectra as a function of conductance setpoint, as shown in figure 5.2a. With increasing conductance setpoint, we observe a slight shift in the energy of the FERs, which is explained by the increased out-of-plane confinement (figure 5.1b), as well as the appearance of negative differential resistance (NDR). The appearance of NDR at high conductance setpoints gives us qualitative insight into the coupling of the resonances with the substrate and tip.

We consider a transport model describing the resonant tunneling of independent electrons from (to) the tip and sample through a level localized between the two potential barriers (2a, inset, see chapter 7). In this framework, the current through a single resonance is given by:

$$I_i = \frac{2G_Q\hbar}{e}\frac{\Gamma_t^i(z,V)\Gamma_s^i(z,V)}{\Gamma_t^i(z,V)+\Gamma_s^i(z,V)}\left(\frac{\pi}{2}+\tan^{-1}\left(\frac{2(eV-E_i(z,V))}{\hbar(\Gamma_t^i(z,V)+\Gamma_s^i(z,V))}\right)\right), \tag{5.1}$$

where the quantum of conductance is $G_Q = e^2/(\pi\hbar)$, Γ_t^i and Γ_s^i are, respectively, the tip and sample decay rates for the ith resonance, and E_i its energy, whose shift with bias voltage we will initially neglect for simplicity. In general, the tip and sample decay rates are both distance and voltage dependent. For the former, this dependence is derived by considering the transmission through the tunnel barrier. The sample decay rate, however, encapsulates an effective barrier that depends on the surface band-structure, and the relationship between Γ_s and V is non-trivial; we approximate this dependence as either constant or linear, depending on the width of the voltage window we consider. The differential conductance, in turn, can be obtained by differentiating the current with respect to voltage, and contains terms that scale with the derivatives of the decay rates and the energy of the resonance (see chapter 7 for the full expression).

5.3. ESTIMATING AND TUNING THE ELECTRON LIFETIME

We can gain quantitative insight into the tip and sample decay rates by focusing strictly on the first principal FER (figure 5.2b inset): this allows us to drastically reduce the num-

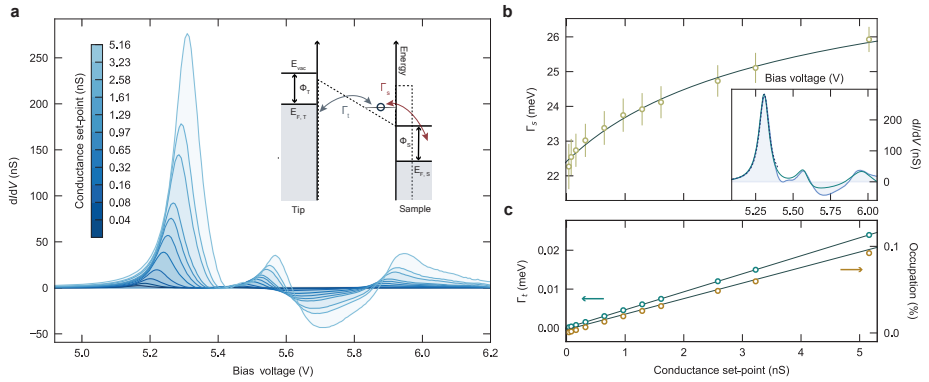

Figure 5.2: **Extracting tip and sample decay rates.** **a** Constant-height differential conductance spectra obtained at the center of the 5 × 5 patch for a range of conductance setpoints ((250 pA → 32 nA), 6.2 V). Inset: schematic of the double-barrier potential (dotted line) implemented in the rate equations, with the decay rates to the tip and sample, Γ_t and Γ_s, indicated. **b** Inset: constant-height differential conductance (light blue, shaded) acquired at the center of the 5 × 5 patch (32 nA, 6.2 V). Calculated $\mathrm{d}I/\mathrm{d}V$ using a resonant tunneling model for a single level (navy, dotted line) or several, independent levels (green solid line). **b, c** Sample (**b**, yellow circles) and tip (**c**, green circles) decay rates extracted for the first principal resonance as a function of conductance setpoint, fitted (solid grey line) to an inverse natural logarithm and a line, respectively. The tip decay rate is evaluated at the energy of the peak of the first principal field emission resonance. **c** Average occupation versus conductance setpoint (orange circles), and the corresponding linear fit (solid grey line).

ber of free variables to a single resonance ($i = 0$), and consequently to meaningfully account for the effects of the changing level E_0; additionally, we simplify $\Gamma_s(V)$ to a constant in the narrow voltage range around the resonance. By fitting the measured differential conductance at each conductance setpoint to our model, we can extract a value for the tip and sample decay rates as function of conductance setpoint (figure 5.2b and c).

In figure 5.2b, we see that Γ_s increases with conductance setpoint, which can be related to the FER wave function: in general, decay to the bulk is governed by the overlap of the vacuum-localized state to the substrate, which is in turn determined via the penetration of the state into the bulk, the evanescent tail of the bulk states into the vacuum, and the diminished electronic screening in the area between the surface and the vacuum [173, 174]. Bringing the tip closer causes a redistribution of the weight of the wave function toward the surface, rendering the scattering channels to the bulk more efficient [175], leading to an increase in Γ_s. More precisely, we consider that the sample decay rate should scale linearly with the wave function overlap of the FER with the sample [173], and for simplicity we assume its increase to be inversely proportional to the tip-sample distance. Given the exponential dependence of current with distance, we thus expect an inverse logarithmic dependence of the sample decay rate on the conductance setpoint. The fit in figure 5.2b shows this simple relation describes the change in Γ_s appropriately.

The evolution of the tip decay rate with conductance setpoint is straightforward: this rate should scale exponentially with the tip-sample distance, meaning it should be linear with the conductance setpoint and intercept with the origin, as we see in figure 5.2c.

Importantly, the changes in the decay rates impact the overall occupation of the state. The occupation is determined by the ratio of the tip decay rate to total decay rate $\Gamma_s + \Gamma_t$, meaning that the occupation of the state can be tuned via the tip-height, as shown in figure 5.2c: the occupation linearly increases with the conductance setpoint. In effect, this means that the competing factors determining the time-average occupation—the rate of tunneling electrons versus the increase in the lifetime-limiting rate, Γ_s—results in the state filling increasing as the tip is brought closer.

We now extend our scope to account for transport through the higher energy states—around 5.6 V ($(n_x, n_y) = (2,1),(1,2)$) and 6 V ($(3,1),(1,3)$), respectively. To do so, we assume the resonances are independent, i.e. that the total current is determined by the sum of the currents I_i through each resonance; additionally, we explicitly account for the voltage-dependence of $\Gamma_s(V)$ as linear to first approximation. As seen in figure 5.2b (inset), our model successfully reproduces the key features of the measured differential conductance over the entire voltage range, with, in particular, the presence of NDR between ~ 5.6 to 6 V. In this window, we find $d\Gamma_s/dV < 0$. In fact, we find it is necessary to have a decreasing sample decay rate with increasing voltage to engender NDR, indicating once again that the decay path to the sample crucially depends on the electronic wave function of the FER.

While the decay rates can be tuned by changing the out-of-plane confinement of the wave function, the in-plane confinement plays the dominant role in setting an upper bound on the lifetime. Typically, field-emission resonances are delocalized (Bloch-like) in the directions parallel to the surface and thus form bands [176]. In that case, the electron lifetime is affected by interband scattering, wherein the excited electron escapes into the metal (sample or tip), or scatters with an electron in a different band; and intraband scattering, in which case the electron changes velocity [40, 173]. We can expect the introduction of lateral localization to affect decay through these channels in two opposing ways: the increased confinement causes the bands to split into quantized states, strongly attenuating intraband decay, while the simultaneous broadening of the k-space distribution increases the available interband decay paths to the bulk. We assess the degree to which the in-plane confinement precisely affects the lifetime by investigating the transport characteristics of different sized patches.

Performing the same conductance-dependent measurements (see supplementary), we see a marked change in the relative strength of the NDR based on the dimensions of the confining patch, as shown in figure 5.3a. The relative NDR strength, which we define as the ratio of negative area to the total area under the differential conductance spectrum, stays fairly constant as a function of conductance setpoint for patches of larger size, such as the 7×7 and 5×5. In contrast, the smallest patch (2×2) does not exhibit any NDR at low conductance setpoints; at a conductance setpoint of ~0.5 nS, the relative NDR strength becomes non-zero and monotonically increases thereafter. The same general trend holds for the 3×3: exponentially increasing NDR strength with increasing conductance setpoint. In fact, the NDR is directly related to the change in the sample decay rate as a function of voltage, and we can see this variance in Γ_s in the strength and conductance-dependent behaviour of the NDR for the different patches.

As before, to quantify the change in the sample decay rate, we extract Γ_s by fitting equation (5.1) to the first principal FER of each patch, for a discrete range of conductance

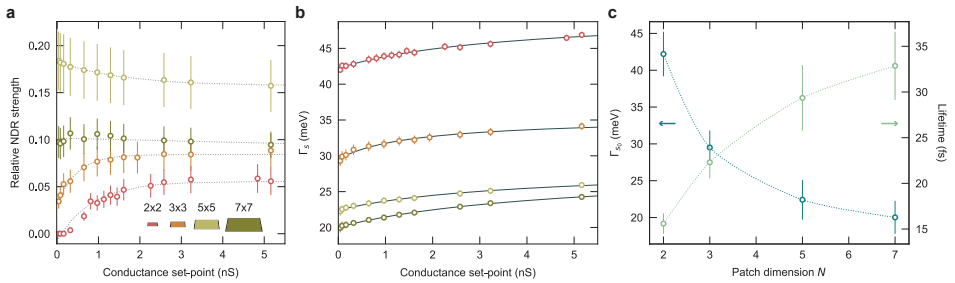

Figure 5.3: **Tuning the lifetime**. **a** Relative strength of the negative differential resistance as a function of conductance setpoint, for patches of various size. Colors correspond to illustration in the inset. Dotted lines are guides to the eye. **b** Conductance-dependence of the sample decay rate for corresponding patch sizes, fitted to an inverse natural logarithmic function (grey solid lines). **c** Extrapolated value of the sample decay rate for zero setpoint conductance (blue circles), and the corresponding lifetime (green circles) for each patch size. Dotted lines are guides to eye.

setpoints (figure 5.3b). We see that both the magnitude of the sample decay rate, and its rate of change over this conductance setpoint range, vary according to patch size. The electrons localized above the smallest patch experience the largest sample decay rates, meaning scattering to the bulk becomes more efficient due to the increased spatial confinement.

The lifetime of these localized electrons, τ, is determined by the tip and sample decay rates, such that $\tau^{-1} = \Gamma_s^{-1} + \Gamma_t^{-1}$. The tip contribution exponentially tends to zero as a function of the tip-sample distance, meaning the intrinsic lifetime (at zero conductance setpoint, namely when the tip is infinitely far away) is determined by the sample decay rate at zero conductance. Approximating the lifetime by the linewidth of the resonance is not valid here, as the potential in the out-of-plane direction changes as we perform spectroscopy, leading to a changing resonance energy as a function of the applied voltage that artificially broadens the peak.

As shown in figure 5.3c, the extracted lifetimes monotonically increase as a function of patch size up to $N = 7$, the maximum patch dimension studied in this work. Notably, the lifetime for the confined states is roughly 2-4 times longer than the lifetime of the first resonance on bare Cu(100), extracted using the same method and in fair agreement with previously reported values (see chapter 7). This also indicates that there must be a patch size with an optimally long lifetime, after which τ begins decreasing with patch size, tending toward the freely-propagating Cu(100) limit. Indeed, the degree to which the confinement prohibits the different decay paths at play is ultimately a delicate balance: the smaller the patch, the fewer states available for scattering between different resonances, but the larger the k-space overlap with the bulk states. Notably, the lifetime-limiting rate for all the patches shown here is Γ_s, which in our case is approximately three orders of magnitude larger than the tip decay rate Γ_t (figure 5.2c).

To better determine the role of the in- and out-of-plane confinement on the lifetime, we investigate the spectral weight of the localized resonances in k-space and compare this to the bulk band structure of copper. We calculate the wave function Ψ, which we assume to be separable, in the directions parallel and perpendicular to the (100) direction

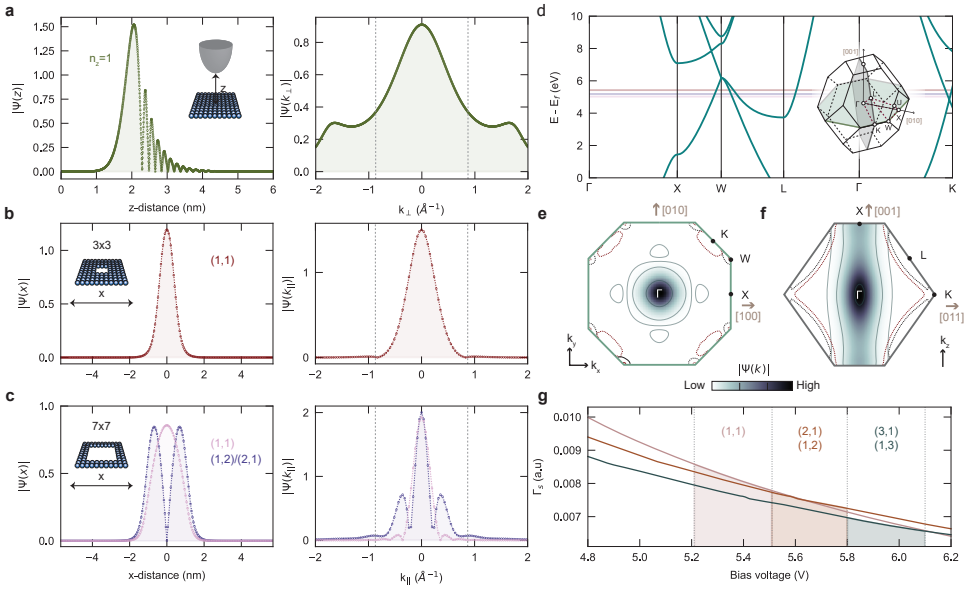

Figure 5.4: **Distribution in k-space**. **a** Calculated out-of-plane component of the real space wave function $|\psi(z)|$ for the first principal FER $n_z = 0$ (left), and the corresponding Fourier transform (right), at tip-sample distance $z = 2.4$ nm. **b**, **c** Calculated in-plane component of the real space wave function (left) for the (**b**) 3×3 (**c**) and 7×7 patches, showing the first $(n_x, n_y) = (1,1)$ (**b**, red; **c**, pink) and second $(1,2), (2,1)$ (**c**, purple) modes, with the corresponding Fourier transforms (right). Dotted lines indicate $\pm\pi/a$ bounds. **d** Bulk band structure of Cu along high symmetry lines, with the experimental resonance energy of the $(1,1)$ state for the 3×3 (red) and 7×7 (pink), as well as the $(1,2)/(2,1)$ state of the latter (purple), denoted by solid lines. Inset: schematic of the first Brillouin zone of Cu. **e, f** Intensity of the 3×3 wave function in k-space across Brillouin zone slices indicated in inset of **d**. Solid contour lines delineate an order of magnitude change in the intensity. Corresponding DFT-calculated constant-energy isolines shown for bulk Cu bands, taken 5 V (black line) and 6 V (red line) above the Fermi level. **g** Calculated sample decay rate as a function of bias voltage, shown for the first three resonances probed in the center of a 5×5 patch, corresponding to the $(1,1)$ (mauve line), $(2,1)/(1,2)$ (brown line), and $(3,1)/(1,3)$ (grey line) modes. The shaded areas correspond to the voltage range in which the respective modes are typically measured, delineating Γ_s in that range.

to obtain the corresponding k-space distribution. First, we consider the out-of-plane direction, where the confinement is set by the tip-sample distance and the applied voltage. We restrict our focus to the calculated wave-function, $\Psi(z)$, for the first principal FER and the resulting Fourier transform, $\Psi(k_\perp)$, shown in figure 5.4a. The $k_\perp$ values with a significant spectral weight span the entirety of the first Brillouin zone (BZ) (± 1.75 Å).

Along the in-plane directions, we consider the wave functions $\Psi(x)$ and $\Psi(y)$ corresponding to the first ($(1,1)$) particle-in-a-box mode for the 3×3 and 7×7 patches (figure 5.4b and c). As expected, the $k_\parallel$-space distribution widens as the patch size decreases. Furthermore, as shown in figure 5.4c, this broadening also takes place when the quantum numbers (n_x, n_y) of the in-plane mode increase. This is due to changes in the apparent barrier height: compare, for instance, the first and second particle-in-a-box modes—since the latter lies at higher energy than the former, it experiences a shallower finite well. Such considerations allow us to visualize how the factors considered so far—

such as the tip-sample distance, the lateral extent of the patch, the apparent height of the in-plane barrier—impact the distribution of the state in k-space, and consequently its overlap with the bulk states.

To better illustrate this, we consider the band structure of bulk copper along the high symmetry lines [177], specifically at the experimental energies of the particle-in-a-box modes (figure 5.4d). The lifetime of the confined electrons depends directly on, and is limited by, the number of bulk states available for direct tunneling—the more bands we cross at the energy of the resonance, with k-values falling within $\Psi(k)$, the shorter the lifetime to first order. In this energy range, we cross several bulk bands along the high symmetry lines (X → W, W → L, L → Γ, Γ → K); however, the efficiency of these decay paths is scaled by the spectral weight of $\Psi(k)$ at the crossing points. In other words, the efficiency of the decay paths is scaled by the probability of having an electron with the right momentum for direct tunneling into that bulk state.

Accordingly, in figures 5.4e and f, we consider the intensity of the k-space wave function along various cross-sections of the first BZ (figure 5.4d, inset). Interestingly, the highest spectral weight is along the Γ → X direction—across both the lateral (figure 5.4e) and vertical (figure 5.4f) cross-sections—relative to the other high symmetry lines; however, this direction does not present any band crossing along the high symmetry lines at the energy of the resonances. In fact, $\Psi(k)$ carries little, if any, spectral weight along the other directions where it does cross the bulk bands. This is illustrated in figures 5.4e and f, where we see that $\Psi(k)$ has practically zero intensity along the energy isosurfaces (at 5 V and 6 V) of bulk Cu, calculated using density functional theory (DFT). This is quite remarkable: although the lateral confinement of the states introduces direct tunneling paths to the bulk that are not present for the laterally freely-propagating case, we can consider the contribution to be minimal in this case. Additionally, the added confinement acts to largely hinder the role of intraband inelastic scattering, as the available states for scattering are substantially reduced: the FERs no longer form bands, but are rather quantized and well-separated in energy, according to the physical dimensions of the patch. These two effects ultimately amount to a considerable enhancement of the lifetime of the confined states.

These considerations also shed light on the dependence of the sample decay rate Γ_s with bias voltage—which, as we previously found, is critical in engendering NDR. Namely: with increasing voltage, the localized resonance is pushed to higher energies, causing a shift in the crossing points with the bulk bands. In turn, this shift translates into the decay channels being scaled by a slightly different spectral weight. To illustrate this effect, we can consider the crossing along the Γ → K direction: as the bias increases, the FER shifts up in energy, meaning that the crossing point for the lower band moves away from the Γ point, closer to the K point. Figures 5.4e and f show that this shift is accompanied by a decrease in the spectral weight of $\Psi(k)$, meaning the total overlap between the localized state and the bulk bands decreases. The emergence of the upper band around ~4.5V, however, further complicates the picture, illustrating that the overall rate of change of the decay rate is hard to estimate. However, by qualitatively considering the evolution of the k-space overlap, we can already grasp the complexity of the dependence of Γ_s on the bias voltage.

To get a quantitative estimate of the change in the sample decay rate, we calcu-

late the weighted k-space wave function overlap for each DFT-calculated crossing point throughout the entire BZ, and relate that to a dimensionless sample-decay rate via Fermi's golden rule (figure 5.4g). For this, we consider the calculated k-space wave function of the 5×5 patch for the first $(1,1)$, second $(2,1)$, $(1,2)$, and fourth $(3,1)$, $(1,3)$ particle-in-a-box modes—the only states with non-zero intensity at the center of the patch (see figures 5.1d and 5.2a). As shown in figure 5.4g, we see that the calculated sample decay rate for all three states monotonically decreases, i.e. that the overlap of $\Psi(k)$ with the bulk bands decreases with increasing voltage, so that $d\Gamma_s/dV$ is negative—the ratio of this rate of change to the intercept is in good agreement with our quantitative results from the double barrier model (figure 5.2). The sample decay rate associated with each state is strictly only applicable in the voltage range in which that state is measured, roughly delineated in figure 5.4g by the shaded areas. All in all, we can confidently attribute the NDR to the effects of the bulk band structure. Additionally, we should also note that the NDR is consistently observed with different tips, and is not observed for laterally propagating FERs (see supplementary) [178, 179], which do not have direct tunneling paths to the bulk available to them.

5.4. CONCLUSIONS

By laterally confining field-emission resonances through atomic assembly of single chlorine vacancies, we present a new platform for creating artificial atoms. We demonstrate control over the lifetime and occupation of these artificial atoms by adjusting the confining potential, implemented via modification of the tip-sample distance or the lateral dimensions of the patch. The ability to tune the occupation is a key parameter of control in the study of quantum many-body states that evolve as a function of the state filling. We show that the lifetime of field-emission resonances, unlike that of surface states, can be prolonged via lateral confinement, up to nearly four times the freely-propagating case. This extension of the lifetime enhances the available energy resolution, and, in conjunction with control over the state filling, is a first step towards studying electron-electron interactions with artificial lattices. Further prolonging the lifetime to approach a state occupation of 1 for reasonable setpoint currents can be pursued via several avenues: such as finding an underlying bulk crystal that hosts FER bands closer to the Fermi energy, or one that is semi-conducting or even insulating. These considerations make confined vacuum resonances a promising platform for creating and studying artificial lattices.

5.5. METHODS

Sample preparation and experimentation were performed in ultrahigh vacuum systems with a base pressure of 10^{-10} mbar (Unisoku USM1300s, SPECS Joule-Thompson-SPM). The Cu(100) crystal was cleaned via repeated cycles of argon sputter at 1 kV and annealing to 600° C. The chlorinated copper surface was prepared by thermal evaporation (2-3 minutes) of anhydrous $CuCl_2$ powder heated to 300° C onto a warm Cu(100) crystal. The crystal was heated to 150° C for ~ 10 minutes before and after deposition [18]. The coverage and sample quality were verified via LEED (where possible) and STM. Atom manipulation of chlorine vacancies was implemented using a procedure previously out-

lined [18]. Differential conductance measurements were performed using standard lock-in detection techniques.

5.5.1. DENSITY FUNCTIONAL THEORY (DFT) CALCULATIONS

To calculate the bulk band structure of Cu, we use plane-wave density-functional theory with a standard ultrasoft scalar relativistic pseudopotential and PBE exchange correlation functional, as implemented in the Quantum ESPRESSO package [180]. Plane wave energy cutoffs were set to 120/1080 Ry (wave function/density). We initialised the atoms on a FCC lattice with lattice constant 3.61 Å. Self-consistent calculation was done on a $4 \times 4 \times 4$ k-point grid and followed by non self-consistent Gamma-point Brillouin zone sampling on a $32 \times 32 \times 32$ k-point grid. The visualization of constant-energy surface cuts was done with FermiSurfer [181].

ACKNOWLEDGEMENTS

The authors thank the Dutch Research Council (NWO) and the European Research Council (ERC Starting Grant 676895 "SPINCAD"). The authors would like to thank Ingmar Swart, Anton Akhmerov, and Michael Wimmer for helpful discussions and insights, as well as Artem Pulkin for guidance with the DFT calculations.

All data presented in this chapter are publicly available with identifier (DOI) 10.5281/zenodo.6473090

5.6. SUPPLEMENTARY MATERIALS

5.6.1. CORRECTION APPLIED TO STACKED dI/dV

The raw constant-height spectroscopy acquired over each patch (Fig. 5.5) shows a general shift of the spectroscopic features to the right as the bias voltage is increased. We attribute this shift to the asymmetric geometry of the tip, which consequently gives rise to an asymmetric tip electric field. To correct for this, we assume that for a given bias voltage, the acquired spectrum should be symmetric and centered. We achieve this by applying a second-order polynomial fit to each constant-voltage line for each patch, and use the global maximum along each slice to set the center point.

5.6.2. MODELLING THE IN-PLANE CONFINEMENT

The engineered lateral confinement of the field emission resonances, which physically arises from the work function difference between the bare and chlorinated Cu(100) surfaces, can be simply modelled using a finite, slanted square potential well. The depth of the potential well is set by the work function difference $\Delta\phi = 1.1 \pm 0.1$ eV between the two surfaces [168]. It is also possible to estimate $\Delta\phi$ from the energy shift of the first field-emission resonance on each surface [171, 172]; this method also yields a difference of roughly 1 V (see figure 1c of the main manuscript). Since the work function change cannot occur with an infinitely sharp slope, we assume the potential well is slanted: we consider that the slope is set by $\Delta\phi$, as well as by the Fermi wavelength of the tunneling electrons, which is roughly 1.5 units cells at 5V.

We calculate the expected energy of the observed resonances by numerically solv-

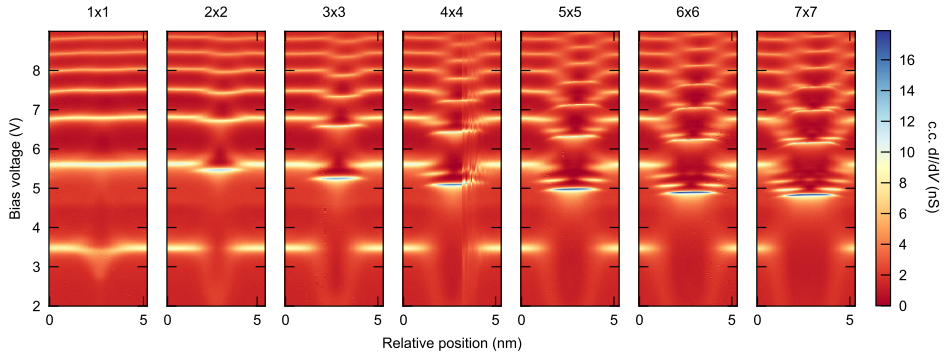

Figure 5.5: Raw, uncorrected stacked constant-current differential conductance spectra obtained at a setpoint of 100 pA, taken along a line crossing the center of each patch, with the respective size indicated at the top.

ing the Schrödinger equation [182] for this potential; this gives us the energy spacing between the main and sub resonances. The total potential landscape, which also has an out-of-plane component, described by the trapezoidal potential barrier at the tip-sample junction, is separable, meaning the eigenenergies for each direction can be simply added. For ease of comparison between the energies calculated for the in-plane confinement and those measured, we subtract the out-of-plane component by defining the energy axis relative to the energy of the first field-emission resonance. As shown in figure 5.6, the comparison between the energies extracted from the measured constant-height $\mathrm{d}I/\mathrm{d}V$ to those obtained numerically is fair. Note that the third in-plane confinement mode is absent in the measured $\mathrm{d}I/\mathrm{d}V$ spectrum obtained at the center of the patch, as this point corresponds to the intersection of the two nodal planes for the $(n_x, n_y) = (2,2)$ state. As such, we also compare the results of the calculations to the energies of the constant-current $\mathrm{d}I/\mathrm{d}V$ maps shown in figure 5.1e—again, we have good agreement.

5.6.3. CONDUCTANCE-DEPENDENT SPECTROSCOPY FOR PATCHES OF DIFFERENT SIZE

We perform conductance-dependent spectroscopy at the center of the 2×2, 3×3, and 7×7 patches (Fig.5.7), in addition to those performed on the 5×5 (Fig. 5.2). In each case, we fit the first resonance using our transport model to extract the sample decay rate shown in Fig 5.3b. We also use these spectra to quantify the relative NDR strength as a function of the conductance setpoint (Fig 5.3a).

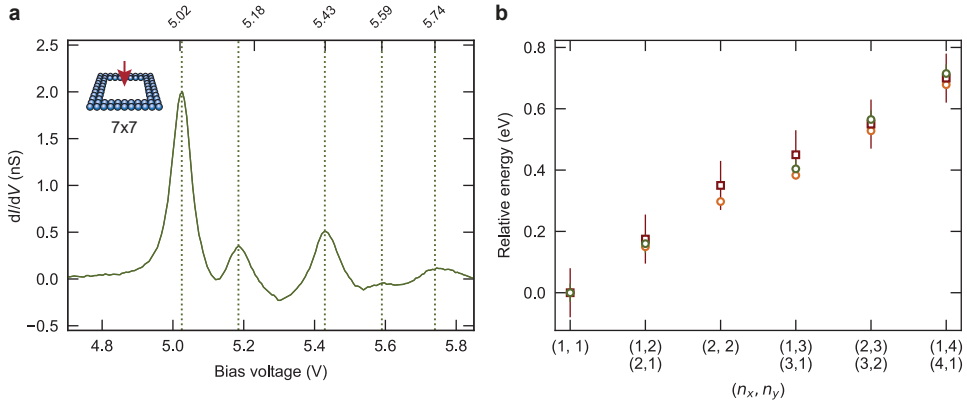

Figure 5.6: Comparison of calculated and measured eigenenergies of the particle-in-a-box states of the laterally confined field-emission resonances. (a) Constant-height differential conductance spectrum (conductance set-point at 250 pA/6.2 V) acquired at the center of the 7 × 7 patch, as indicated in the inset. Dotted lines indicate the energy of the first main resonance (5.02V) and the following sub-resonances. (b) Resonance energies extracted from point spectroscopy performed at the center of the 7 × 7 patch (green circles); we compare this to the energies of the constant-current (100 pA) differential conductance maps (red squares) shown in figure 5.1e, as well as the energy calculated for each state using a finite potential well model (orange circles). In each case, we define the energy axis relative to the energy of the first field-emission resonance.

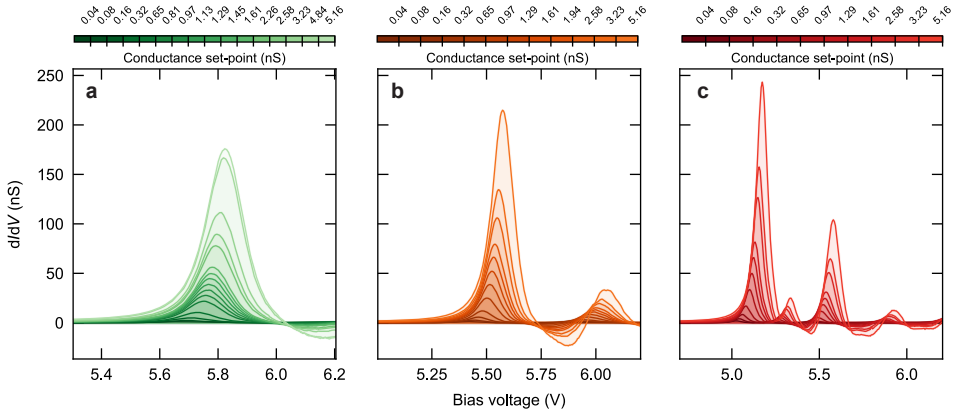

Figure 5.7: **Constant-height differential conductance spectra for patches of various size**. Spectra obtained at the center of the 2 × 2 (**a**), 3 × 3 (**b**), and 7 × 7 (**c**) patches for a range of conductance setpoints ((250 pA → 32 nA),6.2 V) (exact values indicated in the discretized colorbar).

6

COUPLING CONFINED VACUUM RESONANCES

Laterally confined vacuum resonances can be cast as artificial atoms used in the atom-by-atom construction of artificial matter. Here, we address the suitability of this platform to such applications by characterizing the coupling between artificial atoms based on the confinement of these resonances. To achieve this, we construct dimers and trimers of various geometries and deduce the tight binding parameters: our findings indicate that we can span a wide region of parameter space—demonstrating control over the on-site energy, the orbital overlap, and the hopping amplitude—by adjusting the size of the patches, as well as that of the bridging patch connecting them. To determine the feasibility of using these patches as sites in extended architectures, we turn to a well-known and previously studied system: a looped dimerized chain. Our measurements support the existence of a topological domain wall state in the constructed lattice, in agreement with previous studies. Finally, we look to using this platform to study topological edge states in higher energy bands in a diamond chain geometry. We realize such a lattice, and present preliminary results that evidences the presence of an edge state in the p-like manifold. Since the existence of this topological state relies on the constituent sites carrying a non-zero orbital angular momentum, a conclusive measurement of it could experimentally determine whether sites that lack rotational symmetry can be considered to have orbital angular momentum.

Quantum simulation via atomically assembled artificial lattices permits a high degree of control over the relevant interactions and geometries at play, making it possible to realize a number of model Hamiltonians that are otherwise difficult to study in real materials. There are a few popular platforms for realizing atom-by-atom construction of artificial matter, such as surface states that are confined [33] by coordinated molecules [21] or single atoms [36], and single chlorine vacancies on the chlorinated Cu(100) surface [18, 19, 27]. In chapter 5, we presented laterally confined field emission resonances as a viable new basis for constructing extended artificial lattices, noting the particular advantages this platform presents: a tunable lifetime and easy access to higher energy states that host nodal patters reminiscent of atomic orbitals.

In this chapter, we assess how well-suited this platform is to the study of artificial matter. As a first step, we construct and investigate dimers and trimers composed of vacancy patches on the chlorinated Cu(100) surface. We find we can enable and tune the coupling between two patches via a connecting patch of exposed metal. Following previous works [165], we extract the tight binding parameters, such as the on-site energy, the orbital overlap, and the hopping amplitude, additionally quantifying the coupling strength for various dimer geometries. As a proof of concept, we use this platform to realize a well-characterized system—a looped, dimerized chain that is predicted to host domain wall states [19]—and recover the expected behaviour. Having ascertained that confined vacuum resonances behave as expected in larger architectures, we point to potential avenues of interest to explore further, such as a diamond chain lattice that is expected to host topological edge states when the orbital angular momentum of the constituent sites is non-zero.

6.1. HYBRIDIZATION OF CONFINED VACUUM RESONANCES IN A DIMER GEOMETRY

In the context of artificial matter, a lone $N \times N$ patch of assembled chlorine vacancies constitutes a site in the lattice—a role that it is justified in serving on the basis that each patch hosts discretized energy levels, with the corresponding eigenstates resembling the two-dimensional analog of atomic orbitals. However, this semblance is not completely robust in that the notion of orbital angular momentum is not well-defined in the absence of rotational symmetry. As such, an orbital angular momentum quantum number cannot be strictly assigned to these states—yet, the relationship between the rotation operator and orbital angular momentum operator makes it possible to define, in a limited sense, an orbital angular momentum in systems with reduced symmetry (see section 6.5 for details). As such, we will refer to the particle-in-a-box states by their atomic analog, wherein the $(1,1)$ state is referred to as s-like, the $(2,1)$, $(1,2)$ states as p_x-like and p_y-like, respectively, the $(2,2)$ state as d_{xy}-like, and the linear combination $(3,1) - (1,3)$ as $d_{x^2-y^2}$-like.

To determine whether dimers constructed from vacancy patches exhibit signs of coupling, we atomically assemble two 5×5 patches (dimensions defined in unit cells of the chlorine lattice) that are connected via a 2×3 (width $\times$ length) bridging patch that enhances the intrinsic coupling strength, as shown in Fig. 6.1. We perform constant-current differential conductance spectroscopy (normalized via the procedure outlined

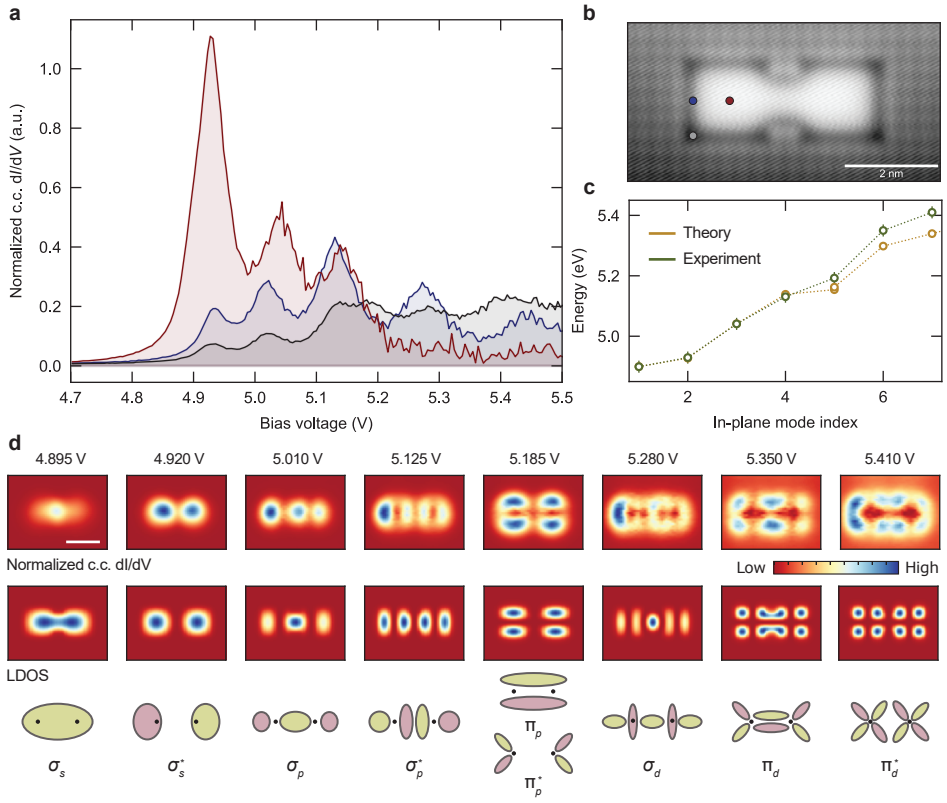

Figure 6.1: **Coupling confined vacuum resonances in a dimer geometry**. **a** Normalized constant-current differential conductance spectroscopy obtained at a current setpoint of 50 pA, acquired at different positions atop a dimer composed of two 5 × 5 patches (indicated in unit cells), connected via a 3 × 2 (width × length) bridging patch. **b** Topography of the dimer (acquired at 600 mV, 1 nA); the locations at which the spectra are obtained is indicated via dots with the corresponding color; scale bar: 2 nm. **c** Extracted experimental resonance energies (green), and corresponding calculated energies (orange) offset by 4.78 V to account for the out-of-plane confinement energy. In-plane mode index refers to the states in **d**, labelled in order of increasing energy. **d** Top row: normalized constant-current differential conductance maps obtained at the indicated energies, the values of which correspond to the approximate locations of the peaks detected in point-spectroscopy. Middle row: Calculated LDOS of the particle-in-a-box states ($|\Psi|^2$), obtained for a finite well with the same geometric configuration as the assembled dimer. Bottom row: schematic of the relevant *s*, *p*, and *d* bonding and antibonding states generated by hybridization between two identical orbitals in each case; position of the nuclei indicated by black circles. The sign of the wavefunction corresponds to its color (positive: green, negative: red).

in chapter 7) at three different points along the dimer (Fig. 6.1a, b). Notably, we observe the emergence of peaks that are engendered by hybridization between the two patches. To trace the full spatial evolution of these states, we perform differential conductance maps at energies corresponding to the peak locations in point-spectroscopy (Fig. 6.1d, top row). The two lowest energy states are reminiscent of the *s* bonding (σ_s) and antibonding (σ_s^*) states, respectively. Namely, the lowest energy state is character-

ized by an electron probability density that has significant intensity along the whole structure, peaking in the very center (symmetric), whereas the second state exhibits a distinct nodal plane between the two patches (antisymmetric).

This analogy to the orbitals of a diatomic molecule continues into the higher energy states (p-like and d-like), where we observe probability distributions corresponding to the p_x bonding (σ_p, at ~ 5.010 V) and antibonding (σ_p^*, at ~ 5.125 V) states. The hybridization of the p_y orbitals (π_{p_x} and $\pi_{p_x}^*$) results in a very small energy splitting, making the two states indistinguishable, as we see in the differential conductance map at ~ 5.185 V. This minimal energy splitting is expected: the p_y bonding and antibonding states are nearly degenerate according to our calculations (Fig. 6.1c, in-plane mode index of 5). At even higher energies, we observe electron probability distributions that have the same nodal pattern as the d-like σ (at ~ 5.280 V) and π (at ~ 5.350 V) bonding states, as well as the π^* antibonding state (at ~ 5.410 V). Additionally, we can reproduce the spatial distributions of all the measured states, as well as their energy spacing, with the calculated eigenstates and energies of a finite potential well that has the same geometry as the constructed dimer, as shown in Fig. 6.1c and d. The well depth here is set by the work function differences between the chlorinated and bare Cu surfaces (~ 1.1 V) [168].

6.2. EXTRACTING THE TIGHT-BINDING PARAMETERS

We follow the same procedure previously outlined [165] for extracting the tight binding parameters for artificial atoms that are coupled via a bridging patch. This connecting bridge introduces certain complications, for instance that coupled patches do not have the same on-site energy as independent ones [165]. Thus, to determine the on-site energies—in addition to the other tight-binding parameters, such as overlap integral, $\mathcal{s}$, as well as the nearest (t_1) and next-nearest (t_2) hopping terms—we atomically assemble and probe dimers and trimers with a given bridging patch geometry (see Fig. 6.2). Furthermore, we restrict our focus to the effects of hybridization on the lowest energy (s-like) states, and assume that the orbital overlap $\mathcal{s}$ is equivalent for dimers and trimers.

With this, the energies of the bonding (E_+) and antibonding (E_-) states arising from the hybridization of s-orbitals in a dimer geometry (see inset of Fig. 6.2a) are given by [165]:

$$E_+ = \frac{\epsilon_1 + t_1}{1 + \mathcal{s}}, \tag{6.1}$$

$$E_- = \frac{\epsilon_1 - t_1}{1 - \mathcal{s}}, \tag{6.2}$$

where ϵ_1 is the onsite energy of each patch comprising the dimer.

Similarly, hybridization in a trimer geometry is expected to give rise to three states with distinct spatial distributions, as schematically illustrated in Fig. 6.2b (inset): the bonding state, at energy E_1, carries intensity across most of the structure; the nonbonding state (E_2) is characterized by zero intensity at the center site; and the antibonding state (E_3) hosts two nodal planes between the inner and outer sites. The energies of

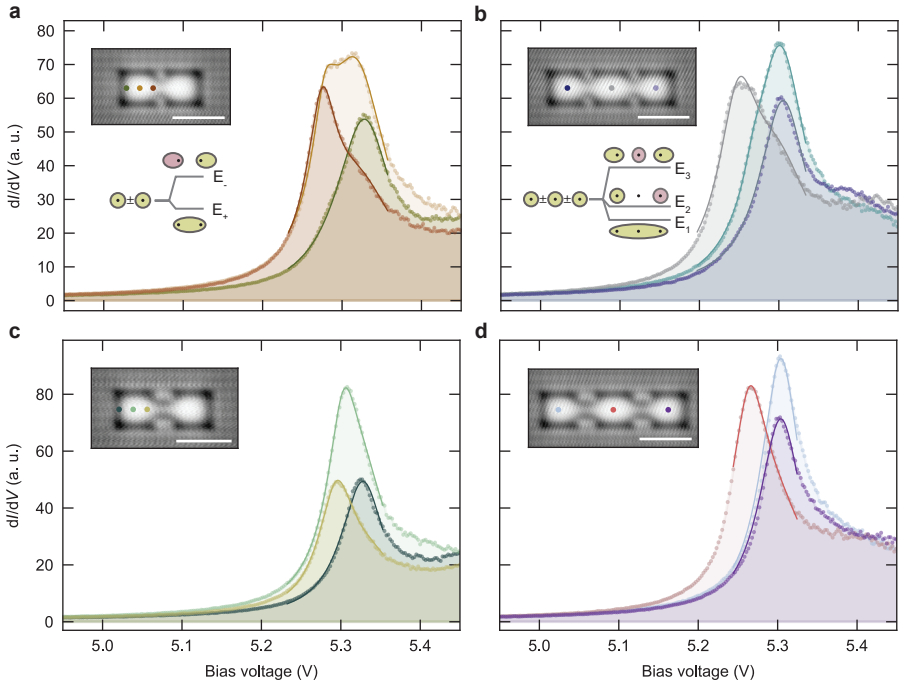

Figure 6.2: **Deducing the tight-binding parameters for dimer and trimer geometries.** **a, c** Normalized constant-current point spectroscopy (circles, shaded), obtained at 100 pA, acquired at various locations atop each dimer (indicated in inset by colored dots; topography recorded at 600 mV, 1 nA; scale bar: 2 nm), composed of two 4×4 patches, connected via a 2×1 (**a**) or 2×2 (**c**) bridging patch. Solid lines are fits of each spectrum to the sum of two Lorentzian functions. Inset (**a**): schematic of the bonding and antibonding orbitals formed (at energies E_+ and E_-, respectively) by hybridization of two identical $1s$ orbitals. The sign of the wavefunction corresponds to its color: positive is denoted by green, and negative by red. **b, d** The same as **a** and **c**, but considering a trimer geometry. Inset (**b**): schematic of the bonding, nonbonding, and antibonding orbitals (at energies E_1, E_2, and E_3, respectively) formed by the hybridization of three identical $1s$ orbitals.

these states are given by:

$$E_1 = \frac{\epsilon_1+\epsilon_2-4\mathcal{O}t_1+t_2-\sqrt{(-\epsilon_1-\epsilon_2+4\mathcal{O}t_1-t_2)^2-4(1-2\mathcal{O}^2)(\epsilon_1\epsilon_2-2t_1^2+\epsilon_2 t_2)}}{2(1-2\mathcal{O}^2)}, \tag{6.3}$$

$$E_2 = \epsilon_1 - t_2, \tag{6.4}$$

$$E_3 = \frac{\epsilon_1+\epsilon_2-4\mathcal{O}t_1+t_2+\sqrt{(-\epsilon_1-\epsilon_2+4\mathcal{O}t_1-t_2)^2-4(1-2\mathcal{O}^2)(\epsilon_1\epsilon_2-2t_1^2+\epsilon_2 t_2)}}{2(1-2\mathcal{O}^2)}, \tag{6.5}$$

where ϵ_1 is the on-site energy of the outermost sites comprising the trimer, and ϵ_2 that of the center site.

We can experimentally deduce these energies (E_+, E_- and E_1, E_2, E_3) using differential conductance spectroscopy performed atop the respective structures. First, we focus on two 4×4 patches strongly coupled by a bridging patch of dimension 2×1 (Fig. 6.2a):

	ϵ_1 (eV)	ϵ_2 (eV)	t_1 (eV)	t_2 (eV)	$\mathfrak{s}$
2×1 bridge	5.28 ± 0.03	5.25 ± 0.03	2.8 ± 0.6	0 ± 0.1	0.5 ± 0.1
2×2 bridge	5.30 ± 0.03	5.27 ± 0.03	2.3 ± 0.5	0 ± 0.1	0.4 ± 0.2

Table 6.1: Tight binding parameters extracted for different bridging geometries.

due to the spatial extent of the bonding and antibonding states (as schematically shown in the inset), we can expect to mainly probe the antibonding state atop the outer patches, and conversely, to dominantly probe the bonding state in the very center. Differential conductance spectroscopy performed at various points along the dimer confirm this, and we are able to clearly resolve two peaks at approximately 5.27 V and 5.33 V (Fig. 6.2a).

Analogously, the distinctive spatial distributions of the bonding, nonbonding, and antibonding states in a trimer geometry allow us to identify their contributions to the differential conductance and extract the energies at which they occur. For instance, differential conductance measurements performed atop the outer patches should mainly be a probe of the nonbonding and antibonding states, as we see in Fig. 6.2b. Similarly, point spectroscopy acquired atop the center patch should mostly carry information about the bonding and antibonding states. By performing measurements at these locations along the trimer, we can indeed resolve these three states at roughly 5.25 V, 5.27 V, and 5.30 V, respectively.

To precisely determine the peak locations, we fit each spectrum acquired atop the dimer (trimer) to the sum of two (three) Lorentzian functions (Fig. 6.2), and use the extracted values to solve the system of equations outlined in Eqs. 6.1-6.5. The resultant tight-binding parameters (Table 6.1) are quite insightful: first off, we can conclusively state that the bridging patches (and the extra area they afford the confined electrons) change the on-site energy according to the coordination number of that site (i.e., $\epsilon_2 < \epsilon_1$); secondly, we can neglect next-nearest neighbour hopping as $t_2 \sim 0$; and most importantly, the dimensional orbital overlap $\mathfrak{s}$ is quite large ($0 \leq \mathfrak{s} < 1$) and cannot be neglected. The magnitude of $\mathfrak{s}$ directly affects the degree to which the energies of the bonding and antibonding states are asymmetrically displaced from ϵ_1 (see insets in Fig. 6.2). Additionally, a non-negligible orbital overlap introduces off-diagonal matrix elements in the Hamiltonian, which means that analytically determining the eigenvalues and eigenstates would require solving a generalized eigenvalue problem—a process that can be carried out by using the Löwdin transformation [183, 184].

6.3. TUNING THE COUPLING STRENGTH

Generally speaking, there are three parameters that we can adjust in order to modify the dimer coupling strength: the size of the constituent patches, as well as the length and width of the bridging patch. To deduce the effects of the bridging length on the tight binding parameters, we investigate the coupling between 4×4 patches connected via a 2×2 bridging patch, as shown in Fig. 6.2c and d. As shown in Table 6.1, a direct comparison between the tight binding parameters extracted for the two geometries—namely, considering a 2×1 (Fig. 6.2a, c) or 2×2 bridging patch (Fig. 6.2b, d)—reveals a decrease in the best estimate of the hopping parameter and the orbital overlap for an

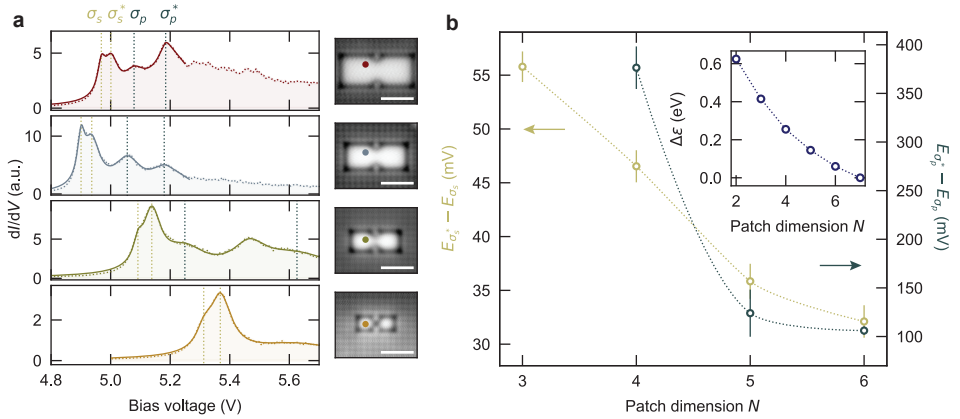

Figure 6.3: **The coupling strength in a dimer geometry, as a function of the patch dimensions**. **a** Normalized constant-current point spectroscopy (circles, shaded) obtained at 50 pA, acquired atop dimers composed of two 6×6 (top row, red), 5×5 (second row, blue), 4×4 (third row, green), and 3×3 (bottom row, orange) patches, respectively. Solid lines are fits of each spectrum to the sum of three (for the 3×3 dimer) or five (for the remaining dimer geometries) Lorentzian functions. Dotted vertical lines correspond to the extracted positions of the σ_s and σ_s^* states (yellow), as well as the σ_p and σ_p^* states (grey), in order of increasing bias voltage. Spectroscopy positions indicated in topography (right column; setpoint of 600 mV, 1 nA; scale bar: 2 nm) by circles with the corresponding color. Spectroscopy performed with different microscopic tips, resulting in an overall shift in the resonance energies—but relative differences are unperturbed. **b** Extracted energy splitting of the s-like (yellow) and p_x-like (grey) bonding and antibonding states, for dimers constructed from two patches of dimension $N\times N$, bridged via a connecting patch of dimension $(N-2)\times1$, as shown in the topographies in **a**, right column. Dotted lines are guides to the eye. Error bars account for uncertainty in the fit parameters only. Inset: change in the on-site energy ϵ for a single patch, relative to the on-site energy for a 7×7 patch, as a function of the patch dimensions N.

increased bridging length, but the associated errors undermine any robust quantitative conclusion.

As such, we take a qualitative approach for estimating the role of the dimer geometry on the coupling, where we take the energy spacing between the bonding and antibonding states as a first-order approximation of the coupling strength; this approximation neglects variations in the orbital overlap, which also impacts the energy spacing and should be taken into account for a more accurate analysis. First, we focus on isolating the effects of the patch size on the coupling by constructing a series of dimers comprised of two patches of dimension $N\times N$, connected via a bridging patch of dimension $(N-2)\times1$, as shown in Fig. 6.3a. Based on the spatial distribution of the hybridized states (Fig. 6.1d), we perform differential conductance spectroscopy in the top right quadrant of the left $N\times N$ patch to ensure we can simultaneously probe every state—this amounts to avoiding the nodal lines, where the spectral intensity goes to zero. We perform Lorentzian fits to the normalized spectra to extract the positions of the bonding and antibonding states; we confirm the expected spatial distribution of these states via differential conductance maps taken at the corresponding energies, as in Fig. 6.1.

As we see in Fig. 6.3b, the energy splitting between the hybridized states monotonically decreases with patch size. Since the on-site energy of an individual patch decreases

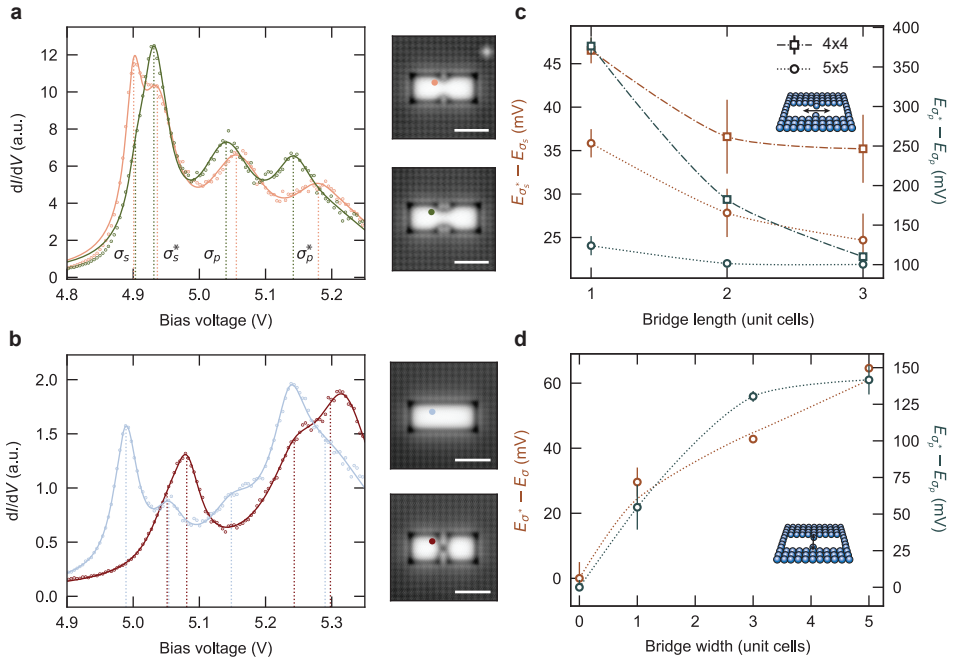

Figure 6.4: **The coupling strength of the s-like and p_x-like states of a dimer, as a function of the bridging geometry**. **a, b** Normalized constant-current point spectroscopy (circles) acquired at 50 pA, performed atop dimers composed of two 5 × 5 patches, connected via bridging patches of varying length (**a**; $3x1$ (orange), $3x2$ (green)), or width (**b**; $5x1$ (blue), $1x1$ (red)). Solid lines are fits of each spectrum to the sum of m Lorentzian functions, where m corresponds to the number of peaks detected in this voltage range; dotted vertical lines are the energies of the σ_s, σ_s^*, σ_p, and σ_p^* states (in order of increasing energy), as extracted from the Lorentzian fits. Right column: corresponding topographic maps (recorded at 600 mV, 1 nA; scale bar: 2 nm) with spectroscopic locations indicated by the color-coordinated circles. **c, d** Extracted energy splitting of the s-like (brown) and p_x-like (gray) bonding and antibonding states as a function of the bridging patch length (**c**) or width (**d**), as shown in inset schematics. **c** Values extracted for distinct dimer geometries composed of two patches, either of dimension 4 × 4 (square markers) or 5 × 5 (circular markers), connected by a bridging patch of fixed width (2 or 3 unit cells, respectively). **d** Now considering a dimer geometry composed of two 5 × 5 patches (circular markers) connected via a bridging patch of fixed length (1 unit cell). Dotted lines in **c** and **d** are guides for the eye. Error bars only account for uncertainty in the fit parameters.

with the patch dimension N (see Fig. 6.3b, inset), it follows that the coupling strength decreases as well. One way to understand this is by considering that the effective depth of the potential well generated by a lone patch is deepened as N is increased (see chapter 5), meaning that the lowest energy state (s-like) experiences an increasingly heightened potential barrier, which in turn decreases the extent of the wave-function outside the well. Additionally, the energy difference between the σ_p and σ_p^* states is larger than for the s-like states, a finding that can be rationalized in the same way: the hybridized p_x-like states, which are at higher energies than the hybridized s-like states, experience an effectively lower potential barrier. Finally, the overall dimensions of the dimer can cause a reordering of the states when comparing structures of various size—this occurs

for the 4 × 4 dimer (Fig. 6.3a, green), where the p_y-like bonding/antibonding states (effectively degenerate, at ~ 5.47 V) are lower in energy than the p_x antibonding state (at ~ 5.62 V), in line with our LDOS calculations for this dimer.

In order to elucidate the role of the bridging patch dimensions in determining the coupling strength, we restrict our attention to dimers composed of two 5 × 5 patches, as shown in Fig. 6.4. We either keep the bridge width (Fig. 6.4a) or length (Fig. 6.4b) fixed, in order to trace the effects of changing the other dimension. As before, we extract the energy of the states from fitting normalized differential conductance spectra obtained for each dimer geometry to a sum of Lorentzians.

As expected, bringing the two patches further apart (i.e., increasing the bridge length) or decreasing the bridge width have a similar effect: an overall decrease in the energy splitting between both the s-like and p_x-like bonding and antibonding states (Fig. 6.4c and d, circular markers). That said, the energy difference between the σ_p and σ_p^* states decreases at a much faster rate (with respect to a changing bridge width or length) than for the s-like states. We can understand this by again considering the increased spatial extent of the p_x-like states outside of the patch, as compared to the s-like. Notably, two 5 × 5 patches one lattice site apart—without a bridging patch to connect them—do not exhibit any measurable coupling within the experimental energy resolution; in this case, we can only set an upper limit to the splitting (≤ 8 mV), which is determined by the energy broadening caused by the lock-in modulation voltage and the measurement temperature (Fig. 6.4d).

The same analysis performed for dimers composed of 4 × 4 patches (Fig. 6.4c, square markers) with a fixed bridge width (two unit cells) and variable bridge length shows the same monotonic decrease in the energy splitting between the bonding and antibonding states. However, as the overall length of the dimer is increased (by increasing the bridge length), the decrease in $E_{\sigma_p^*} - E_{\sigma_p}$ is much larger, and accompanied by a change in the order of the hybridized states: for bridge lengths of more than two unit cells, the p_y bonding/antibonding state is raised in energy above the p_x antibonding state.

6.4. COUPLING CONFINED VACUUM RESONANCES IN EXTENDED LATTICES

Having demonstrated and characterized the hybridization of confined field emission resonances in dimer and trimer geometries, we now turn our focus to their study in extended architectures. Due to the nature of field-emission resonances, and particularly their critical dependence on the out-of-plane confinement, their hybridization in larger lattices is not necessarily implied. Consider an extended one-dimensional chain comprised of vacancy patches: when the tip is above a given patch, the out-of-plane confinement experienced by any of the subsequent patches varies laterally due to the tip shape [178]. This change in confinement means that the resonance energies shift laterally, perhaps negating the possibility of hybridization in larger lattices that exist on length scales comparable to the tip radius. Thereby, we test our platform against a well studied system: a dimerized chain of atoms.

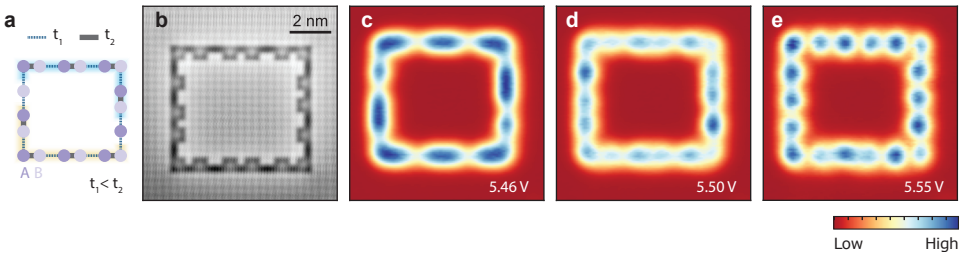

Figure 6.5: **Domain walls in a dimerized looped chain**. **a** Schematic of the looped SSH chain realized experimentally. Alternating weak (t_1) and strong (t_2) coupling between the dimerized sites, with sublattices A (dark purple) and B (light purple) denoted. The two types of unit cell gives rise to two distinct phases, denoted by shaded areas (yellow and blue), engendering a domain wall at their boundary. **b** Topographic map (600 mV, 1 nA) of the assembled SSH loop, composed of artificial atoms of dimension 2×2, connected via a bridging patch of dimension 1×2 (t_1) or 1×1 (t_2). **c–e** Normalized constant-current differential conductance maps obtained at 50 pA, at the indicated bias voltage.

6.4.1. SU–SCHRIEFFER–HEEGER (SSH) CHAIN

One of the simplest frameworks to support topological states is the Su–Schrieffer–Heeger (SSH) model, which takes a tight-binding approach towards describing a one-dimensional dimerized lattice characterized by its staggered hopping amplitudes, t_1 and t_2 [185]. The alternating strong and weak bonds lead to an energy gap opening—the width of which scales with the difference of the two hopping amplitudes—that separates the bulk bands [186]. Notably, this dimerization can occur in solid state systems naturally; the most relevant example being polyacetylene, which experiences staggered hopping amplitudes due to the Peierl's instability [187], and is the molecule for which the SSH model was originally developed [185, 188].

While the gap opens whenever $t_1 \neq t_2$, it their relative amplitude that determines whether the boundaries of a finite dimerized chain are trivial or topological: if the intracell hopping is larger than that of the intercell, all the energy eigenstates of the chain are the same as those of the bulk. However, if the reverse is true, then the ends of the chain host a single eigenstate at zero energy, in the middle of the bulk gap—these are topologically protected edge states. The same principle can lead to domain wall states in a looped SSH chain (see Fig. 6.5a), where the relative strength of the hopping amplitudes is switched mid lattice to create an isolated state at the boundary.

The isolated end state is topologically protected by the chiral (or sublattice) symmetry of the system. This kind of symmetry entails that the Hamiltonian only induces transitions between the two sublattices (not within the same sublattice), thereby lending the Hamiltonian a strictly block off-diagonal form in the chiral basis. Consequently, a topological end state on one sublattice is robust against variations in the other sublattice, such as fluctuations in the on-site energy.

SSH chains have been realized and studied across different experimental platforms [16, 17, 189], including via atomic assembly in the STM-based approach towards artificial lattices [2, 19, 25, 26]. These STM studies have experimentally realized and ascertained various aspects of the SSH model—such as the existence of the topological end state for a prototypical dimerized chain [19], and different extensions involving trimer and coupled

dimer chains that aim at tuning the energy of the topological states [25]. Here, we recreate the looped SSH chain previously studied [19] using 2 × 2 patches (see section 6.7.1), and perform differential conductance maps to determine whether the expected domain walls can be observed with an artificial lattice based on coupling confined field emission resonances.

As shown in Fig. 6.5, a differential conductance map obtained at 5.5 V reveals a heightened intensity localized at the domain wall sites; $\mathrm{d}I/\mathrm{d}V$ maps obtained at bias voltages above and below this value (~5.46 V and ~ 5.55 V) are instead characterized by a mostly even intensity across all sites, as expected. However, while the domain walls host a locally pronounced LDOS at 5.5 V, this is accompanied by a non-negligible intensity across the other sites as well—for a true in-gap state, we expect this intensity to be strictly zero. Three considerations can help make sense of this: firstly, the linewidth of the confined resonances (~ 150 mV) is larger than the energy spacing between these states; secondly, a non-negligible orbital overlap can cause hybridization between the in-gap states and the bulk states; and thirdly, the addition of the bridging patches causes a slight decrease in the on-site energy of the isolated sites as compared to the bulk, which is not accounted for by the normal SSH model (where the on-site energies are all assumed to be equivalent).

In order to evaluate how significant this variation in the on-site energy is, we can make use of the tight binding parameters extracted for 5 × 5 dimers—although we can expect the exact values for the hopping and on-site energies to change for dimers constructed from 2 × 2 patches, this should suffice for a rough estimation. From Table 6.1, we can estimate the change in the on-site energy of the end sites to be roughly 1% of the hopping strength—a minimal shift, that when accounted for does not notably impact the expected eigenstates and energies of a typical SSH chain (see Fig. 6.8, section 6.7.2). With these considerations in mind, our results indicate that hybridization of confined vacuum resonances does occur as expected in extended structures.

6.5. OUTLOOK: SIMULATING TOPOLOGICAL STATES IN HIGHER ENERGY BANDS

Artificial lattices are an experimental tool for the realization and study of exotic states of matter [3], and have been applied in this context to topological states across various architectures [28, 160, 164], such as the Lieb [19, 20], Kagomé [23], and Kekulé lattices [21, 24], as well as quasi-one-dimensional chains [25, 26, 190]—but it is worth noting that these works have mostly focused on the lowest energy (*s*-like) bands. Here, lateral confinement of field-emission resonances allows us to readily access states with *p*-like character, making the study of topological states in higher energy bands an interesting avenue for exploration.

A possible system for such study is a so-called diamond chain constructed from sites with non-zero orbital angular momentum, which is expected to host a topologically nontrivial band structure as well as protected edge states [191]. In this geometry (see Fig. 6.6a), the unit cell is comprised of a central site A and two equidistant neighbouring sites B and C, with an angle $\theta = \pi/2$ between them; all sites have orbital moment given by $m_\ell = \pm 1$. We note that the orbital angular momentum is only defined in the out-

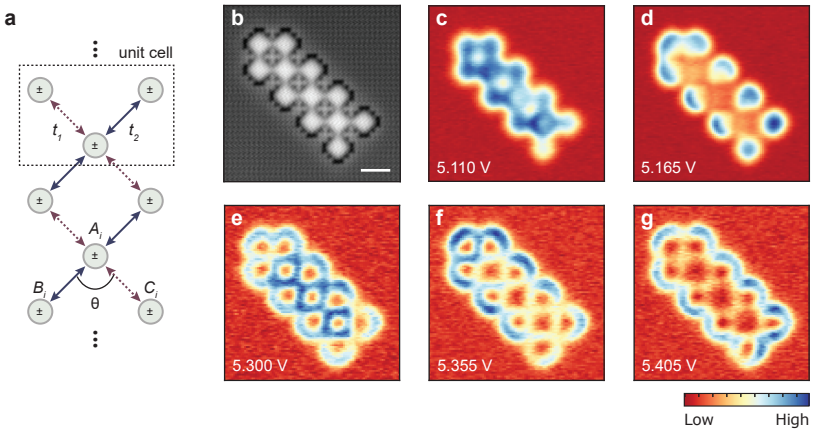

Figure 6.6: **Experimental realization of a diamond chain**. **a** Schematic of the diamond chain lattice. The unit cell is comprised of three sites with an angle $\theta = \pi/2$ between them, where the distance between the central site A and the two neighbouring sites (B and C) is the same. Each site carries orbital angular momentum, resulting in the two $m_\ell = \pm 1$ states. The double-arrow solid lines indicate directions in which all the hopping amplitudes are purely real, whereas the dashed lines denote the directions along which a change in helicity results in a complex hopping phase factor. **b** Topography of the assembled diamond chain lattice, comprised of 4×4 patches connected by 2×1 bridging patches (600 mV, 40 pA). **c–g** Constant-current differential conductance maps obtained at a current setpoint of 50 pA, at the indicated bias voltage.

of-plane direction, such that $L_z|\psi\rangle = \hbar m_\ell |\psi\rangle$, where $m_\ell = 0, \pm 1, \pm 2, \ldots$ [192, 193]. This means there are two states to occupy at each site, denoted by $|j_i, \pm\rangle$, where $j = A, B, C$, i is the index of each unit cell, and $\pm$ refers to helicity of the state.

Consequently, hopping from one site to another can be accompanied by a change in helicity, which in general introduces a relative phase in the hopping [194] that is given by $e^{i\phi_0 \Delta m_\ell}$, where Δm_ℓ quantifies the change in helicity ($\Delta m_\ell = 0, \pm 2$ here) and ϕ_0 is the azimuthal phase origin [191]. In a two-site unit cell, the phase origin can always be defined along the line connecting the two sites, such that $\phi_0 = 0$ and the relative hopping phase is equal to one [194]. In a three-site unit cell, however, the relative phase factor assumes a complex value: in this case, the choice of phase origin will always leave a relative angle between at least one of the neighbouring sites and the central site [191, 194]. If, for instance, the phase origin is chosen along the line connecting A to B, then a relative phase of $e^{\pm 2i\theta}$ is incurred when hopping between states of different helicity in sites A and C [191, 194]. These phases are a natural consequence of the azimuthal component of the wavefunctions for states with non-zero orbital angular momentum, and can be adjusted via geometric modifications of the three-site unit cell [191, 194].

A consequence of this complex hopping in the three-site unit cell is a topologically non-trivial band structure, characterized by a flat band at zero energy (considering a zero on-site energy) and an energy gap that scales with the amplitude of the hopping; if the sites have no orbital angular momentum, the flat, zero energy band persists, but the two remaining bands close at $k = \pm \pi / a$ [191]. Additionally, the $m_\ell = \pm 1$ case is expected to host topologically protected edge states [191, 195] that vanishes in the $m_\ell = 0$ case (in the absence of an external magnetic field) [196].

We construct such a lattice from 4×4 vacancy patches connected by a 2×1 patch (see Fig. 6.6b). We try to account for the shift in the on-site energy induced by the bridging patches by slightly modifying the geometry of the lattice to have the same number of bridging patches per site; however, due to the width of the bridging patch used here, it is not possible to make each site completely identical. Another factor here is whether the p-like states observed for the lone patches can be considered to host a non-zero orbital angular momentum, which is an essential ingredient in the proposed model. Strictly speaking, the orbital angular momentum operator does not have well-defined eigenvalues in the absence of rotational symmetry; however, systems with n-fold symmetry can be considered to have an effective, non-zero orbital angular momentum up to (but not including) $n-1$, given the relation between the orbital angular momentum operator and the rotation operator [197, 198].

The most general definition of the orbital angular momentum operator is as a generator of rotations, a role which we can deduce from its definition $L_{\hat{\eta}} = i\hbar\partial_\phi R(\hat{\eta},\phi)\big|_{\phi=0}$, where $R(\hat{\eta},\phi)$ is the rotation operator acting about an axis $\hat{\eta}$ by an angle ϕ [197, 198]. The rotation operator is itself defined by $R(\hat{\eta},\phi) = \exp(-i\phi L_{\hat{\eta}}/\hbar)$, meaning that in general, the orbital angular momentum operator and rotation operator share eigenstates. While the four-fold symmetry of the confining potentials precludes a general, well-defined concept of the orbital angular momentum operator, let us focus solely on the $(2,1)$, $(1,2)$ particle-in-a-box states (see chapter 5), which correspond to the p_x-like and p_y-like states: here, $R(\hat{z},\pi)|\psi\rangle = -|\psi\rangle$ which supports the solutions $L_z|\psi\rangle = \pm\hbar|\psi\rangle$, where $\hat{z}$ is the out-of-plane direction. The same thinking can be applied to other states, but the four-fold symmetry of the patch means that eigenstates of the potential are also eigenstates of the rotation operator for a maximum rotation of $\pi/2$. In this limited scope, we can think of these states as having a non-zero orbital angular momentum up to the symmetry permitted by the confining potential.

Preliminary differential conductance maps obtained at energies corresponding to the s-like states (Fig. 6.6c and d) are either characterized by a roughly even intensity across all sites (5.110 V) or at the sites along the lattice boundary (5.165 V), presumably corresponding to the bulk and flat bands in the infinite chain limit. At higher energies, we probe the p-like states: the maps obtained at 5.3 V (Fig. 6.6e) and 5.405 V (Fig. 6.6g) are quite analogous to the s-like states (at 5.110 V and 5.165 V, respectively), in that the former is characterized by an increased intensity across the bulk and the latter by a pronounced intensity along the edges. However, the p-like manifold has an additional state at 5.355 V (Fig. 6.6f) that is absent at lower energies, and which features a localized and increased intensity at the end of the chain, as expected from the topological edge state. It is worth repeating that this state should only appear in the p-like manifold, as it relies on each site carrying a non-zero orbital angular momentum—as such, it is promising that we do not seem to observe it when probing the s-like manifold.

Another point of consideration is the role of the orbital overlap: since the overlap is not negligible (section 6.2), we can expect it to induce some hybridization between the edge state and the bulk states. Future experimental realizations would benefit from making use of a smaller bridging patch (of dimension 1×1, for instance), which should decrease the strength of the orbital overlap. Indeed, additional measurements performed at constant tip-sample distance and further theoretical checks are necessary to conclu-

sively comment on any of the observed behaviour here, but we believe this is a promising first step toward realizing and studying topological states in higher energy bands using confined field emission resonances.

6.6. CONCLUSIONS

In this chapter, we demonstrate that confined field emission resonances are well-suited to the study of artificial lattices. Specifically, we show that vacancy patches assembled into dimer geometries hybridize to engender *s*-like and *p*-like bonding and antibonding states. We characterize the coupling strength across various dimer architectures and extract the tight binding parameters, such as the on-site energy, the orbital overlap, and the hopping amplitude, where applicable.

Having ascertained that the patches hybridize, we implement them in a well-studied lattice as a proof of concept; to this end, we construct a looped SSH chain that is expected to host topological domain wall states. Differential conductance measurements atop the structure corroborate the existence of such states, indicating that this platform can be used to realize and study artificial lattices. Finally, we point to interesting avenues to explore further, such as the diamond chain, where the different orbital character of the states is exploited in an effort to probe topological states in higher energy bands.

ACKNOWLEDGEMENTS

We would like to thank Hélène Spring, Maura Willems, and Laëtitia Farinacci for their contributions to this work.

6.7. SUPPLEMENTARY MATERIALS

6.7.1. CHARACTERIZING DIMERS COMPRISED OF 2 × 2 PATCHES

In order to characterize the building blocks used to construct the looped SSH chain (see section 6.4.1), we construct and investigate dimers comprised of two 2 × 2 patches, connected via an off-center bridging patch of dimension 1 × 1 or 1 × 2 (see Fig. 6.7). Point spectroscopy performed atop the 1 × 1 bridged dimer reveals a double peak (Fig. 6.7b), and differential conductance maps obtained at the peak locations indicate that the spatial distribution of these states correspond to the *s*-like bonding (5.33 V) and antibonding (5.64 V) states (Fig. 6.7c). Point-spectroscopy performed atop the 1 × 2 bridged dimer is much the same (Fig. 6.7e), with the distinction that the bonding and antibonding states here are closer in energy due to the weaker effective coupling.

6.7.2. VARYING THE ON-SITE ENERGY IN THE SSH MODEL

To closely examine how variations in the on-site energy take shape in the SSH model, we calculate [182] the eigenergies and eigenstates of a finite one-dimensional dimerized chain, where $t_1 = 0.5$ and $t_2 = 1$. To mimic the experimental conditions, we vary the on-site energy of the isolated end sites (setting this parameter equal to 0 eV, -0.1 eV, or -0.3 eV), while keeping all other on-site energies equal to zero. As shown in Fig. 6.8a, this change in the on-site energies of the end sites causes the states in the gap to shift downward in energy, away from zero energy point. The corresponding calculated eigenstates

do not appreciably change, despite these variations (Fig. 6.8b).

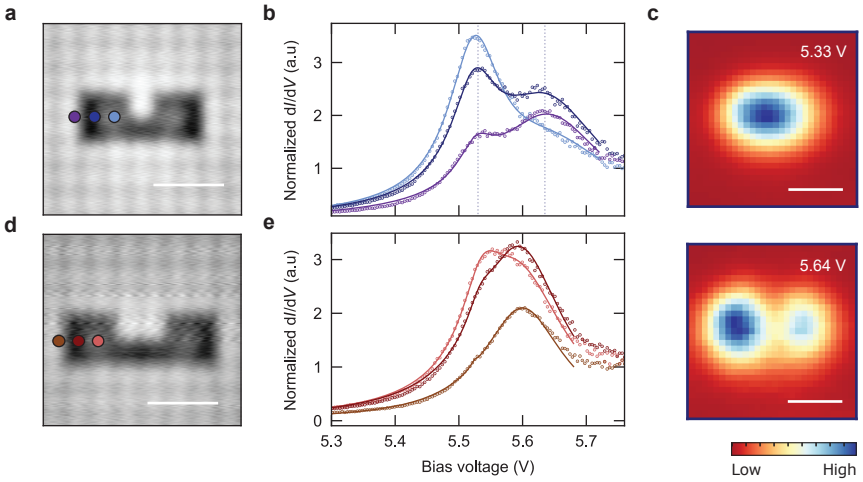

Figure 6.7: **Hybridization of *s*-like states in dimers constructed from 2 × 2 patches**. **a, d** Topography (600 mV, 1 nA) of the assembled dimers, comprised of two 2 × 2 patches connected via an off-center bridging patch of dimension 1 × 1 (**a**) or 1 × 2 (**d**). **b, e** Normalized constant-current differential conductance spectroscopy obtained atop the 1 × 1 bridged dimer (**b**) and the 1 × 2 bridged dimer (**e**)) at a current setpoint of 50 pA; location of each spectrum indicated on the topographic maps by circles with the corresponding color. Solid lines are fits to the sum of two Lorentzian functions. Dotted lines (panel **b**) correspond to 5.33 V and 5.64 V. **c** Normalized constant-current differential conductance maps of the 1 × 1 bridged dimer, obtained at 50 pA.

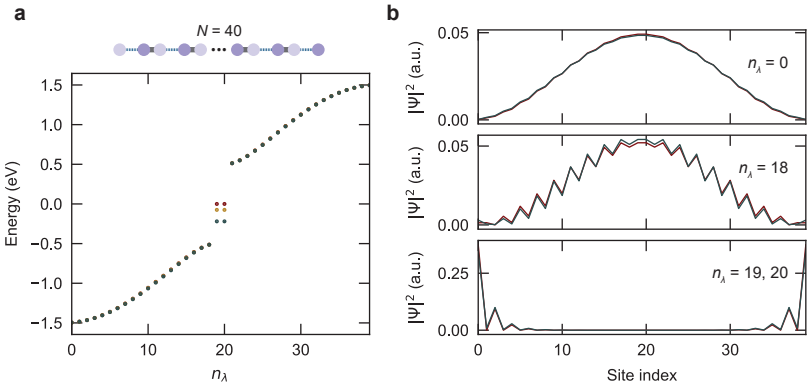

Figure 6.8: **Varying the on-site energy of the end sites in the SSH model**. **a** Top: schematic of a finite SSH chain ($N = 40$ sites) for which calculations were performed; hopping amplitudes given by $t_1 = 0.5$ eV (dotted line) and $t_2 = 1$ eV (solid line); sublattices A (dark purple) and B (light purple) indicated. Calculated energies versus the spectral index (n_λ) for the illustrated dimerized chain. Calculations performed for three distinct scenarios: all on-site energies are taken to be equal to zero (red); or, on-site energies of the end-sites are set to -0.1 eV (yellow) or -0.3 eV (grey), with all other on-site energies still equal to zero. **b** $|\Psi|^2$ corresponding to the indicated eigenvalue number, calculated considering zero on-site energy for all sites (red), or by setting the on-site energies of the end sites to -0.3 eV (grey).

7

NUMERICAL SIMULATIONS OF FIELD-EMISSION RESONANCES

Field-emission resonances are sensitive to the electronic structure and morphology of surfaces, making them useful probes of the local surface work function, scattering properties of surfaces, and notably, electron dynamics of unoccupied states. However, scanning tunneling spectroscopy performed in this regime—which entails applying bias voltages exceeding the sample work function—suffers from experimental and theoretical complications pertaining to the resonances' sensitivity to the tunnel barrier: changes in the tip-sample distance or the applied voltage are necessarily accompanied by a redistribution of the wave function and a shift in the resonance energy. As such, the wave functions continuously evolve during spectroscopy, yielding a measurement that is a convolution of these effects with the local electronic density of states. This prevents direct quantitative analysis of differential conductance spectra for determining the properties of these states, such as the electronic lifetime. Here, we present several numerical avenues for the treatment of field-emission resonances, aimed at extracting quantitative information from their spectroscopic features. By accounting for the tunnel barrier in the high bias regime, we simulate the wave functions and energies of the resonances to quantify their evolution as the potential across the tunnel junction is varied. Furthermore, we estimate the transmission through the tunnel barrier to derive how the local density of states and experimentally obtained differential conductance spectra are related to each other, proposing a general normalization procedure for extracting the local density of states from high-bias spectroscopy. Finally, by modelling the transport through the vacuum-localized state, we present a method for determining electronic lifetimes from spectroscopic data. We use this procedure to extract the lifetime of the first field-emission resonance on bare Cu(100), obtaining a value of 8 ± 3 *fs, consistent with previously reported results.*

Parts of this chapter have been published in ACS Nano **16**, 11251–11258 (2022) by R. Rejali, L. Farinacci, D. Coffey, R. Broekhoven, J. Gobeil, Y. M. Blanter, and A. F. Otte [159]; parts of this chapter are in preparation for journal submission by R. Rejali, L. Farinacci, and A. F. Otte.

Field-emission resonances are quantized electronic states localized in the vacuum, between the surface and the probe tip: the linear potential drop across the junction due to the applied bias voltage elevates the potential barrier above the vacuum level of the sample, thereby giving rise to a new class of confined states. In this high electric field regime, tunneling electrons will be reflected both by the sample surface and the rising potential barrier generated by the applied voltage, thus creating standing waves in front of the sample surface. These resonances depend critically on the electronic properties of the sample–such as the surface-projected band structure, which alters the surface reflectivity. As such, they are useful in obtaining information about the surface, such as local work function changes [169–172] or scattering properties at interfaces [199], and even allow for atomically resolved images of insulators [200] and spin-textures [201] far from the surface.

These states also depend on the exact shape of the tunneling barrier: variations in the either tip-sample distance, the tip shape, or the bias voltage cause a change in the confining potential, and consequently alter the energy and probability distribution of the localized states. This presents a challenge in terms of extracting quantitative information from the resonances, as any differential conductance measurement—whether it's performed in constant-height or -current mode—necessarily induces a continual change in the state being probed. In fact, spectroscopy performed in the field-emission regime is, by definition, taken at voltages exceeding the sample work-function and often spanning a wide energy range; as such, the tip is usually nanometers away from the surface, and the tunneling current can easily vary by several orders of magnitude across the energy range of interest. These experimental considerations can make constant-height measurements in this regime highly impractical: the alternative choice of constant-current spectroscopy presents its own challenges, as the measured $\mathrm{d}I/\mathrm{d}V$ in this mode is a poor reflection of the local density of states [113, 114, 202]. Furthermore, the changing level of the localized state during measurement artificially broadens the linewidth of the $\mathrm{d}I/\mathrm{d}V$ peaks, which both limits the available energy resolution and renders the linewidth an inaccurate reflection of the state lifetime.

Here, we address the difficulties in extracting quantitative information from field-emission resonances on three fronts: first, we model the potential landscape across the tip-sample junction to calculate the wave functions and energies of these states, an essential tool in simulating their evolution as the sample properties or tunneling barrier change. Second, we propose and verify a normalization routine for extracting the local density of states from the measured differential conductance in the high-bias regime, for both spectroscopic modes. Finally, we develop a transport model that quantitatively extracts information about the state lifetime from conductance-dependent $\mathrm{d}I/\mathrm{d}V$ measurements, and benchmark our model using a well-known surface, such as Cu(100).

7.1. FIELD-EMISSION RESONANCES: BINDING ENERGIES AND WAVE FUNCTIONS

In general, metal surfaces can host electron states that are absent in the bulk, and which can be categorized according to their spatial probability distribution relative to the surface: intrinsic surface states [203] and image potential states[204, 205]. Intrinsic surface

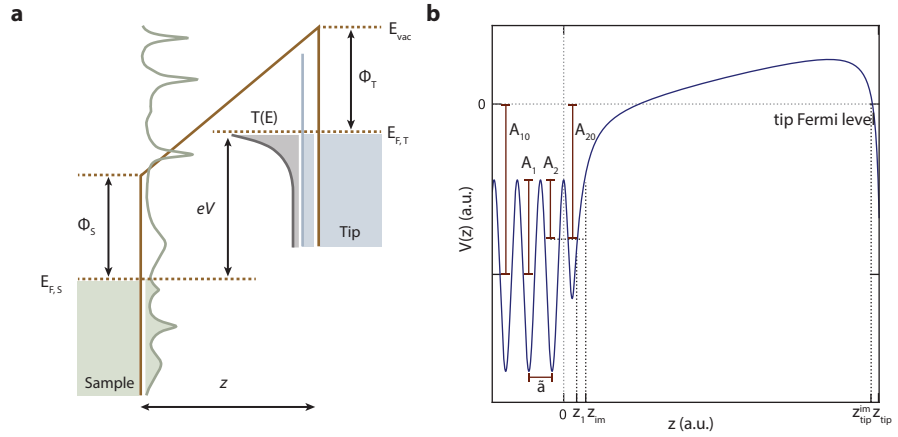

Figure 7.1: **Energy landscape at the tip-sample junction, in the direction perpendicular to the sample surface**. **a** A positive bias voltage applied to the sample shifts the sample Fermi level ($E_{F,S}$) by $-eV$ relative to the tip Fermi level ($E_{F,T}$), creating a trapezoidal potential barrier. This barrier, which depends on the tip-sample distance z, and the work functions of the tip (ϕ_t) and sample (ϕ_s), has an associated transmission factor $T(E)$, which indicates the exponentially decreasing probability that an electron with a certain energy tunnels through the barrier. The Fermi-Dirac distributions of the sample and tip (green and blue rectangles, respectively) are schematically shown for zero temperature. Electrons from the occupied states of the tip tunnel to the empty states on the sample side. The tip density of states (blue line) is assumed to be a constant, while the sample density of states can be expected to vary with energy (schematically illustrated by the green line); both are filled below the respective Fermi levels. **b** The potential used to calculate the energies and wave functions of the field-emission resonances, with the model parameters used to reproduce the bulk band gap (A_1, A_{10}, $\bar{a}$) and the experimental binding energies (A_2 and z_{tip}) defined.

states, also known as Tamm [206] or Shockley states [207], are localized at the surface, whereas image potential states are localized by the Coulomb-like image potential barrier to the region in front of the surface. One way to conceptualize field-emission resonances is as image potential states that are shifted to higher energies by the addition of the linear potential between the tip and sample [175, 208].

While field-emission resonances are particular to the scanning probe geometry, image states are ubiquitous and have been extensively studied using techniques such as inverse photoemission [209] and (time-resolved) two-photon photoemission [173, 210–212]. These works provide reference points for image state binding energies and lifetimes for many noble and transition metals, and have been used to develop one-dimensional models [40, 205] for calculating the energies and wave functions of image states in accordance with these experimental findings. The model used here incorporates the linear potential across the junction and the image potential at the tip side [208], into this existing framework [205] to calculate the wave functions and energies of field-emission resonances.

The total one-dimensional potential across the tip-sample junction accounts for the properties of the bulk, the tunneling barrier, and the work-functions of the tip and sample (see Fig. 7.1) [205, 208]. More specifically, the sample potential ($z \leq 0$) is taken to be periodic in the bulk, with a periodicity set by $a/2$, the distance between two atomic lay-

ers in the out-of-plane direction, where a is the lattice constant. The potential beyond the surface atomic layer is simulated with a potential well ($0 \le z \le z_1$), followed by an exponential decay of the potential towards the tip vacuum level ($z_1 \le z \le z_{\text{im}}$). To account for the tip (at z_{tip}) [208], we add the linear potential $V_{\text{lin}}(z)$ between the tip and sample ($z_1 \le z \le z_{\text{tip}}$), which arises due to the applied voltage and the contact potential. The contact potential is also explicitly accounted for by including the tip (ϕ_t) and sample work functions (ϕ_s). The long-range image potential, $V_{\text{im}}(z)$, which accommodates multiple images in both tip and sample, is also considered, which, all in all, gives rise to the following total potential:

$$V(z) = \begin{cases} A_{10} + A_1 \cos\left(\frac{2\pi}{\bar{a}}\right) & z \le 0 \\ A_{20} + A_2 \cos(\beta z) & 0 \le z \le z_1 \\ V_{\text{lin}}(z) + A_3 \exp(-\alpha(z - z_1)) & z_1 \le z \le z_{\text{im}} \\ V_{\text{lin}}(z) - V_{\text{im}}(z) & z_{\text{im}} \le z \le z_{\text{tip}}, \end{cases} \tag{7.1}$$

where

$$V_{\text{lin}}(z) = E_{f,s} + s(eV + \phi_t) + (1 - s)\phi_s, \tag{7.2}$$

where $E_{f,s}$ is the sample Fermi energy, and $s = (z - z_1)/(z_{\text{tip}} - z_1)$. We chose to define the potential relative to the tip Fermi level, meaning $E_{f,s} = -eV_{\text{bias}}$. Additionally, we can define the image potential as [208]:

$$V_{\text{im}}(z) = \left(1 - \exp(-\lambda(z - z_{\text{im}})\right) \frac{e^2 \left(2\Psi(1) - \Psi(\eta) - \Psi(1 - \eta)\right)}{16\pi\epsilon_0 \left(z_{\text{im}}^{\text{tip}} - z_{\text{im}}\right)}, \tag{7.3}$$

where $\eta = (z - z_{\text{im}})/(z_{\text{im}}^{\text{tip}} - z_{\text{im}})$, e is the electron charge, ϵ_0 the vacuum permittivity, and Ψ the digamma function.

For a terminated metal surface, the parameters A_1 and A_{10} determine the width and position of the surface-projected gap, respectively, whereas the parameters A_2 and β reproduce the experimental values of the binding energies of the image states [205]. We set $A_{10} = -eV_{\text{bias}} - A_1$, as we chose the tip vacuum level as our reference, and assign A_1, A_{20}, A_2, β, and $z_1 = 5\pi/(4\beta)$ to their corresponding values previously determined for a terminated Cu(100) surface [205]. By forcing the potential and its derivative to be continuous everything (except at the tip position, z_{tip}), we can analytically determine the values for the remaining parameters (A_3, α, λ, z_{im}) in terms of already known parameters, using the following analytical relations.

$$\begin{aligned} A_{20} &= A_{10} + A_1 - A_2, \\ A_3 &= A_{20} + A_2 \cos(\beta z_1) - V_{\text{lin}}(z_1), \\ \alpha &= \frac{eV_{\text{bias}} + \phi_t - \phi_s}{A_3(z_{\text{tip}} - z_1)} + \frac{\beta A_2}{A_3} \sin(\beta z_1), \\ \lambda &= 2\alpha, \\ z_{\text{im}} &= \frac{-1}{\alpha} \ln\left(\frac{-\lambda e^2}{16\pi\epsilon_0 A_3}\right) + z_1. \end{aligned}$$

We note that the tip image plane is not well defined in the above potential (and hard to estimate from experiment); luckily, this parameter has little bearing on the calculated wave functions, and can be easily estimated within an acceptable degree (we assign $z_{\mathrm{im}}^{\mathrm{tip}} \approx z_{\mathrm{tip}} - 0.3$ Å.). Solving the time-independent Schrödinger equation [182] using this potential (equation 7.1) results in the calculated wave functions shown in chapter 5.

7.2. OBTAINING THE LOCAL DENSITY OF STATES FROM FIELD-EMISSION SPECTROSCOPY

Scanning tunneling spectroscopy is a tool for obtaining atomically resolved information about the surface-projected electronic density of states as a function of energy. However, the measured differential conductance directly depends on a number of parameters—such as the transmission through the tunnel barrier, the tip density of states, the tip-sample distance, and the finite temperature—which renders it a poor direct measure of the local density of states (LDOS). Several schemes have been proposed for extracting quantitative information from the tunnel current, for instance by considering the static conductance $\mathrm{d}\ln I/\mathrm{d}\ln V$ [96], fitting the differential conductance to a tunneling probability function [213], or normalizing the differential conductance by both the tunnel current and the transmission coefficient [214, 215]. However, these approaches are solely suited for treatment of spectroscopic data obtained at a constant tip-sample distance, for electron energies well below the sample and tip work-functions.

Performing constant-current spectroscopy can be an advantageous choice when, for example, covering large voltage ranges, or when the change in the apparent height of the surface varies drastically–both scenarios necessitate a severe dynamic range of current if the tip-sample distance is held constant. Also, high currents during spectroscopy can sometimes alter or damage molecules or the atomic structure at the surface, as well as induce tip instabilities, in which case it can be preferable to maintain a low and constant current. Unfortunately, constant-current spectra are even further removed from the LDOS than constant-height measurements [113, 114, 202], in part due to the changing transmission through the tunnel barrier, as well as the effects of the tip displacement during data acquisition: for instance, the energy, relative amplitude, and spatial extent of spectroscopic features are significantly affected by changes in tip height [114, 202]. As such, it is even more critical to normalize constant-current spectra to reliably extract quantitative information from the measured differential conductance. While such schemes have been proposed [114, 115, 202, 216], they are limited to low voltage ranges, well below the sample work-function—even though constant-current measurements are most severely needed in the high bias regime.

Here, we present a normalization scheme for extracting the local density of states from spectroscopic data obtained at either constant current or constant tip-sample distance in the field-emission regime. In this approach, we describe the total tunneling current I using the one-dimensional Wenzel-Kramers-Brillouin (WKB) theory, wherein the tunneling barrier is defined by a transmission coefficient, $\mathcal{T}(z, V, E)$, that is both energy- and distance-dependent. In the low temperature limit (where the temperature $T \ll eV/k_B$, and e is the electron charge and k_B the Boltzmann constant), applying a bias voltage V across the barrier leads to a tunneling current at a tip-sample distance z

that is determined by [92, 213, 217]:

$$I(z,V) = \int_0^{eV} \rho_s(E)\rho_t(E-eV)\mathcal{T}(z,V,E)dE, \tag{7.4}$$

where ρ_s and ρ_t are the tip and sample densities of states, respectively, and the proportionality constant relating the current to the integral is set to one. In the above expression, the windowing function determined by the difference of the Fermi-Dirac distributions f of the tip and sample, $f(E-eV)-f(E)$, sets the bounds of integration. Following the expression for the current, the differential conductance can in turn be written as:

$$\partial_V I(z,V) = \partial_V \int_0^{eV} \rho_s(E)\rho_t(E-eV)\mathcal{T}(z,V,E)dE \tag{7.5}$$

$$= e\rho_s(eV)\rho_t(0)\mathcal{T}(z,V,eV) + \int_0^{eV} \rho_s(E)\rho_t(E-eV)\partial_V\mathcal{T}(z,V,E)dE, \tag{7.6}$$

where we apply the Leibniz rule to differentiate the argument of the integral, and approximate the tip density of states be constant with voltage, such that $\partial_V\rho_t = 0$ [115, 214]. To further evaluate the differential conductance, we need an analytical form for the transmission factor in the field emission regime. In this case, the applied voltage is necessarily greater than the sample work function, and we can approximate the tunnel barrier to be triangular, in the region where $eV > \phi_s$, with a transmission factor given by the WKB approximation, wherein the transmission factor $\mathcal{T}$ in related to the integral of the momentum p via $\mathcal{T}(z,V,E) = \exp\left(\frac{-2}{\hbar}\int|p(z')|dz\right)$:

$$-\frac{2}{\hbar}\int_{z_{\text{tp}}}^{z}|p(z')|dz' = -\frac{2}{\hbar}\int_{z_{\text{tp}}}^{z}\sqrt{2m_e\left(\phi_s + \frac{\phi_t-\phi_s+eV}{z}z' - E\right)}dz', \tag{7.7}$$

where the classical turning point is denoted by z_{tp} and the electron mass by m_e [111]. The width of the barrier is given by the tip-sample distance z, and ϕ_s and ϕ_t are the tip and sample work functions, respectively (see Fig. 7.1a). From this we can derive a transmission [111, 218]:

$$\mathcal{T}(z,V,E) = \exp\left(-\frac{4\sqrt{2m_e}}{3\hbar}\frac{z}{\phi_t-\phi_s+eV}(\phi_t+eV-E)^{3/2}\right). \tag{7.8}$$

Here, we note a key and convenient relation [214] between the transmission factor $\mathcal{T}(z,V,E)$

through the tunnel barrier, and its partial derivative with respect to the applied voltage:

$$\partial_V \mathcal{T}(z,V,E) = \partial_V \exp\left(-\frac{4\sqrt{2m_e}}{3\hbar}\frac{z}{\phi_t-\phi_s+eV}(\phi_t+eV-E)^{3/2}\right) \tag{7.9}$$

$$= \mathcal{T}(z,V,E)\times\left(\frac{4e\sqrt{2m_e}}{3\hbar}\frac{z}{(\phi_t-\phi_s+eV)^2}(\phi_t+eV-E)^{3/2} - \frac{2e\sqrt{2m_e}}{\hbar}\frac{z}{\phi_t-\phi_s+eV}(\phi_t+eV-E)^{1/2}\right) \tag{7.10}$$

$$= \frac{2e\sqrt{2m_e}}{\hbar}\frac{z}{(\phi_t-\phi_s+eV)}\left(\frac{2(\phi_t+eV-E)^{3/2}}{3(\phi_t-\phi_s+eV)}-(\phi_t+eV-E)^{1/2}\right)\mathcal{T}(z,V,E). \tag{7.11}$$

By substitution of the above in Eq. 7.6, we arrive at:

$$\partial_V I(z,V) = e\rho_s(eV)\rho_t(0)\mathcal{T}(z,V,eV) + \int_0^{eV}\rho_s(E)\rho_t(E-eV)\mathcal{T}(z,V,E) \times\frac{2e\sqrt{2m_e}}{\hbar}\frac{z}{(\phi_t-\phi_s+eV)}\left(\frac{2(\phi_t+eV-E)^{3/2}}{3(\phi_t-\phi_s+eV)}-(\phi_t+eV-E)^{1/2}\right)dE. \tag{7.12}$$

The arguments of the integrals in Eq. 7.12 and Eq 7.4 are the same, except for the additional factors that relate the transmission to its partial derivative. By noting that these factors are slowly varying in the energy range of interest, and that the transmission itself exponentially peaks at an energy eV, we can set the mean value of these factors to $\frac{4e\sqrt{2m_e}}{3\hbar}\frac{z}{(\phi_t-\phi_s+eV)^2}\phi_t^{3/2}$ and $-\frac{2e\sqrt{2m_e}}{\hbar}\frac{z}{\phi_t-\phi_s+eV}\phi_t^{1/2}$, respectively. We use the generalized mean value theorem [214] to evaluate the integral according to:

$$\partial_V I(z,V) = e\rho_s(eV)\mathcal{T}(z,V,eV) + \frac{4\sqrt{2m_e}}{3\hbar}\frac{z}{\phi_t-\phi_s+eV}\left(\frac{\phi_t^{3/2}}{\phi_t-\phi_s+eV}-\frac{3}{2}\phi_t^{1/2}\right)eI(z,V), \tag{7.13}$$

where we have additionally set the $\rho_t(0)$ equal to unity [214]. Using this expression, we can isolate the density of states from a constant-height differential conductance measurement, performed a distance z_0 from the surface according to:

$$\rho_s(eV) = \frac{1}{e\mathcal{T}(z_0,V,eV)} \times\left(\mathrm{d}_V I(z_0,V) - \frac{4\sqrt{2m_e}}{3\hbar}\frac{z_0}{\phi_t-\phi_s+eV}\left(\frac{\phi_t^{3/2}}{\phi_t-\phi_s+eV}-\frac{3}{2}\phi_t^{1/2}\right)eI(z_0,V)\right). \tag{7.14}$$

If instead we keep the current set-point constant and allow the tip-sample distance to vary, such that $I = I(z(V))$, then the transmission becomes voltage dependent through

$z(V)$ as well. Namely:

$$\mathrm{d}_V \mathcal{T}(z(V),V,E) = \partial_V \mathcal{T}(z(V),V,E) + \mathrm{d}_V z(V)\partial_z \mathcal{T}(z(V),V,E), \tag{7.15}$$

whereby the differential conductance assumes the form:

$$\begin{aligned}\mathrm{d}_V I(z(V)) = {} & e\rho_s(eV)\rho_t(0)\mathcal{T}(z(V),V,eV) \\ & + \int_0^{eV} \rho_s(E)\rho_t(E-V)\left[\partial_V \mathcal{T}(z(V),V,E) + \mathrm{d}_V z(V)\partial_z \mathcal{T}(z(V),V,E)\right] dE.\end{aligned} \tag{7.16}$$

The partial derivative of the transmission with respect to the tip-sample distance $z(V)$ is readily evaluated:

$$\partial_z \mathcal{T}(z(V),V,E) = -\frac{4\sqrt{2m_e}}{3\hbar}\frac{(\phi_t + eV - E)^{3/2}}{\phi_t - \phi_s + eV}\mathcal{T}(z(V),V,E). \tag{7.17}$$

Noting once more that the factors that relate the transmission to its partial derivative with respect to $z(V)$ are slowly varying, we can again apply the mean value theorem to evaluate the integral in Eq. 7.6:

$$\begin{aligned}\mathrm{d}_V I(z(V)) = {} & e\rho_s(eV)\mathcal{T}(z(V),V,eV) \\ & + \frac{4\sqrt{2m_e}}{3\hbar}\frac{z(V)}{\phi_t - \phi_s + eV}\left(\frac{\phi_t^{3/2}}{\phi_t - \phi_s + eV} - \frac{3}{2}\phi_t^{1/2}\right) eI_0 \\ & - \frac{4\sqrt{2m_e}}{3\hbar}\frac{\phi_t^{3/2}}{\phi_t - \phi_s + eV} I_0 \mathrm{d}_V z(V),\end{aligned} \tag{7.18}$$

$$\begin{aligned}= {} & e\rho_s(eV)\mathcal{T}(z(V),V,eV) \\ & + \frac{4\sqrt{2m_e}}{3\hbar}\frac{\phi_t^{3/2}}{\phi_t - \phi_s + eV}\left(ez(V)\left(\frac{1}{\phi_t - \phi_s + eV} - \frac{3}{2\phi_t}\right) - \mathrm{d}_V z(V)\right) I_0,\end{aligned} \tag{7.19}$$

where I_0 is the current set-point. Here, we should note that a measurement of the $\mathrm{d}I/\mathrm{d}V$ at a specific dc-bias amounts to tracking the change in the current caused by the applied bias modulation; correspondingly, the $\mathrm{d}_V z(V)$ term corresponds to the change in the tip-sample separation due to the same ac component of the applied bias. If the frequency of the ac-bias is sufficiently high compared to the cut-off frequency of the feedback, which is normally the case, then $\mathrm{d}_V z(V)$ is negligible [114, 115]. In this case, the density of states can be extracted from the measured differential conductance via:

$$\rho_s(eV) = \frac{1}{e\mathcal{T}(z(V),V,eV)}\left(\mathrm{d}_V I(z(V)) - \frac{4\sqrt{2m_e}}{3\hbar}\frac{z(V)}{\phi_t - \phi_s + eV}\left(\frac{\phi_t^{3/2}}{\phi_t - \phi_s + eV} - \frac{3}{2}\phi_t^{1/2}\right) eI_0\right). \tag{7.20}$$

The relations in Eq. 7.14 and 7.20 can be used to normalize constant-height and constant-current differential conductance spectra, respectively, to obtain the local density of states, in the case where the applied voltage is greater than the sample work-function. This approach relies on recording the differential conductance $\mathrm{d}_V I(z,V)$, the relative tip-displacement Δz, and the current-voltage behaviour $I(V)$ simultaneously. While this is easily and commonly implemented, gaining experimental information about the absolute distance $z = \Delta z + z_0$ requires additional $I(z)$ measurements to estimate the point of contact between the tip and sample.

However, it is in general possible to make a reasonable estimate of this parameter [114]; and in the particular case of field-emission resonances, it is possible to estimate the absolute distance by modelling the out-of-plane potential to match the experimental and calculated energies of the resonances (see section 7.1). In either case, the exact value of z_0 does not dramatically affect the spectral shape of the differential conductance: for a wide range of z_0 values, the peak positions and widths remain roughly constant, while the relative height of the peaks are subject to variation (see Fig 7.2) [114].

7.2.1. EFFECTS OF k-SELECTIVITY IN THE TUNNELING CURRENT

In general, the total tunneling current depends not only on the tunneling barrier, but also on the in-plane momentum $k_\parallel$ of the probed state [88, 89]. In fact, scanning tunneling spectroscopy is mostly sensitive to states with a small in-plane momentum, meaning the total contribution to the current dies off as the $k_\parallel$ of the state increases [219]. This effect has been previously accounted for in the Tersoff and Hamann description of the tunneling current: there, $k_\parallel$ is incorporated into the decay constant that defines the current. Namely, $I \propto \exp(-2\kappa z)$, where $\kappa = \sqrt{2m\phi/\hbar^2 + k_\parallel^2}$, and ϕ is the potential barrier for tunneling [88, 89, 219].

Analogously, the effects of the in-plane momentum can be accounted for in the WKB approach via the transmission factor, namely:

$$\mathcal{T}(z,V,E,k_\parallel) = \exp\left(\frac{-2}{\hbar}\int_0^z \sqrt{2m_e(\phi(z')-E)+\hbar^2 k_\parallel^2}\,dz'\right). \tag{7.21}$$

In the simplest case, where the tunneling barrier is approximated by a rectangular potential ($eV < \phi_s, \phi_t$, necessarily), with an effective tunneling barrier height $\phi_{\text{eff}} = (\phi_t + \phi_s)/2$, the transmission reduces to $\mathcal{T}(z,V,E) = \exp\left(\frac{-2}{\hbar} z\sqrt{2m_e(\phi_{\text{eff}}-E)+\hbar^2 k_\parallel^2}\right)$. The tunneling current in this case is proportional to this transmission:

$$I(V) \propto \mathcal{T}(z,V,E=E_F,k_\parallel)\int_0^{eV}\rho_s(E)\,dE \tag{7.22}$$

$$= \exp\left(\frac{-2}{\hbar} z\sqrt{2m_e\phi_{\text{eff}}+\hbar^2 k_\parallel^2}\right)\int_0^{eV}\rho_s(E)\,dE, \tag{7.23}$$

as in the Bardeen approach. In the above, we consider $\mathcal{T}(z,V,E,k_\parallel) \sim \mathcal{T}(z,V,E=E_F,k_\parallel)$, a common approximation when $eV < \phi_s, \phi_t$, and we set the tip-density of states to unity.

In the field-emission regime, we can similarly incorporate the effects of the in-plane

momentum of the probed state, leading to a transmission factor that depends on $k_\parallel$:

$$\mathcal{T}(z,V,E,k_\parallel) = \exp\left(-\frac{2}{3m_e\hbar}\frac{z}{\phi_t-\phi_s+eV}\left(\left(2m_e(\phi_t+eV-E)+\hbar^2k_\parallel^2\right)^{3/2}-\left|\hbar k_\parallel\right|^3\right)\right), \tag{7.24}$$

where the partial derivative with respect to the voltage is:

$$\begin{aligned}\partial_V\mathcal{T}(z,V,E,k_\parallel) = \mathcal{T}(z,V,E,k_\parallel)\\ \times\left(\frac{2e}{3m_e\hbar}\frac{z}{(\phi_t-\phi_s+eV)^2}\left(\left(2m_e(\phi_t+eV-E)+\hbar^2k_\parallel^2\right)^{3/2}-\left|\hbar k_\parallel\right|^3\right)\right.\\ \left.-\frac{2e}{\hbar}\frac{z}{\phi_t-\phi_s+eV}\left(2m_e(\phi_t+eV-E)+\hbar^2k_\parallel^2\right)^{1/2}\right).\end{aligned} \tag{7.25}$$

Following the same procedure outlined in section 7.2, we can obtain an analytical form for the differential conductance that is analogous to Eq. 7.13:

$$\begin{aligned}\partial_V I(z,V) = e\rho_s(eV)\mathcal{T}(z,V,eV)\\ +\frac{2e}{\hbar}\frac{z}{\phi_t-\phi_s+eV}\left(\frac{\left(2m_e\phi_t+\hbar^2k_\parallel^2\right)^{3/2}-\left|\hbar k_\parallel\right|^3}{3m_e(\phi_t-\phi_s+eV)}-\left(2m_e\phi_t+\hbar^2k_\parallel^2\right)^{1/2}\right)I(V),\end{aligned} \tag{7.26}$$

from which we can isolate the local density of states.

7.2.2. APPLICATION OF NORMALIZATION PROCEDURE TO PEAK-SHAPED SPECTROSCOPIC FEATURES

To test the validity of the proposed normalization schemes, we apply them to constant-current and constant-height spectroscopic data obtained for laterally confined field-emission resonances (chapter 5). As we saw in chapter 5, these particle-in-a-box states carry some finite $k_\parallel$. We can understand this in analogy to the simple case of a one-dimensional infinite potential well, wherein the angular wave number for each state, described by principle quantum number n_{PW}, is given by $n_{\mathrm{PW}}\pi/L$, where n_{PW} is a positive integer and L is the width of the well. This allows us to test both normalization schemes for a system in which $k_\parallel$ is relevant, in addition to inspecting how it compares for open- or closed-feedback measurements.

Ideally, differential conductance measurements performed in either spectroscopic mode—constant-current or constant-height—should yield, via the proposed normalization procedures, identical local densities of states. In Fig 7.2, we show $\mathrm{d}I/\mathrm{d}V$ measurements performed in both modes, and normalize each according to Eqs. 7.14, 7.20 and 7.26 to obtain the local density of states. The extracted LDOS is remarkably similar for the two measurement modes, for both of the normalization schemes proposed

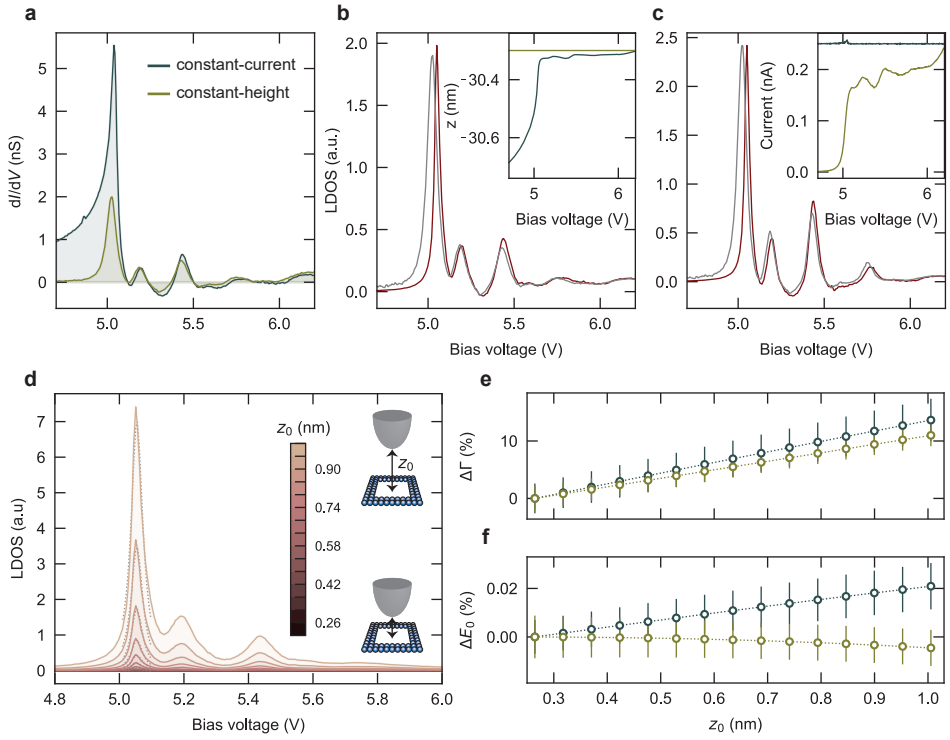

Figure 7.2: **Local density of states extracted from constant-height and constant-current spectroscopic data**. **a** Constant-height (light green) and constant-current (dark blue) differential conductance spectroscopy obtained at the center of the 7×7 patch, at current set-point of 250pA. **b, c** The raw $\mathrm{d}I/\mathrm{d}V$ is normalized to obtain the local density of states, with (c) and without (b) considering the in-plane momentum of the probed state, for both the constant-height (light gray) and constant-current (maroon) measurements. Simultaneously acquired tip-sample distance, offset by z_0 to obtain the absolute distance (b, inset), and current-voltage curve (c, inset), measured during both constant-height (light green, $z_0 \approx 0.2$ nm) and constant-current (grey, $z_0 \approx 0.6$ nm) spectroscopy. **d** Local density of states obtained from normalizing the constant-height spectrum, for a range of z_0 (exact values indicated in the color-bar), as schematically illustrated (inset). Dotted lines are Lorentzian profiles fitted to the first peak. **e, f** Effects of a changing z_0 on the relative peak width Γ (e) and energy E_0 (f) of the first peak in the LDOS, extracted from both constant-current (dark blue) and constant-height (light green) spectra.

here—which either neglect (Fig 7.2b, Eqs. 7.14 and 7.20) or consider (Fig 7.2c, Eq. 7.26) the effects of k-selectivity on the tunnel current. In both cases, the position, relative amplitude, and width of the peaks in the extracted LDOS are quite consistent, although the first peak appears sharper and slightly shifted for the constant-current normalized spectrum; this is likely due to the drastic change in the tip-sample distance around this resonance, a feedback response that cannot be completely rectified by the normalization scheme.

Explicitly considering the in-plane momentum of the probed states $k_\parallel$ (Fig 7.2c) only affects the relative amplitudes of the resonances, as expected. Since the tunneling cur-

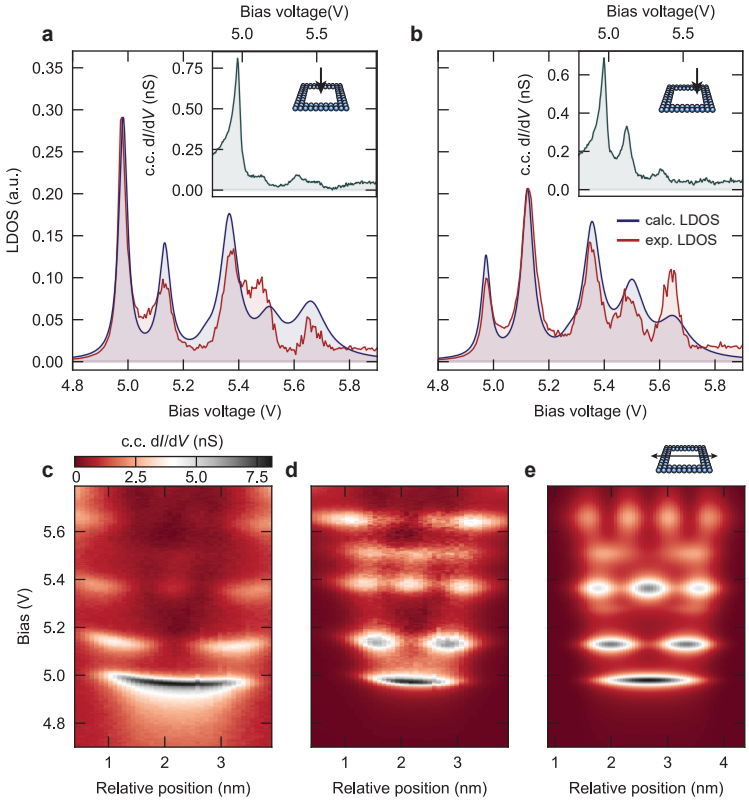

Figure 7.3: **Spatially dependent comparison of raw constant-current spectra, and the corresponding extracted and calculated local density of states**. **a, b** LDOS extracted (red) from constant-current dI/dV spectroscopy obtained at a set-point 0f 50 pA (insets), compared to the calculated LDOS (blue), obtained for the center (**a**) and edge (**b**) of the 7×7 patch (the relative position is schematically illustrated, inset). Experimental LDOS is normalized by its maximum value, and re-scaled by the maximum value of the calculated LDOS. **c** Raw, stacked constant-current differential conductance spectra obtained at a set-point of 50 pA, taken along a line crossing the center of the 7×7 patch (schematically illustrated to the right). **d** The corresponding LDOS, extracted from the experimental data using the $k_\parallel$ sensitive normalization scheme, and **e** the calculated LDOS.

rent is increasingly less sensitive to states with increasing $k_\parallel$, it follows that the relative amplitude of the higher energy peaks are increasingly underestimated if this effect is not accounted for.

As previously mentioned, the schemes proposed here rely on the absolute tip-sample distance, while only the relative tip displacement Δz is readily available and easily measured. The value of z_0, which converts the measured relative change into an absolute distance $z = \Delta z + z_0$, can be reasonably estimated by several means—such as additional $I(z)$ measurements—but is hard to pin-point precisely. As such, any normalization procedure that cannot tolerate small variations in z_0 cannot be widely implemented.

First, we note that the experimental conditions for each spectroscopic mode help us

set some limits on the value of z_0 for comparing constant-current and constant-height measurements. Constant-height measurements, for instance, require regulating at a bias voltage of interest V_{stpt} (at a current of choice) before opening the feedback for measurement. This is not the case for constant-current measurements, as the feedback is always engaged—but in either case, the tip-sample distance at V_{stpt} should be the same for both measurement modes, given measurements are performed with the same microscopic tip and at the same set-point current. Here, we chose V_{stpt} to be the highest bias voltage of interest (6.2 V, see Fig 7.2a), to ensure the tip-sample distance is set to its maximum value over the course of spectroscopy, thereby minimizing the risk of tip crashes. This means that the value of z_0, while different for each mode, should result in the same absolute distance z at the highest bias voltage, as we see in Fig 7.2b (inset). This condition allows us to compare the extracted LDOS for the two measurements, knowing that the parameter z_0 does not skew one curve relative to the other.

To more concretely trace the effects of a changing z_0, we focus on $\mathrm{d}I/\mathrm{d}V$ spectroscopy normalized for a range of z_0 values, as shown in Fig 7.2d—we can see by eye that this parameter mainly determines the overall intensity of the peaks. To quantify this, we fit the first peak in the experimental LDOS with a Lorentzian lineshape ((Fig 7.2d) to extract its width and position. Carrying out this procedure for LDOS extracted from both constant-current and -height measurements (Fig 7.2e, f), we see that in both cases the width, Γ, and position, E_0, of the peak are not significantly altered over a z_0 range of nearly 1 nm—to put this value in context, a few angstroms displacement of the tip can cause the tunneling current to change by an order of magnitude. In fact, we observe a maximum variation of $\Delta E_0 \sim 0.02\%$ in the peak position (~ 5.05 V at 0.26 nm), which, in this case, is smaller than the broadening associated with the lock-in modulation (10 mV). The change in the peak width $\Delta\Gamma$ is greater, but still negligible over such a broad range of z_0: we observe a maximum variation of $\sim 13\%$ and $\sim 10\%$ in the peak width, for constant-current and constant-height extracted LDOS, respectively. As we can see, the exact value of z_0 can impact the overall intensity of the experimentally derived LDOS, but it's the relative change Δz—which is easily measured during spectroscopy—that plays a critical role in determining the relevant peak features, such as relative intensity, width, and position.

Having ascertained that our normalization procedure is robust for different spectroscopic modes, and yields consistent results against a varying z_0, we now focus on how it fares compared to the expected (calculated) local density of states. To calculate the local density of states, we model the potential landscape of the laterally confined field-emission resonances using a finite, slanted well (see chapter 5 for more details). From this, we can calculate the expected eigenstates and energies to determine the LDOS, which is simply given by $|\Psi|^2$. To mimic the state broadening—which is primarily lifetime-limited, but also affected by experimental considerations, such as the lock-in modulation and temperature—we generate Lorentzians centered at each eigenenergy, with the linewidth set to match the experiment. More precisely, the lifetime of the resonances decreases as the principle quantum number of the in-plane mode increases [175, 179], leading to a corresponding increase in the linewidth, which is echoed in the theoretical LDOS.

Fig. 7.3 shows the experimental LDOS retrieved from constant-current $\mathrm{d}I/\mathrm{d}V$ mea-

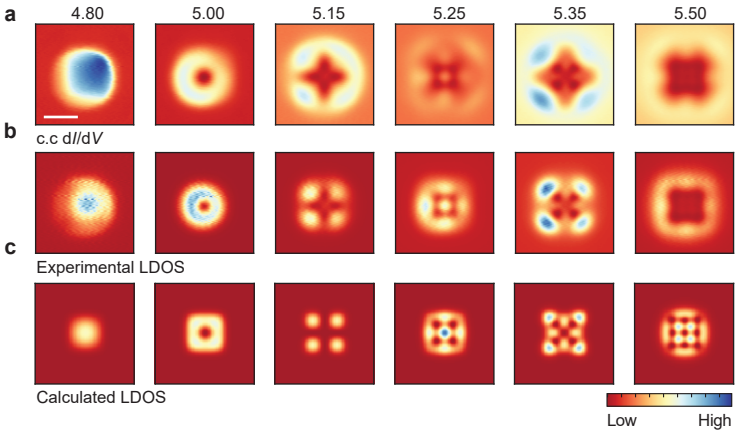

Figure 7.4: **Local density of states extracted from constant-current differential conductance maps. a** Experimental constant-current differential conductance maps, taken at a current-set point of 100 pA over the 7 × 7 patch, at the energies indicated above. Scale bar: 2 nm. **b** LDOS obtained from normalizing the differential conductance maps compared to **c** the theoretically derived LDOS.

surements performed at the center and edge of 7 × 7 patch, compared to the corresponding calculated LDOS. The agreement between the experimentally derived and expected local density of states is remarkable, especially in light of the raw dI/dV spectra. The effects of the feedback, which are most pronounced at the energy of the first resonance, are well-distinguished in the raw spectrum obtained at the patch edge (Fig. 7.3b): here, the tip displacement artificially lends the first resonance an asymmetric line-shape and heightened relative intensity, which is remedied by the normalization procedure. To probe the spatial evolution of the experimentally derived and calculated LDOS, we perform dI/dV spectroscopy along a line crossing the center of the patch (Fig. 7.3c); the raw data is normalized to obtain the LDOS (Fig. 7.3d), which we find is in fair agreement with the calculated LDOS (Fig. 7.3e). This comparison makes it clear that the tip displacement during data acquisition dramatically broadens the spatial extent of the states well beyond the confines of the patch, and changes the line-shape of the spectroscopic features, in agreement with previous findings [114, 115, 216].

Another experimental approach towards probing the full spatial evolution and extent of the local density of states is performing differential conductance maps. To do so in constant-current mode (i.e. with the feedback loop closed) complicates the matter, as the local topographic features will induce significant cross-talk between the tip-sample displacement and the measured differential conductance, convoluting data interpretation [93, 114, 220]. In Fig. 7.4, we apply our normalization procedure to constant-current maps obtained over a 7 × 7 patch, and compare it to the theoretically derived LDOS: again, we see a reduction in the spatial extent of the patch, and an increased sharpness in the spectroscopic features that allows us to better distinguish the nodal planes at each energy.

7.3. QUANTIFYING THE ELECTRONIC LIFETIMES OF UNOCCUPIED STATES

The spatial resolution provided by the scanning probe framework enables the study of surface and (Stark-shifted) image states in the limit of a completely defect-free surface, and further permits the measurement of spatially-resolved electronic lifetimes. The most common approaches towards deducing the lifetime of such states using differential conductance spectroscopy rely on the linewidth of the spectroscopic feature associated with the state [162, 163, 221, 222], or the phase-relaxation length, which is extracted from interference patterns near step edges or other scattering centers [161, 176, 223]. The latter method can only be used if the states are laterally unconfined (or approach this limit), and the former cannot be reliably used for empty states, i.e. well above the Fermi level. This limitation is due to the potential across the tunnel barrier, which varies with the applied bias voltage or tip-sample distance—which, in turn, causes the state to shift in energy during spectroscopy, artificially broadening the linewidth.

Here, we propose a method for extracting the lifetime of image states, which is based on modelling the conductance-dependent transport through the localized state. We consider two electron baths—namely, the tip and sample—coupled to this state with two corresponding decay rates, Γ_t and Γ_s. We largely simplify the potential across the tunnel junction by approximating it as a double barrier potential (Fig. 7.5a, inset), where the barrier on the sample side is an effective one meant to mimic the surface-projected electronic properties.

Transport through the double potential barrier is dictated by the voltage and height-dependent tip and sample decay rates. The transmission coefficient for resonant tunneling through a single level localized between the barriers at an energy E_n is given by the Breit-Wigner formula [224]:

$$T_{\mathrm{BW}}(E,z,V) = \frac{\Gamma_t(E,z,V)\Gamma_s(E,z,V)}{\left((\Gamma_t(E,z,V)+\Gamma_s(E,z,V))/2\right)^2 + ((E-E_n(z,V))/\hbar)^2}. \tag{7.27}$$

As previously mentioned, the energy of the level E_n is strictly a function of voltage: the state shifts higher in energy with increasing bias voltage. We can account for this change using the Bohr-Sommerfield quantization condition in the WKB approximation of a triangular potential well $\oint p(z')dz' = 2\pi\hbar(n+3/4)$, where $p(z') = \sqrt{(2m(E-V(z'))}$, and $V(z') = (\phi_t - \phi_s + eV)z'/z$, where z is the total width of the barrier (the tip-sample separation). We note that here, as above, we define our parameters relative to the sample vacuum level. By integrating the absolute value of the momentum from the start of the well ($z' = 0$) to the classical turning point z_{tp}, we find the analytical form for the discrete levels:

$$E_n(z,V) = \left(\frac{3\pi\hbar}{2}\frac{eV+\phi_t-\phi_s}{z}\left(n+\frac{3}{4}\right)\right)^{2/3}(2m)^{-1/3}. \tag{7.28}$$

Furthermore, we can relate the tip decay rate to the WKB transmission factor through the tunnel barrier (Eq. 7.8) via a proportionality constant λ:

$$\Gamma_t(z,V,E=E_n(z,V)) = \lambda\exp\left(-\frac{4\sqrt{2m_e}}{3\hbar}\frac{z}{\phi_t-\phi_s+eV}(\phi_t+eV-E_n(z,V))^{3/2}\right), \tag{7.29}$$

where, for simplicity, we consider the tip decay rate only at the energy of the bound state. By using Eq. 7.28 and focusing only on the first bound state ($n = 0$), we can determine the energy $E_0 = \left(\frac{9\pi\hbar}{8}\frac{eV+\phi_t-\phi_s}{z\sqrt{2m}}\right)^{2/3}$. The explicit form of the tip decay rate in this case is:

$$\Gamma_t(z,V,E=E_0(z,V)) = \lambda \exp\left(-\frac{4\sqrt{2m_e}}{3\hbar}\frac{z}{\phi_t-\phi_s+eV}\left(\phi_t+eV-\left(\frac{9\pi\hbar}{8}\frac{eV+\phi_t-\phi_s}{z\sqrt{2m}}\right)^{2/3}\right)^{3/2}\right). \tag{7.30}$$

To determine the current, we integrate the Breit-Wigner transmission, assuming the zero-temperature limit and positioning the chemical potentials of the sample and the tip at 0 and eV, respectively:

$$I = \frac{G_Q}{e}\int_0^{eV} T_{\mathrm{BW}}(E,z,V)\,dE \tag{7.31}$$

$$= \frac{2G_Q\hbar}{e}\frac{\Gamma_t(z,V)\Gamma_s(z,V)}{(\Gamma_t(z,V)+\Gamma_s(z,V))}\left(\tan^{-1}\left(\frac{2(eV-E_n(z,V))}{\hbar(\Gamma_t(z,V)+\Gamma_s(z,V))}\right) + \tan^{-1}\left(\frac{2E_n(z,V)}{\hbar(\Gamma_t(z,V)+\Gamma_s(z,V))}\right)\right), \tag{7.32}$$

here G_Q is the conductance quantum $e^2/(\pi\hbar)$, where the spin degeneracy has been accounted for. If the levels are resolvable, namely that $E_n \gg \Gamma_t(z,V)+\Gamma_s(z,V)$, then the expression for the current simplifies to:

$$I = \frac{2G_Q\hbar}{e}\frac{\Gamma_t(z,V)\Gamma_s(z,V)}{\Gamma_t(z,V)+\Gamma_s(z,V)}\left(\frac{\pi}{2}+\tan^{-1}\left(\frac{2(eV-E_n(z,V))}{\hbar(\Gamma_t(z,V)+\Gamma_s(z,V))}\right)\right), \tag{7.33}$$

In general, the differential conductance depends on the partial derivatives of $\Gamma_t(z,V)$, $\Gamma_s(z,V)$, and $E_n(z,V)$ with respect to voltage; for ease of notation, we will refer to these partial derivatives as $\dot{\Gamma}_t$, $\dot{\Gamma}_s$, and $\dot{E}_n$, and drop the explicit reference to their dependence on z and V. The differential conductance can be evaluated accordingly:

$$\frac{\mathrm{d}I}{\mathrm{d}V} = \frac{2G_Q\hbar}{e}\left[\left(\frac{\dot{\Gamma}_t\Gamma_s+\Gamma_t\dot{\Gamma}_s}{\Gamma_t+\Gamma_s}-\frac{\Gamma_t\Gamma_s(\dot{\Gamma}_t+\dot{\Gamma}_s)}{(\Gamma_t+\Gamma_s)^2}\right)\left(\frac{\pi}{2}+\arctan\frac{eV-E_n}{\Gamma_t+\Gamma_s}\right) + \frac{2\hbar\Gamma_t\Gamma_s}{\Gamma_t+\Gamma_s}\frac{(E_n-eV)(\dot{\Gamma}_t+\dot{\Gamma}_s)-(\Gamma_t+\Gamma_s)\dot{E}_n+e(\Gamma_s+\Gamma_t)}{\hbar^2(\Gamma_t+\Gamma_s)^2+4(E_n-eV)^2}\right]. \tag{7.34}$$

The second term in the sum in the above expression corresponds to a Lorentzian lineshape centered at E_n, with width and amplitude determined by Γ_t and Γ_s. In some cases, it sufficient to only consider the explicit derivative of the current with respect to the voltage V, rendering a simplified expression for the differential conductance (see section 7.5.1). Otherwise, we can use the analytical forms of the tip decay rate and the

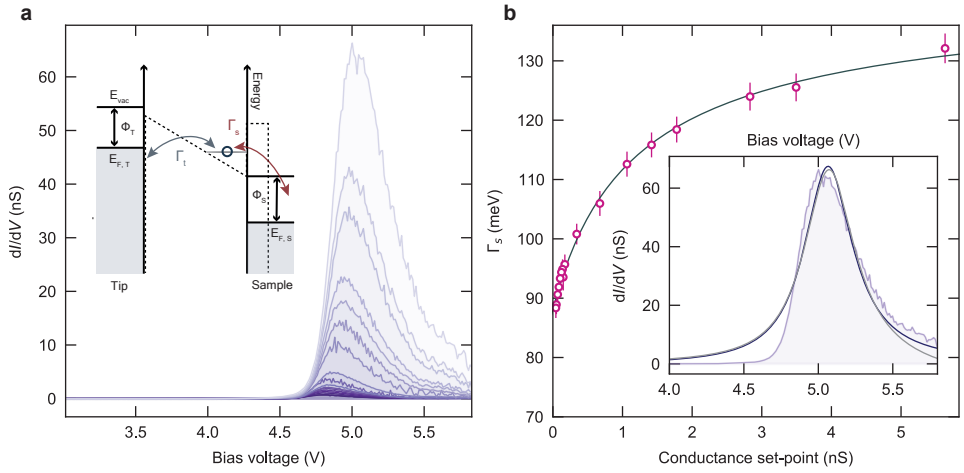

Figure 7.5: **Determining the lifetime of the first field emission resonance of Cu(100).** **a** Constant-height differential conductance measurements acquired for bare Cu(100) for a range of conductance set-points, from 0.04 nS to 5.6 nS, at 4 K. Inset: double barrier potential (dotted line) and potential across the STM junction, with the tip (Γ_t) and sample decay rates (Γ_s). **b** Inset: modelled $\mathrm{d}I/\mathrm{d}V$ derived from the simplified (Eq. 7.38, blue line) and full (Eq. 7.34, grey line) expressions for the differential conductance, compared to a constant-height measurement (purple, filled), obtained at a conductance set-point of 32 nA, 5.8 V. The sample decay rate derived from the (simplified) modelled $\mathrm{d}I/\mathrm{d}V$ as a function of conductance set-point, at 4 K (pink circles). An inverse logarithmic fit to the sample decay rate (dark grey) yields a lifetime of 8 ± 3 fs. The error bars here only account for the error associated with the fit.

changing level of the resonance to explicitly evaluate the respective derivatives:

$$\frac{\partial \Gamma_t(z,V)}{\partial V} = \frac{4\sqrt{2m_e}}{3\hbar}\frac{z(\phi_t + eV - E_n(V))^{1/2}}{\phi_t - \phi_s + eV}\left(\frac{e(\phi_t + eV - E_n(V))}{\phi_t - \phi_s + eV} - \frac{3}{2}\left(e - \frac{\partial E_n(V)}{\partial V}\right)\right)\Gamma_t(z,V), \tag{7.35}$$

and

$$\frac{\partial E_n(z,V)}{\partial V} = \frac{\pi\hbar e}{\sqrt{2mz}}\left(n+\frac{3}{4}\right)\left(\frac{3\pi\hbar}{2}\frac{eV+\phi_t-\phi_s}{z\sqrt{2m}}\left(n+\frac{3}{4}\right)\right)^{-1/3}. \tag{7.36}$$

In this framework, the time-average occupation p of the confined level is given by:

$$p = \frac{\Gamma_t(z,V)}{\Gamma_s(z,V)+\Gamma_t(z,V)}. \tag{7.37}$$

We benchmark this model by applying it to the first field-emission resonance measured on Cu(100) (Fig. 7.5), whose lifetime has been previously determined via phase-coherence length measurements [176, 225]. We perform conductance-dependent constant-height $\mathrm{d}I/\mathrm{d}V$ spectroscopy over the energy range of the first resonance (Fig. 7.5) at 4 K. By putting together equations 7.28, 7.29, and 7.34we can model the measured differential conductance using our analytical framework.

We implement the dependence of the level on the applied voltage and tip-sample distance (equation 7.28) according to $E_n = \beta_n(eV/z)^{2/3}$, where β_n is a fit parameter; for

simplicity, we assume the work functions of the tip and sample are the same. This assumption is justified on two fronts: first, the work functions of the copper crystal and tungsten tip are similar (~4.6 eV and ~4.5 eV, respectively); second, our tip preparation methods, which involve dipping the tip into the surface (meaning it is likely partially covered in copper), bring them even closer. We apply the same assumption to equation 7.29, and we take λ as a fit parameter in defining the tip decay rate. The tip-sample distance z is fixed according to the relative displacement of the z-piezo at each conductance set-points, with a universal offset parameter (to transform the relative displacement to a total tip-sample separation) that is obtained by fitting the spectrum taken at closest tip-sample distance. We have confirmed that large variations (± 1 nm) in this universal offset do not impact the extracted lifetime values. Finally, we estimate Γ_s as a constant, and we take this as a fit parameter.

With this, we use our transport model to obtain fits to each measured $\mathrm{d}I/\mathrm{d}V$ spectrum, with one such fit shown as an illustrative example in Fig. 7.5b (inset). From each fit, we extract the sample decay rate, Γ_s, as function of the conductance set-point, shown in Fig. 7.5b. An inverse logarithmic fit (see chapter 5) to the sample decay rate allows us to extract Γ_s at zero conductance set-point (i.e., when the tip is fully retracted), Γ_{s_0}, which we can relate to the lifetime via $\tau = \hbar/\Gamma_{s_0}$. This yields a lifetime of 8 ± 3 fs, in fair agreement with previously measured lifetimes obtained at 6 K [176, 225].

As such, our approach to model the transport through the localized state provides a fair estimate of the lifetime, and furthermore allows us to disentangle and quantitatively assess the tip and sample decay rates, tracing their evolution as the tip displacement is varied. The simplicity of the transport model also renders it widely applicable to the study of any type of electronic state above the Fermi level.

7.4. CONCLUSIONS

In this chapter, we presented a three-pronged approach towards quantitatively and numerically addressing field-emission resonances: we proposed a one-dimensional model for calculating the wave functions and energies of vacuum-localized states; derived a normalized procedure to extract the local density of states from constant-height and constant-current differential conductance measurements performed in the high bias regime; and finally, offered a simple transport model for estimating the electronic lifetime of these unoccupied states. We benchmark the aforementioned theoretical models with experimental results, and find good agreement in all cases.

7.5. SUPPLEMENTARY MATERIALS

7.5.1. SIMPLIFICATION OF THE DIFFERENTIAL CONDUCTANCE

The full expression of the differential conductance accounts for the voltage-dependence of Γ_t, Γ_s, and E_n (Eq. 7.34), but can be simplified further if we only consider a limited voltage-range—namely around the resonance itself. In this case, we can neglect the contributions of the terms containing $\dot{\Gamma}_t$, $\dot{\Gamma}_s$, and $\dot{E}_n$, thereby only accounting for the explicit

derivative of the current with respect to V:

$$\frac{\mathrm{d}I}{\mathrm{d}V} \approx \frac{4\hbar^2 G_Q \Gamma_t \Gamma_s}{\hbar^2(\Gamma_t+\Gamma_s)^2 + 4(E_n - eV)^2}. \tag{7.38}$$

To evaluate the robustness of this assumption, we again consider the first field-emission resonance on a bare Cu(100) surface, and model the measured differential conductance with the full and simplified expressions (see Fig. 7.5b, inset). The fit parameters of the simplified model vary minimally compared to those derived from the full expression (by $< 4\%$), and the qualitative features of both are in good agreement around the peak. Thus, we justify using Eq. 7.38 to fit a single resonance. We note here that the full expression (Eq. 7.34) must be used for fitting differential conductance spectrum spanning a broad voltage range, as the additional terms cannot be neglected beyond the limited scope of the peak itself.

8

CONCLUSION & OUTLOOK

The content of this thesis is primarily dedicated to investigating candidate building blocks for constructing artificial magnetic and electronic lattices atom-by-atom. We present nitrogen-bound Fe atoms on the Cu_2N/Cu(100) surface as viable candidates for assembling extended magnetic architectures: this spin system boasts a sizeable total magnetic moment—with a nearly unquenched orbital angular moment in the out-of-plane direction—and the largest magnetic anisotropy energy reported for Fe atoms on surfaces. A weak spin-orbit coupling allows us to probe and excite the spin and orbital angular momentum independently. Specifically, we demonstrate an orbital excitation, in which the orbital moment is fully reversed via a co-tunneling process that leaves the spin unaltered. As nitrogen-bound Fe atoms are easily manipulable, this lays the foundation for future work on larger spin lattices, in which the individual atoms can interact through both magnetic degrees of freedom.

Our preliminary work is promising in this regard: we are able to construct lattices comprised of tens of atoms reliably and quickly. This is a notable advantage, as atom manipulation is often the most time-consuming process in realizing artificial spin lattices. Furthermore, we find that nitrogen-bound Fe atoms placed two lattice sites apart are weakly exchange coupled, and that this gives rise to complicated magnetic behaviour in extended lattices, possibly due to some competition between the exchange interaction, magnetic anisotropy, and external magnetic field. We also observe an overall decrease in the energy of the orbital excitation with increasing number of nearest neighbours. Future work, which aims at quantitatively characterizing the exchange interaction between two such atoms, could clarify the precise applicability of this system for studying larger magnetic structures.

For studies of electronic artificial lattices, we present laterally confined vacuum resonances on the chlorinated Cu(100) surface. For this, we use atom manipulation to arrange single chlorine vacancies into square patches: due to the work function difference between the chlorine monolayer and bulk Cu crystal, this amounts to patterning a potential well on the surface. Accordingly, we observe particle-in-a-box modes, whose energy and spatial extent vary according to the specifications of the atomically assem-

bled patch. We find we can tune and extend the average lifetime of electrons in these engineered states by modifying the overall confining potential. Furthermore, we construct small structures comprised of these vacancy patches, such as dimers and trimers, to characterize their coupling parameters. We can exert some degree of control over the coupling strength by modifying the dimensions of the patches themselves, or that of the bridging patch connecting them. We use this platform to study a well-characterized artificial lattice: a looped dimerized chain that is expected to host domain wall states, as confirmed by our measurements. Our analysis of these results is aided in part by the methods presented in the final chapter, which detail various schemes for extracting quantitative information from high bias differential conductance spectra.

Future studies on this platform would benefit from a more detailed look at the diamond chain, particularly with a focus on verifying the nature of the end state via additional constant-height measurements. The effects of the orbital overlap may be an interesting avenue to explore as well: specifically, since the degree of orbital overlap may be tuned by the changing the bridging patch dimensions, it should be possible to closely trace how this parameter impacts the topology of the in-gap state.

Additionally, several routes can be explored to enhance the baseline coherent lifetime of the confined vacuum states in order to achieve reasonable occupation values for the study of many-body states and electron-electron correlations. One approach would be to create an inverse lattice: instead of confining the resonances to the metal patch, single vacancies can be arranged as scattering centers that trace the perimeter of the artificial atom and confine the resonances to the chlorine monolayer. We can expect this approach to enhance the lifetime of the confined states dramatically, as previous studies found that a decoupling monolayer largely suppresses the interband and intraband scattering paths to the bulk, resulting in a 3–4 times increase in the lifetime of the vacuum states [210]. Furthermore, the first vacuum state on the chlorine monolayer occurs around 3.5 V—significantly closer to the Fermi level than the first resonance observed on the Cu substrate. This should also carry significant consequences for the state lifetime, which scales with $1/(E-E_f)^2$, where E is the energy of the state and E_f is the Fermi energy [223, 225]. Suppressing the decay paths to the bulk can also be achieved by considering a different choice of substrate: perhaps one that is insulating or semiconducting, for instance.

REFERENCES

[1] L. Yan and P. Liljeroth, "Engineered electronic states in atomically precise artificial lattices and graphene nanoribbons", Advances in Physics: X **4**, 1651672 (2019).

[2] S. E. Freeney, M. R. Slot, T. S. Gardenier, I. Swart, and D. Vanmaekelbergh, "Electronic quantum materials simulated with artificial model lattices", ACS Nanoscience Au (2022).

[3] A. A. Khajetoorians, D. Wegner, A. F. Otte, and I. Swart, "Creating designer quantum states of matter atom-by-atom", Nature Reviews Physics **1**, 703–715 (2019).

[4] T. Hensgens, T. Fujita, L. Janssen, X. Li, C. Van Diepen, C. Reichl, W. Wegscheider, S. Das Sarma, and L. M. Vandersypen, "Quantum simulation of a Fermi–Hubbard model using a semiconductor quantum dot array", Nature **548**, 70–73 (2017).

[5] P. Barthelemy and L. M. Vandersypen, "Quantum dot systems: a versatile platform for quantum simulations", Annalen der Physik **525**, 808–826 (2013).

[6] C. Gross and I. Bloch, "Quantum simulations with ultracold atoms in optical lattices", Science **357**, 995–1001 (2017).

[7] A. Dauphin, M. Müller, and M. A. Martin-Delgado, "Quantum simulation of a topological Mott insulator with Rydberg atoms in a Lieb lattice", Phys. Rev. A **93**, 043611 (2016).

[8] J. Zhang, M. H. Yung, R. Laflamme, A. Aspuru-Guzik, and J. Baugh, "Digital quantum simulation of the statistical mechanics of a frustrated magnet", Nature Communications **3**, 1–10 (2012).

[9] I. Bloch, J. Dalibard, and S. Nascimbène, "Quantum simulations with ultracold quantum gases", Nature Physics **8**, 267–276 (2012).

[10] A. Singha, M. Gibertini, B. Karmakar, S. Yuan, M. Polini, G. Vignale, M. I. Katsnelson, A. Pinczuk, L. N. Pfeiffer, K. W. West, and V. Pellegrini, "Two-dimensional Mott-Hubbard electrons in an artificial honeycomb lattice", Science **332**, 1176–1179 (2011).

[11] Y. Cao, V. Fatemi, A. Demir, S. Fang, S. L. Tomarken, J. Y. Luo, J. D. Sanchez-Yamagishi, K. Watanabe, T. Taniguchi, E. Kaxiras, R. C. Ashoori, and P. Jarillo-Herrero, "Correlated insulator behaviour at half-filling in magic-angle graphene superlattices", Nature **556**, 80–84 (2018).

[12] R. Blatt and C. F. Roos, "Quantum simulations with trapped ions", Nature Physics **8**, 277–284 (2012).

[13] A. A. Houck, H. E. Türeci, and J. Koch, "On-chip quantum simulation with superconducting circuits", Nature Physics **8**, 292–299 (2012).

[14] I. Bloch, "Ultracold quantum gases in optical lattices", Nature Physics **1**, 23–30 (2005).

[15] I. Piquero-Zulaica, J. Lobo-Checa, A. Sadeghi, Z. M. A. El-Fattah, C. Mitsui, T. Okamoto, R. Pawlak, T. Meier, A. Arnau, J. E. Ortega, et al., "Precise engineering of quantum dot array coupling through their barrier widths", Nature communications **8**, 1–6 (2017).

[16] D. J. Rizzo, G. Veber, T. Cao, C. Bronner, T. Chen, F. Zhao, H. Rodriguez, S. G. Louie, M. F. Crommie, and F. R. Fischer, "Topological band engineering of graphene nanoribbons", Nature **560**, 204–208 (2018).

[17] O. Gröning, S. Wang, X. Yao, C. A. Pignedoli, G. Borin Barin, C. Daniels, A. Cupo, V. Meunier, X. Feng, A. Narita, K. Müllen, P. Ruffieux, and R. Fasel, "Engineering of robust topological quantum phases in graphene nanoribbons", Nature **560**, 209–213 (2018).

[18] F. E. Kalff, M. P. Rebergen, E. Fahrenfort, J. Girovsky, R. Toskovic, J. L. Lado, J. Fernández-Rossier, and A. F. Otte, "A kilobyte rewritable atomic memory", Nature Nanotechnology **11**, 926–929 (2016).

[19] R. Drost, T. Ojanen, A. Harju, and P. Liljeroth, "Topological states in engineered atomic lattices", Nature Physics **13**, 668–671 (2017).

[20] M. R. Slot, T. S. Gardenier, P. H. Jacobse, G. C. P. van Miert, S. N. Kempkes, S. J. M. Zevenhuizen, C. M. Smith, D. Vanmaekelbergh, and I. Swart, "Experimental realization and characterization of an electronic Lieb lattice", Nature Physics **13**, 672–676 (2017).

[21] K. K. Gomes, W. Mar, W. Ko, F. Guinea, and H. C. Manoharan, "Designer Dirac fermions and topological phases in molecular graphene", Nature **483**, 306–310 (2012).

[22] T. S. Gardenier, J. J. van den Broeke, J. R. Moes, I. Swart, C. Delerue, M. R. Slot, C. M. Smith, and D. Vanmaekelbergh, "p Orbital flat band and Dirac cone in the electronic honeycomb lattice", ACS Nano **14**, 13638–13644 (2020).

[23] S. N. Kempkes, M. R. Slot, J. J. van den Broeke, P. Capiod, W. A. Benalcazar, D. Vanmaekelbergh, D. Bercioux, I. Swart, and C. Morais Smith, "Robust zero-energy modes in an electronic higher-order topological insulator", Nature Materials **18**, 1292–1297 (2019).

[24] S. E. Freeney, J. J. van den Broeke, A. J. J. Harsveld van der Veen, I. Swart, and C. Morais Smith, "Edge-dependent topology in Kekulé lattices", Phys. Rev. Lett. **124**, 236404 (2020).

[25] M. N. Huda, S. Kezilebieke, T. Ojanen, R. Drost, and P. Liljeroth, "Tuneable topological domain wall states in engineered atomic chains", npj Quantum Materials **5**, 17 (2020).

[26] M. N. Huda, S. Kezilebieke, and P. Liljeroth, "Designer flat bands in quasi-one-dimensional atomic lattices", Phys. Rev. Research **2**, 043426 (2020).

[27] J. Girovsky, J. Lado, S. Otte, F. Kalff, E. Fahrenfort, L. Peters, and J. Fernández-Rossier, "Emergence of quasiparticle Bloch states in artificial crystals crafted atom-by-atom", SciPost Physics **2**, 020 (2017).

[28] L. C. Collins, T. G. Witte, R. Silverman, D. B. Green, and K. K. Gomes, "Imaging quasiperiodic electronic states in a synthetic penrose tiling", Nature Communications **8**, 15961 (2017).

[29] A. A. Khajetoorians, J. Wiebe, B. Chilian, S. Lounis, S. Blügel, and R. Wiesendanger, "Atom-by-atom engineering and magnetometry of tailored nanomagnets", Nature Physics **8**, 497–503 (2012).

[30] C. F. Hirjibehedin, C. P. Lutz, and A. J. Heinrich, "Spin coupling in engineered atomic structures", Science **312**, 1021–1024 (2006).

[31] A. Khajetoorians, J. Wiebe, B. Chilian, and R. Wiesendanger, "Realizing all-spin–based logic operations atom by atom", Science **332**, 1062–1064 (2011).

[32] R. Toskovic, R. Van Den Berg, A. Spinelli, I. S. Eliens, B. Van Den Toorn, B. Bryant, J. S. Caux, and A. F. Otte, "Atomic spin-chain realization of a model for quantum criticality", Nature Physics **12**, 656–660 (2016).

[33] M. F. Crommie, C. P. Lutz, and D. M. Eigler, "Confinement of electrons to quantum corrals on a metal surface", Science **262**, 218–220 (1993).

[34] H. Manoharan, C. Lutz, and D. Eigler, "Quantum mirages formed by coherent projection of electronic structure", Nature **403**, 512–515 (2000).

[35] S. Fölsch, P. Hyldgaard, R. Koch, and K. H. Ploog, "Quantum confinement in monatomic Cu chains on Cu(111)", Phys. Rev. Lett. **92**, 056803 (2004).

[36] F. E. Olsson, M. Persson, A. G. Borisov, J.-P. Gauyacq, J. Lagoute, and S. Fölsch, "Localization of the cu(111) surface state by single cu adatoms", Phys. Rev. Lett. **93**, 206803 (2004).

[37] V. D. Pham, K. Kanisawa, and S. Fölsch, "Quantum rings engineered by atom manipulation", Phys. Rev. Lett. **123**, 066801 (2019).

[38] E. Heller, M. Crommie, C. Lutz, and D. Eigler, "Scattering and absorption of surface electron waves in quantum corrals", Nature **369**, 464–466 (1994).

[39] S. Schofield, P. Studer, C. Hirjibehedin, N. Curson, G. Aeppli, and D. Bowler, "Quantum engineering at the silicon surface using dangling bonds", Nature communications **4**, 1–7 (2013).

[40] P. Echenique, R. Berndt, E. Chulkov, T. Fauster, A. Goldmann, and U. Höfer, "Decay of electronic excitations at metal surfaces", Surface Science Reports **52**, 219–317 (2004).

[41] A. Eiguren, B. Hellsing, F. Reinert, G. Nicolay, E. V. Chulkov, V. M. Silkin, S. Hüfner, and P. M. Echenique, "Role of bulk and surface phonons in the decay of metal surface states", Phys. Rev. Lett. **88**, 066805 (2002).

[42] L. Zhou, J. Wiebe, S. Lounis, E. Vedmedenko, F. Meier, S. Blügel, P. H. Dederichs, and R. Wiesendanger, "Strength and directionality of surface Ruderman–Kittel–Kasuya–Yosida interaction mapped on the atomic scale", Nature Physics **6**, 187–191 (2010).

[43] A. Spinelli, B. Bryant, F. Delgado, J. Fernández-Rossier, and A. F. Otte, "Imaging of spin waves in atomically designed nanomagnets", Nature materials **13**, 782–785 (2014).

[44] R. Elbertse, D. Coffey, J. Gobeil, and A. Otte, "Remote detection and recording of atomic-scale spin dynamics", Communications Physics **3**, 1–5 (2020).

[45] S. Loth, S. Baumann, C. P. Lutz, D. Eigler, and A. J. Heinrich, "Bistability in atomic-scale antiferromagnets", Science **335**, 196–199 (2012).

[46] S. Baumann, F. Donati, S. Stepanow, S. Rusponi, W. Paul, S. Gangopadhyay, I. G. Rau, G. E. Pacchioni, L. Gragnaniello, M. Pivetta, J. Dreiser, C. Piamonteze, C. P. Lutz, R. M. Macfarlane, B. A. Jones, P. Gambardella, A. J. Heinrich, and H. Brune, "Origin of perpendicular magnetic anisotropy and large orbital moment in Fe atoms on MgO", Physical Review Letters **115**, 237202 (2015).

[47] S. Baumann, W. Paul, T. Choi, C. P. Lutz, A. Ardavan, and A. J. Heinrich, "Electron paramagnetic resonance of individual atoms on a surface", Science **350**, 417–420 (2015).

[48] I. G. Rau, S. Baumann, S. Rusponi, F. Donati, S. Stepanow, L. Gragnaniello, J. Dreiser, C. Piamonteze, F. Nolting, S. Gangopadhyay, O. R. Albertini, R. M. Macfarlane, C. P. Lutz, B. A. Jones, P. Gambardella, A. J. Heinrich, and H. Brune, "Reaching the magnetic anisotropy limit of a 3d metal atom", Science **344**, 988–992 (2014).

[49] A. A. Khajetoorians, B. Baxevanis, C. Hübner, T. Schlenk, S. Krause, T. O. Wehling, S. Lounis, A. Lichtenstein, D. Pfannkuche, J. Wiebe, et al., "Current-driven spin dynamics of artificially constructed quantum magnets", Science **339**, 55–59 (2013).

[50] A. Spinelli, M. P. Rebergen, and A. F. Otte, "Atomically crafted spin lattices as model systems for quantum magnetism", Journal of Physics: Condensed Matter **27** (2015).

[51] M. Steinbrecher, R. Rausch, K. T. That, J. Hermenau, A. A. Khajetoorians, M. Potthoff, R. Wiesendanger, and J. Wiebe, "Non-collinear spin states in bottom-up fabricated atomic chains", Nature communications **9**, 1–9 (2018).

[52] D. J. Choi, R. Robles, S. Yan, J. A. Burgess, S. Rolf-Pissarczyk, J.-P. Gauyacq, N. Lorente, M. Ternes, and S. Loth, "Building complex Kondo impurities by manipulating entangled spin chains", Nano letters **17**, 6203–6209 (2017).

[53] A. Abragam and B. Bleaney, *Electron paramagnetic resonance of transition ions* (Oxford: Clarendon Press, 1986).

[54] J. S. Griffith, *The theory of transition-metal ions* (Cambridge University Press, 1964).

[55] D. I. Khomskii, *Transition metal compounds* (Cambridge University Press, 2014).

[56] S. Blundell, *Magnetism in condensed matter* (Oxford University Press, 2003).

[57] N. Karaman, A. Bayri, and S. Ekmekçi, "An energy competition of Co3+ and Co4+ ions during spin state transition in Ca3Co4O9 complex", in Journal of physics: conference series, Vol. 667, 1 (IOP Publishing, 2016), p. 012008.

[58] D. Dai, H. Xiang, and M.-H. Whangbo, "Effects of spin-orbit coupling on magnetic properties of discrete and extended magnetic systems", Journal of computational chemistry **29**, 2187–2209 (2008).

[59] F. Delgado and J. Fernández-Rossier, "Spin decoherence of magnetic atoms on surfaces", Progress in Surface Science **92**, 40–82 (2017).

[60] O. Eriksson, B. Johansson, R. C. Albers, A. M. Boring, and M. S. S. Brooks, "Orbital magnetism in Fe, Co, and Ni", Physical Review B **42**, 2707–2710 (1990).

[61] C. F. Hirjibehedin, C.-Y. Lin, A. F. Otte, M. Ternes, C. P. Lutz, B. A. Jones, and A. J. Heinrich, "Large magnetic anisotropy of a single atomic spin embedded in a surface molecular network", Science **317**, 1199–1203 (2007).

[62] F. Donati, S. Rusponi, S. Stepanow, C. Wäckerlin, A. Singha, L. Persichetti, R. Baltic, K. Diller, F. Patthey, E. Fernandes, J. Dreiser, Ž. Šljivančanin, K. Kummer, C. Nistor, P. Gambardella, and H. Brune, "Magnetic remanence in single atoms", Science **352**, 318–321 (2016).

[63] T. Miyamachi, T. Schuh, T. Märkl, C. Bresch, T. Balashov, A. Stöhr, C. Karlewski, S. André, M. Marthaler, M. Hoffmann, et al., "Stabilizing the magnetic moment of single holmium atoms by symmetry", Nature **503**, 242–246 (2013).

[64] S. Loth, C. P. Lutz, and A. J. Heinrich, "Spin-polarized spin excitation spectroscopy", New Journal of Physics **12**, 125021 (2010).

[65] S. Loth, K. von Bergmann, M. Ternes, A. F. Otte, C. P. Lutz, and A. J. Heinrich, "Controlling the state of quantum spins with electric currents", Nature Physics **6** (2010).

[66] A. Ferrón, F. Delgado, and J. Fernández-Rossier, "Derivation of the spin Hamiltonians for Fe in MgO", New Journal of Physics **17**, 033020 (2015).

[67] M. Etzkorn, C. Hirjibehedin, A. Lehnert, S. Ouazi, S. Rusponi, S. Stepanow, P. Gambardella, C. Tieg, P. Thakur, A. Lichtenstein, et al., "Comparing XMCD and DFT with STM spin excitation spectroscopy for Fe and Co adatoms on Cu_2N/Cu (100)", Physical Review B **92**, 184406 (2015).

[68] C. Y. Lin and B. Jones, "First-principles calculations of engineered surface spin structures", Physical Review B **83**, 014413 (2011).

[69] A. Ferrón, J. L. Lado, and J. Fernández-Rossier, "Electronic properties of transition metal atoms on Cu_2N(100)", Physical Review B **92**, 174407 (2015).

[70] H. Brune and P. Gambardella, "Magnetism of individual atoms adsorbed on surfaces", Surface Science **603**, 1812–1830 (2009).

[71] B. Bryant, A. Spinelli, J. J. T. Wagenaar, M. Gerrits, and A. F. Otte, "Local control of single atom magnetocrystalline anisotropy", Physical Review Letters **111**, 127203 (2013).

[72] A. F. Otte, M. Ternes, K. von Bergmann, S. Loth, H. Brune, C. P. Lutz, C. F. Hirjibehedin, and A. J. Heinrich, "The role of magnetic anisotropy in the Kondo effect", Nature Physics **4** (2008).

[73] S. Yan, D. J. Choi, J. A. Burgess, S. Rolf-Pissarczyk, and S. Loth, "Three-dimensional mapping of single-atom magnetic anisotropy", Nano Letters **15**, 1938–1942 (2015).

[74] T. Choi and J. A. Gupta, "Building blocks for studies of nanoscale magnetism: adsorbates on ultrathin insulating Cu_2N", Journal of Physics: Condensed Matter **26**, 394009 (2014).

[75] N. Ashcroft and D. Mermin, *Solid state physics*, 1976.

[76] P. Hofmann, *Solid state physics: an introduction* (John Wiley & Sons, 2015).

[77] M. Roy, "The tight binding method", Rutgers University (2015).

[78] J. Jenke, A. N. Ladines, T. Hammerschmidt, D. G. Pettifor, and R. Drautz, "Tight-binding bond parameters for dimers across the periodic table from density-functional theory", Physical Review Materials **5**, 023801 (2021).

[79] A. P. Sutton, M. W. Finnis, D. G. Pettifor, and Y. Ohta, "The tight-binding bond model", Journal of Physics C: Solid State Physics **21**, 35 (1988).

[80] M. Knoll and E. Ruska, "Das elektronenmikroskop", Zeitschrift für Physik **78**, 318–339 (1932).

[81] E. W. Müller, "Das feldionenmikroskop", Zeitschrift für Physik **131**, 136–142 (1951).

[82] G. Binnig, H. Rohrer, C. Gerber, and E. Weibel, "Tunneling through a controllable vacuum gap", Applied Physics Letters **40**, 178–180 (1982).

[83] G. Binnig, H. Rohrer, C. Gerber, and E. Weibel, "Surface studies by scanning tunneling microscopy", Phys. Rev. Lett. **49**, 57–61 (1982).

[84] G. Binnig, H. Rohrer, C. Gerber, and E. Weibel, "7 × 7 reconstruction on Si(111) resolved in real space", Phys. Rev. Lett. **50**, 120–123 (1983).

[85] G. Binnig, C. F. Quate, and C. Gerber, "Atomic force microscope", Phys. Rev. Lett. **56**, 930–933 (1986).

[86] G. Binnig and H. Rohrer, "Scanning tunneling microscopy—from birth to adolescence", Rev. Mod. Phys. **59**, 615–625 (1987).

[87] Y. Martin and H. K. Wickramasinghe, "Magnetic imaging by "force microscopy" with 1000 Å resolution", Applied Physics Letters **50**, 1455–1457 (1987).

[88] J. Tersoff and D. R. Hamann, "Theory of the scanning tunneling microscope", Phys. Rev. B **31**, 805–813 (1985).

[89] J. Tersoff and D. R. Hamann, "Theory and application for the scanning tunneling microscope", Phys. Rev. Lett. **50**, 1998–2001 (1983).

[90] J. Bardeen, "Tunnelling from a many-particle point of view", Phys. Rev. Lett. **6**, 57–59 (1961).

[91] N. D. Lang, "Spectroscopy of single atoms in the scanning tunneling microscope", Phys. Rev. B **34**, 5947–5950 (1986).

[92] J. G. Simmons, "Generalized formula for the electric tunnel effect between similar electrodes separated by a thin insulating film", J. Appl. Phys. **34**, 10.1063/1.1702682 (1963).

[93] J. A. Stroscio and W. J. Kaiser, *Scanning tunneling microscopy*, Vol. 27, Methods in Experimental Physics (Academic Press, 1993).

[94] H. J. W. Zandvliet and A. van Houselt, "Scanning tunneling spectroscopy.", Annual review of analytical chemistry (Palo Alto, Calif.) **2**, 37–55 (2009).

[95] R. Wiesendanger and W. Roland, *Scanning probe microscopy and spectroscopy: methods and applications* (Cambridge University press, 1994).

[96] J. A. Stroscio, R. M. Feenstra, and A. P. Fein, "Electronic structure of the Si(111)2 × 1 surface by scanning-tunneling microscopy", Phys. Rev. Lett. **57**, 2579–2582 (1986).

[97] J. A. Stroscio, R. M. Feenstra, and A. P. Fein, "Local state density and long-range screening of adsorbed oxygen atoms on the GaAs(110) surface", Phys. Rev. Lett. **58**, 1668–1671 (1987).

[98] B. C. Stipe, M. A. Rezaei, and W. Ho, "Single-molecule vibrational spectroscopy and microscopy", Science **280**, 1732–1735 (1998).

[99] M. A. Reed, "Inelastic electron tunneling spectroscopy", Materials today **11**, 46–50 (2008).

[100] D. M. Eigler and E. K. Schweizer, "Positioning single atoms with a scanning tunnelling microscope", Nature **344**, 524–526 (1990).

[101] J. A. Stroscio and D. Eigler, "Atomic and molecular manipulation with the scanning tunneling microscope", Science **254**, 1319–1326 (1991).

[102] G. Meyer, L. Bartels, S. Zöphel, E. Henze, and K. H. Rieder, "Controlled atom by atom restructuring of a metal surface with the scanning tunneling microscope", Phys. Rev. Lett. **78**, 1512–1515 (1997).

[103] M. Rashidi, J. A. Burgess, M. Taucer, R. Achal, J. L. Pitters, S. Loth, and R. A. Wolkow, "Time-resolved single dopant charge dynamics in silicon", Nature communications **7**, 1–7 (2016).

[104] A. van Houselt and H. J. W. Zandvliet, "Colloquium: time-resolved scanning tunneling microscopy", Rev. Mod. Phys. **82**, 1593–1605 (2010).

[105] S. Loth, M. Etzkorn, C. P. Lutz, D. M. Eigler, and A. J. Heinrich, "Measurement of fast electron spin relaxation times with atomic resolution", Science **329**, 1628–1630 (2010).

[106] R. de Vries, A. Saedi, D. Kockmann, A. van Houselt, B. Poelsema, and H. J. Zandvliet, "Spatial mapping of the inverse decay length using scanning tunneling microscopy", Applied physics letters **92**, 174101 (2008).

[107] C. Schönenberger, H. Van Houten, and H. Donkersloot, "Single-electron tunnelling observed at room temperature by scanning-tunnelling microscopy", Europhysics Letters **20**, 249 (1992).

[108] R. Wiesendanger, H. J. Güntherodt, G. Güntherodt, R. J. Gambino, and R. Ruf, "Observation of vacuum tunneling of spin-polarized electrons with the scanning tunneling microscope", Phys. Rev. Lett. **65**, 247–250 (1990).

[109] A. J. Heinrich, J. A. Gupta, C. P. Lutz, and D. M. Eigler, "Single-atom spin-flip spectroscopy", Science **306**, 466–469 (2004).

[110] M. Ternes, "Spin excitations and correlations in scanning tunneling spectroscopy", New Journal of Physics **17**, 063016 (2015).

[111] L. Landau and E. Lifshitz, "Chapter VII: the quasi-classical case", in *Quantum mechanics (third edition)*, edited by L. Landau and E. Lifshitz, Third Edition (Pergamon, 1977), pp. 164–196.

[112] J. F. Ge, M. Ovadia, and J. E. Hoffman, "Achieving low noise in scanning tunneling spectroscopy", Review of Scientific Instruments **90**, 101401 (2019).

[113] G. Hörmandinger, "Comment on "Direct observation of standing wave formation at surface steps using scanning tunneling spectroscopy"", Phys. Rev. Lett. **73**, 910–910 (1994).

[114] M. Ziegler, N. Néel, A. Sperl, J. Kröger, and R. Berndt, "Local density of states from constant-current tunneling spectra", Phys. Rev. B **80**, 125402 (2009).

[115]C. Hellenthal, R. Heimbuch, K. Sotthewes, E. S. Kooij, and H. J. W. Zandvliet, "Determining the local density of states in the constant current STM mode", Phys. Rev. B **88**, 035425 (2013).

[116]G. Reecht, B. W. Heinrich, H. Bulou, F. Scheurer, L. Limot, and G. Schull, "Imaging isodensity contours of molecular states with STM", New Journal of Physics **19**, 113033 (2017).

[117]P. K. Hansma, "Inelastic electron tunneling", Physics Reports **30**, 145–206 (1977).

[118]W. Ho, "Single-molecule chemistry", The Journal of chemical physics **117**, 11033–11061 (2002).

[119]R. C. Jaklevic and J. Lambe, "Molecular vibration spectra by electron tunneling", Physical Review Letters **17**, 1139 (1966).

[120]B. Stipe, M. Rezaei, and W. Ho, "Localization of inelastic tunneling and the determination of atomic-scale structure with chemical specificity", Physical Review Letters **82**, 1724 (1999).

[121]J. Fernández-Rossier, "Theory of single-spin inelastic tunneling spectroscopy", Physical review letters **102**, 256802 (2009).

[122]J. Lambe and R. Jaklevic, "Molecular vibration spectra by inelastic electron tunneling", Physical Review **165**, 821 (1968).

[123]L. Lauhon and W. Ho, "Effects of temperature and other experimental variables on single molecule vibrational spectroscopy with the scanning tunneling microscope", Review of Scientific Instruments **72**, 216–223 (2001).

[124]S. Rolf Pissarczyk, S. Yan, L. Malavolti, J. A. J. Burgess, G. McMurtrie, and S. Loth, "Dynamical negative differential resistance in antiferromagnetically coupled few-atom spin chains", Physical Review Letters **119**, 217201 (2017).

[125]D. T. Pierce, "Spin-polarized electron microscopy", Physica Scripta **38**, 291 (1988).

[126]M. Bode, "Spin-polarized scanning tunnelling microscopy", Reports on Progress in Physics **66**, 523 (2003).

[127]F. Delgado, J. J. Palacios, and J. Fernández-Rossier, "Spin-transfer torque on a single magnetic adatom", Phys. Rev. Lett. **104**, 026601 (2010).

[128]S. Yan, D.-J. Choi, J. A. Burgess, S. Rolf-Pissarczyk, and S. Loth, "Control of quantum magnets by atomic exchange bias", Nature nanotechnology **10**, 40–45 (2015).

[129]M. Kleiber, M. Bode, R. Ravli ć, and R. Wiesendanger, "Topology-induced spin frustrations at the Cr(001) surface studied by spin-polarized scanning tunneling spectroscopy", Phys. Rev. Lett. **85**, 4606–4609 (2000).

[130]M. Bode, M. Heide, K. Von Bergmann, P. Ferriani, S. Heinze, G. Bihlmayer, A. Kubetzka, O. Pietzsch, S. Blügel, and R. Wiesendanger, "Chiral magnetic order at surfaces driven by inversion asymmetry", Nature **447**, 190–193 (2007).

[131]K. von Bergmann, A. Kubetzka, O. Pietzsch, and R. Wiesendanger, "Interface-induced chiral domain walls, spin spirals and skyrmions revealed by spin-polarized scanning tunneling microscopy", Journal of Physics: Condensed Matter **26**, 394002 (2014).

[132] R. Wiesendanger, "Spin mapping at the nanoscale and atomic scale", Reviews of Modern Physics **81**, 1495 (2009).

[133] A. Spinelli, "Quantum magnetism through atomic assembly", PhD thesis (Delft University of Technology, 2015).

[134] W. Ko, C. Ma, G. D. Nguyen, M. Kolmer, and A. P. Li, "Atomic-scale manipulation and in situ characterization with scanning tunneling microscopy", Advanced Functional Materials **29**, 1903770 (2019).

[135] S. W. Hla, "Atom-by-atom assembly", Reports on Progress in Physics **77**, 056502 (2014).

[136] S. Gauthier, "Atomic and molecular manipulations of individual adsorbates by STM", Applied Surface Science **164**, 84–90 (2000).

[137] M. Ternes, C. P. Lutz, C. F. Hirjibehedin, F. J. Giessibl, and A. J. Heinrich, "The force needed to move an atom on a surface", Science **319**, 1066–1069 (2008).

[138] J. A. Stroscio and R. J. Celotta, "Controlling the dynamics of a single atom in lateral atom manipulation", Science **306**, 242–247 (2004).

[139] I. Swart, T. Sonnleitner, J. Niedenfuhr, and J. Repp, "Controlled lateral manipulation of molecules on insulating films by STM", Nano letters **12**, 1070–1074 (2012).

[140] A. Kühnle, G. Meyer, S. W. Hla, and K. H. Rieder, "Understanding atom movement during lateral manipulation with the stm tip using a simple simulation method", Surface science **499**, 15–23 (2002).

[141] R. Rejali, D. Coffey, J. Gobeil, J. W. González, F. Delgado, and A. F. Otte, "Complete reversal of the atomic unquenched orbital moment by a single electron", npj Quantum Materials **5**, 60 (2020).

[142] F. D. Natterer, K. Yang, W. Paul, P. Willke, T. Choi, T. Greber, A. J. Heinrich, and C. P. Lutz, "Reading and writing single-atom magnets", Nature **543**, 226–228 (2017).

[143] J. Gobeil, D. Coffey, S.-J. Wang, and A. F. Otte, "Large insulating nitride islands on Cu_3Au as a template for atomic spin structures", Surface Science **679**, 202–206 (2019).

[144] P. Błoński, A. Lehnert, S. Dennler, S. Rusponi, M. Etzkorn, G. Moulas, P. Bencok, P. Gambardella, H. Brune, and J. Hafner, "Magnetocrystalline anisotropy energy of Co and Fe adatoms on the (111) surfaces of Pd and Rh", Physical Review B **81**, 104426 (2010).

[145] L. Peters, I. Di Marco, O. Grånäs, E. Şaşıoğlu, A. Altun, S. Rossen, C. Friedrich, S. Blügel, M. I. Katsnelson, A. Kirilyuk, and O. Eriksson, "Correlation effects and orbital magnetism of Co clusters", Physical Review B **93**, 224428 (2016).

[146] J. L. Lado, A. Ferrón, and J. Fernández-Rossier, "Exchange mechanism for electron paramagnetic resonance of individual adatoms", Physical Review B **96**, 205420 (2017).

[147] F. Donati, Q. Dubout, G. Autès, F. Patthey, F. Calleja, P. Gambardella, O. V. Yazyev, and H. Brune, "Magnetic moment and anisotropy of individual Co atoms on graphene", Physical Review Letters **111**, 236801 (2013).

[148] B. Bryant, R. Toskovic, A. Ferron, J. L. Lado, A. Spinelli, J. Fernandez-Rossier, and A. F. Otte, "Controlled complete suppression of single-atom inelastic spin and orbital cotunneling", Nano Letters **15**, 6542–6546 (2015).

[149]B. Kiraly, A. N. Rudenko, W. M. van Weerdenburg, D. Wegner, M. I. Katsnelson, and A. A. Khajetoorians, "An orbitally derived single-atom magnetic memory", Nature communications **9**, 3904 (2018).

[150]M. Ternes, "Probing magnetic excitations and correlations in single and coupled spin systems with scanning tunneling spectroscopy", Progress in Surface Science **92**, 83–115 (2017).

[151]F. Delgado and J. Fernández-Rossier, "Cotunneling theory of atomic spin inelastic electron tunneling spectroscopy", Physical Review B **84**, 045439 (2011).

[152]J. Reina Gálvez, C. Wolf, F. Delgado, and N. Lorente, "Cotunneling mechanism for all-electrical electron spin resonance of single adsorbed atoms", Physical Review B **100**, 035411 (2019).

[153]E. M. Chudnovsky and D. A. Garanin, "Rotational states of a nanomagnet", Physical Review B **81**, 214423 (2010).

[154]N. Bloembergen, S. Shapiro, P. S. Pershan, and J. O. Artman, "Cross-relaxation in spin systems", Physical Review **114**, 445–459 (1959).

[155]B. Chilian, A. A. Khajetoorians, S. Lounis, A. T. Costa, D. L. Mills, J. Wiebe, and R. Wiesendanger, "Anomalously large *g* factor of single atoms adsorbed on a metal substrate", Physical Review B **84**, 212401 (2011).

[156]M. Grundmann, *The physics of semiconductors* (Springer-Verlag, 2006).

[157]S. Yan, D. J. Choi, J. A. J. Burgess, S. Rolf-Pissarczyk, and S. Loth, "Control of quantum magnets by atomic exchange bias", Nature Nanotechnology **10** (2014).

[158]V. V. Mazurenko, S. N. Iskakov, A. N. Rudenko, I. V. Kashin, O. M. Sotnikov, M. V. Valentyuk, and A. I. Lichtenstein, "Correlation effects in insulating surface nanostructures", Physical Review B **88**, 085112 (2013).

[159]R. Rejali, L. Farinacci, D. Coffey, R. Broekhoven, J. Gobeil, Y. M. Blanter, and S. Otte, "Confined vacuum resonances as artificial atoms with tunable lifetime", ACS Nano **16**, 11251–11258 (2022).

[160]S. N. Kempkes, M. R. Slot, S. E. Freeney, S. J. M. Zevenhuizen, D. Vanmaekelbergh, I. Swart, and C. M. Smith, "Design and characterization of electrons in a fractal geometry", Nature Physics **15**, 127–131 (2019).

[161]K. F. Braun and K. H. Rieder, "Engineering electronic lifetimes in artificial atomic structures", Phys. Rev. Lett. **88**, 096801 (2002).

[162]H. Jensen, J. Kröger, R. Berndt, and S. Crampin, "Electron dynamics in vacancy islands: scanning tunneling spectroscopy on Ag(111)", Phys. Rev. B **71**, 155417 (2005).

[163]J. Kliewer, R. Berndt, and S. Crampin, "Scanning tunnelling spectroscopy of electron resonators", New Journal of Physics **3**, 22–22 (2001).

[164]M. R. Slot, S. N. Kempkes, E. J. Knol, W. M. J. van Weerdenburg, J. J. van den Broeke, D. Wegner, D. Vanmaekelbergh, A. A. Khajetoorians, C. Morais Smith, and I. Swart, "*p*-band engineering in artificial electronic lattices", Phys. Rev. X **9**, 011009 (2019).

[165]S. Freeney, S. Borman, J. Harteveld, and I. Swart, "Coupling quantum corrals to form artificial molecules", SciPost Phys. **9**, 85 (2020).

[166] J. P. Sun, G. Haddad, P. Mazumder, and J. Schulman, "Resonant tunneling diodes: models and properties", Proceedings of the IEEE **86**, 641–660 (1998).

[167] P. O. Gartland, S. Berge, and B. J. Slagsvold, "Photoelectric work function of a copper single crystal for the (100), (110), (111), and (112) faces", Phys. Rev. Lett. **28**, 738–739 (1972).

[168] D. Westphal and A. Goldmann, "Chlorine adsorption on copper: II. photoemission from Cu(001)c(2 × 2)-Cl and Cu(111)($\sqrt{3} \times \sqrt{3}$)R30°-Cl", Surface Science **131**, 113–138 (1983).

[169] P. Ruffieux, K. Ait-Mansour, A. Bendounan, R. Fasel, L. Patthey, P. Gröning, and O. Gröning, "Mapping the electronic surface potential of nanostructures surfaces", Phys. Rev. Lett. **102**, 086807 (2009).

[170] T. Jung, Y. W. Mo, and F. J. Himpsel, "Identification of metals in scanning tunneling microscopy via image states", Phys. Rev. Lett. **74**, 1641–1644 (1995).

[171] M. Pivetta, F. ç. Patthey, M. Stengel, A. Baldereschi, and W.-D. Schneider, "Local work function Moiré pattern on ultrathin ionic films: NaCl on Ag(100)", Phys. Rev. B **72**, 115404 (2005).

[172] H. C. Ploigt, C. Brun, M. Pivetta, F. ç. Patthey, and W. D. Schneider, "Local work function changes determined by field emission resonances: NaCl/Ag(100)", Phys. Rev. B **76**, 195404 (2007).

[173] W. Berthold, U. Höfer, P. Feulner, E. V. Chulkov, V. M. Silkin, and P. M. Echenique, "Momentum-resolved lifetimes of image-potential states on Cu(100)", Phys. Rev. Lett. **88**, 056805 (2002).

[174] P. Echenique, J. Pitarke, E. Chulkov, and A. Rubio, "Theory of inelastic lifetimes of low-energy electrons in metals", Chemical Physics **251**, 1–35 (2000).

[175] S. Crampin, "Lifetimes of Stark-shifted image states", Phys. Rev. Lett. **95**, 046801 (2005).

[176] P. Wahl, M. A. Schneider, L. Diekhöner, R. Vogelgesang, and K. Kern, "Quantum coherence of image-potential states", Phys. Rev. Lett. **91**, 106802 (2003).

[177] G. A. Burdick, "Energy band structure of copper", Phys. Rev. **129**, 138–150 (1963).

[178] J. I. Pascual, C. Corriol, G. Ceballos, I. Aldazabal, H.-P. Rust, K. Horn, J. M. Pitarke, P. M. Echenique, and A. Arnau, "Role of the electric field in surface electron dynamics above the vacuum level", Phys. Rev. B **75**, 165326 (2007).

[179] S. Stepanow, A. Mugarza, G. Ceballos, P. Gambardella, I. Aldazabal, A. G. Borisov, and A. Arnau, "Localization, splitting, and mixing of field emission resonances induced by alkali metal clusters on Cu(100)", Phys. Rev. B **83**, 115101 (2011).

[180] P. Giannozzi, O. Andreussi, T. Brumme, O. Bunau, M. B. Nardelli, M. Calandra, R. Car, C. Cavazzoni, D. Ceresoli, M. Cococcioni, N. Colonna, I. Carnimeo, A. D. Corso, S. de Gironcoli, P. Delugas, R. A. D. Jr, A. Ferretti, A. Floris, G. Fratesi, G. Fugallo, R. Gebauer, U. Gerstmann, F. Giustino, T. Gorni, J. Jia, M. Kawamura, H.-Y. Ko, A. Kokalj, E. Küçükbenli, M. Lazzeri, M. Marsili, N. Marzari, F. Mauri, N. L. Nguyen, H.-V. Nguyen, A. Otero-de-la-Roza, L. Paulatto, S. Poncé, D. Rocca, R. Sabatini, B. Santra, M. Schlipf, A. P. Seitsonen, A. Smogunov, I. Timrov, T. Thonhauser, P. Umari, N. Vast, X. Wu, and S. Baroni, "Advanced capabilities for materials modelling with quantum espresso", Journal of Physics: Condensed Matter **29**, 465901 (2017).

[181] M. Kawamura, "Fermisurfer: Fermi-surface viewer providing multiple representation schemes", Computer Physics Communications **239**, 197–203 (2019).

[182] C. W. Groth, M. Wimmer, A. R. Akhmerov, and X. Waintal, "Kwant: a software package for quantum transport", New Journal of Physics **16**, 063065 (2014).

[183] Y. Leschber and J. P. Draayer, "Orthogonal polynomial expansion for the Löwdin transformation", Journal of Physics A: Mathematical and General **22**, 2675–2685 (1989).

[184] J. G. Aiken, H. B. Jonassen, and H. S. Aldrich, "Löwdin orthogonalization as a minimum energy perturbation", The Journal of Chemical Physics **62**, 2745–2746 (1975).

[185] W. P. Su, J. R. Schrieffer, and A. J. Heeger, "Solitons in polyacetylene", Phys. Rev. Lett. **42**, 1698–1701 (1979).

[186] J. K. Asbóth, L. Oroszlány, and A. Pályi, "The Su-Schrieffer-Heeger (SSH) model", in *A short course on topological insulators: band structure and edge states in one and two dimensions* (Springer International Publishing, Cham, 2016), pp. 1–22.

[187] R. E. Peierls, *Quantum theory of solids* (Oxford University Press., 2001).

[188] A. J. Heeger, S. Kivelson, J. R. Schrieffer, and W. P. Su, "Solitons in conducting polymers", Reviews of Modern Physics **60**, 781 (1988).

[189] S. Cheon, T. H. Kim, S. H. Lee, and H. W. Yeom, "Chiral solitons in a coupled double peierls chain", Science **350**, 182–185 (2015).

[190] S. N. Kempkes, P. Capiod, S. Ismaili, J. Mulkens, I. Swart, and C. M. Smith, "Compact localized boundary states in a quasi-1D electronic diamond-necklace chain", arXiv preprint, arXiv:2201.02012 (2022).

[191] G. Pelegrı, A. M. Marques, R. G. Dias, A. J. Daley, V. Ahufinger, and J. Mompart, "Topological edge states with ultracold atoms carrying orbital angular momentum in a diamond chain", Phys. Rev. A **99**, 023612 (2019).

[192] D. Sunko, "Angular momentum in two dimensions", European journal of physics **31**, L59 (2010).

[193] N. Wheeler, *Classical/ quantum theory of hydrogen*, 1999.

[194] J. Polo, J. Mompart, and V. Ahufinger, "Geometrically induced complex tunnelings for ultracold atoms carrying orbital angular momentum", Phys. Rev. A **93**, 10.1103/PhysRevA.93.033613 (2016).

[195] A. M. Marques, L. Madail, and R. G. Dias, "One-dimensional 2^n-root topological insulators and superconductors", Phys. Rev. B **103**, 235425 (2021).

[196] A. A. Lopes and R. G. Dias, "Interacting spinless fermions in a diamond chain", Phys. Rev. B **84**, 085124 (2011).

[197] S. M. Barnett and D. T. Pegg, "Quantum theory of rotation angles", Phys. Rev. A **41**, 3427–3435 (1990).

[198] P. E. Wormer, *Angular momentum theory*, Institute of Theoretical Chemistry, Radboud University Nijmegen, 2006.

[199] J. A. Kubby, Y. R. Wang, and W. J. Greene, "Electron interferometry at a heterojunction interface", Phys. Rev. Lett. **65**, 2165–2168 (1990).

[200] K. Bobrov, A. J. Mayne, and G. Dujardin, "Atomic-scale imaging of insulating diamond through resonant electron injection", Nature **413**, 616–619 (2001).

[201] A. Schlenhoff, S. Kovarik, S. Krause, and R. Wiesendanger, "Real-space imaging of atomic-scale spin textures at nanometer distances", Applied Physics Letters **116**, 122406 (2020).

[202] W. Krenner, D. Kühne, F. Klappenberger, and J. V. Barth, "Assessment of scanning tunneling spectroscopy modes inspecting electron confinement in surface-confined supramolecular networks", Scientific Reports **3**, 1454 (2013).

[203] S. Kevan and W. Eberhardt, "Surface states on metals", in *Angle-resolved photoemission*, Vol. 74, edited by S. Kevan, Studies in Surface Science and Catalysis (Elsevier, 1992), pp. 99–143.

[204] P. Echenique, J. Pitarke, E. Chulkov, and V. Silkin, "Image-potential-induced states at metal surfaces", Journal of Electron Spectroscopy and Related Phenomena **126**, 163–175 (2002).

[205] E. Chulkov, V. Silkin, and P. Echenique, "Image potential states on metal surfaces: binding energies and wave functions", Surface Science **437**, 330–352 (1999).

[206] I. Tamm, "Über eine mögliche art der elektronenbindung an kristalloberflächen", Zeitschrift für Physik **76**, 849–850 (1932).

[207] W. Shockley, "On the surface states associated with a periodic potential", Phys. Rev. **56**, 317–323 (1939).

[208] L. Limot, T. Maroutian, P. Johansson, and R. Berndt, "Surface-state Stark shift in a scanning tunneling microscope", Phys. Rev. Lett. **91**, 196801 (2003).

[209] A. Goldmann, V. Dose, and G. Borstel, "Empty electronic states at the (100), (110), and (111) surfaces of nickel, copper, and silver", Phys. Rev. B **32**, 1971–1980 (1985).

[210] K. Schubert, A. Damm, S. V. Eremeev, M. Marks, M. Shibuta, W. Berthold, J. Güdde, A. G. Borisov, S. S. Tsirkin, E. V. Chulkov, and U. Höfer, "Momentum-resolved electron dynamics of image-potential states on Cu and Ag surfaces", Phys. Rev. B **85**, 205431 (2012).

[211] K. Giesen, F. Hage, F. J. Himpsel, H. J. Riess, and W. Steinmann, "Two-photon photoemission via image-potential states", Phys. Rev. Lett. **55**, 300–303 (1985).

[212] R. W. Schoenlein, J. G. Fujimoto, G. L. Eesley, and T. W. Capehart, "Femtosecond studies of image-potential dynamics in metals", Phys. Rev. Lett. **61**, 2596–2599 (1988).

[213]V. A. Ukraintsev, "Data evaluation technique for electron-tunneling spectroscopy", Phys. Rev. B **53**, 11176–11185 (1996).

[214]B. Koslowski, C. Dietrich, A. Tschetschetkin, and P. Ziemann, "Evaluation of scanning tunneling spectroscopy data: approaching a quantitative determination of the electronic density of states", Phys. Rev. B **75**, 035421 (2007).

[215]M. Passoni, F. Donati, A. Li Bassi, C. S. Casari, and C. E. Bottani, "Recovery of local density of states using scanning tunneling spectroscopy", Phys. Rev. B **79**, 045404 (2009).

[216]A. Pronschinske, D. J. Mardit, and D. B. Dougherty, "Modeling the constant-current distance-voltage mode of scanning tunneling spectroscopy", Phys. Rev. B **84**, 205427 (2011).

[217]T. Feuchtwang, P. Cutler, and N. Miskovsky, "A theory of vacuum tunneling microscopy", Physics Letters A **99**, 167–171 (1983).

[218]R. H. Fowler and L. Nordheim, "Electron emission in intense electric fields", Proceedings of the Royal Society A **119**, 173–181 (1928).

[219]N. Krane, C. Lotze, and K. J. Franke, "Moiré structure of MoS_2 on Au(111): local structural and electronic properties", Surface Science **678**, 136–142 (2018).

[220]T. Berghaus, A. Brodde, H. Neddermeyer, and S. Tosch, "Scanning tunneling microscopy and spectroscopy on 7 × 7 reconstructed Si(111) surfaces containing defects", Surface Science **193**, 235–258 (1988).

[221]J. Li, W. D. Schneider, R. Berndt, O. R. Bryant, and S. Crampin, "Surface-state lifetime measured by scanning tunneling spectroscopy", Phys. Rev. Lett. **81**, 4464–4467 (1998).

[222]L. Vitali, P. Wahl, M. Schneider, K. Kern, V. Silkin, E. Chulkov, and P. Echenique, "Inter- and intraband inelastic scattering of hot surface state electrons at the Ag(111) surface", Surface Science **523**, L47–L52 (2003).

[223]L. Bürgi, O. Jeandupeux, H. Brune, and K. Kern, "Probing hot-electron dynamics at surfaces with a cold scanning tunneling microscope", Phys. Rev. Lett. **82**, 4516–4519 (1999).

[224]Y. V. Nazarov and Y. M. Blanter, *Quantum transport: introduction to nanoscience* (Cambridge University Press, 2009).

[225]S. Crampin, J. Kröger, H. Jensen, and R. Berndt, "Phase coherence length and quantum interference patterns at step edges", Phys. Rev. Lett. **95**, 029701 (2005).

CURRICULUM VITÆ

Rasa REJALI

27-07-1994 Born in Esfahan, Iran.

EDUCATION

2008–2012 Secondary School
York Mills Collegiate Institute
Toronto, Canada

2012–2016 Undergraduate in Physics & English Literature (3.9/4 CGPA)
McGill University, Quebec, Canada
Robert E. Bell Prize

2016–2018 M.Sc. in Physics (*summa cum laude*)
McGill University, Quebec, Canada
Thesis: Ultrafast atomic force microscopy
Promotor: Prof. dr. P. Grütter
Alexander McFee & NSERC Fellow

2018-2022 Ph.D. in Physics
Delft University of Technology, Delft, Netherlands
Thesis: Building blocks for atomically assembled magnetic and electronic artificial lattices
Promotor: Prof. dr. A. F. Otte

LIST OF PUBLICATIONS

6. **R. Rejali**, L. Farinacci, D. Coffey, R. Broekhoven, J. Gobeil, Y. M. Blanter, A. F. Otte, *Confined vacuum resonances as artificial atoms with tunable lifetime*, ACS Nano **16**, 11251–11258 (2022).

5. **R. Rejali**, L. Farinacci, A. F. Otte, *Normalization procedure for obtaining the local density of states from high-bias scanning tunneling spectroscopy*, arXiv: 2204.09929, (2022).

4. L. M. Veldman, L. Farinacci, **R. Rejali**, R. Broekhoven, J. Gobeil, D. Coffey, M. Ternes, A. F. Otte, *Free coherent evolution of a coupled atomic spin system initialized by electron scattering*, Science **372**, 6545 (2021)

3. Z. Schumacher, **R. Rejali**, M. Cowie, A. Spielhofer, Y. Miyahara, P. Grütter, *Charge Carrier Inversion in a Doped Thin Film Organic Semiconductor Island*, ACS Nano **15**, 6 (2021).

2. Z. Schumacher, **R. Rejali**, R. Pachlatko, A. Spielhofer, P. Nagler, Y. Miyahara, D. G. Cooke, P. Grütter, *Nanoscale force sensing of an ultrafast nonlinear optical response*, PNAS **117**, 33 (2020).

1. **R. Rejali**, D. Coffey, J. Gobeil, J. W. González, F. Delgado, A. F. Otte, *Complete reversal of the atomic unquenched orbital moment by a single electron*, npj Quantum Materials **5**, 60 (2020).

ACKNOWLEDGEMENTS

For what do we live, but to make sport
for our neighbours and laugh at them in our turn?

Jane Austen

My time in Delft has been shaped by the kind faces littering the halls, that have over the course of the past four years transformed from the countenance of strangers to dear friends. While a few pages is not sufficient thanks for the support and patience I have received over the years, I hope to at least communicate the gratitude it's imbued me with.

The most natural place to begin is with my supervisor, **Sander**, without whom there wouldn't be a thesis to speak of. Thank you for the unbelievable opportunity to play with atoms every day: I have really enjoyed the challenge, and am grateful for all the new experiences and hard-learned lessons that have colored my time here. **Toeno**, thank you for being my co-promoter and patiently sitting through our yearly progress meetings with a genuine interest in my scientific and personal well-being.

Sometimes we find guidance in unexpected places, and for this I have to thank **Sonia**: your infectious enthusiasm, optimism, and no-nonsense attitude have given me direction and motivation when I needed it most—thank you for your encouragement. **Anton**, the department would not be nearly as nice without your keen scientific eye and year-round cargo shorts. I admire your tenacity in standing up for what you believe in, and am grateful for the positive change you have brought about. **Yaroslav**, the last year has been increasingly filled with insightful and fun chats with you—your door is always open for questions, and I am thankful for the experience of working with you. I would also like to extend my sincere gratitude to the members of my doctoral committee not yet mentioned: **Ingmar Swart**, **Harold Zandvliet**, and **Herre van der Zant**.

David, you are the Platonic ideal of a true friend, and yes, you should imagine me saying that in my impeccable posh British accent. I have been able to count on you from the very first day I met you—and this trust and reassurance has only grown over the years. Thank you for the unending patience, support, and frankness that marks our friendship: I am deeply grateful for it. I wouldn't have been able to finish this degree without you, and I wouldn't have had nearly as much fun doing it—thanks for the countless times you made me laugh so hard I nearly hurt myself.

There was a blissfully calm period of six months in which I got to spend every day in the lab with some of my closest friends (who fortuitously happen to be brilliant scientists): **Laëti** and **Lukas**, you've felt like my partners in crime the past years, and I could not be more pleased about this turn of events.

Laëti—our self-proclaimed 'Post-doc #1' and reigning title holder—you have spent countless hours helping me make sense of physics, data, and life. I will miss making you laugh as you're drinking coffee, and taking great pride as it eventually shoots out of your nose (let it out, Laëti!); I will miss your *sneaky* shenanigans and the transparency with which you interact with everyone; and most of all, I will miss the conviction with which you fight for what you think is right. Thank you for your friendship, and for all your help with my thesis and the great experience we had writing papers together.

The artist formerly known as **(S)Lukas**, I am grateful to have found a friend in you, and to have spent the entirety of my time in Delft alongside such a wonderful person. A quick scroll through my phone will reveal countless photos of us—nearly all of them compromising in some capacity—having the time of our lives. Dancing in the lab to Sigrid, sitting on the STM, drinking shamefully colourful cocktails, truly weak attempts at twerking, and making giant chocolate cookies in lewd shapes. I am so appreciative of these memories, and look forward to making many more. Most of all, I am thankful you dance like a 70's icon and dress like a respectable professor—I can't think of something that recommends you more, except perhaps your coveted membership in the Amsterdam art scene.

To my reminder of home away from home: **Jérémie**, you've been a true friend. From celebrating Canadian thanksgiving, to making sugar pies, to having our daily tea breaks—thank you for the many fond memories. **Alex**, your optimism and friendliness lightens our lunch breaks, especially on the more challenging days. I leave you with some of the wisest words ever uttered: you better *werq*. **Hester**, you've been an excellent addition to the group from the first day you started, and I wish you nothing but smooth sailing for the here on out. **Evert**, your frankness is a breath of fresh air, and I wish you good luck with the remainder of your PhD. Sweet **Rik**(kerz), your cheery smile and open attitude are indispensable to our weekly group meetings. **Robbie**, thanks for being a welcoming presence when I first started, and helping me get accustomed to Dutch humour with your (desperately needed) 'sarcasm' sign.

During my third year I was tasked with supervising a master's student—a seemingly bleak endeavour I didn't much look forward to. To my surprise, the experience was one of the most fruitful and fulfilling during my postgraduate studies. This was largely due to you, **Maura**: you're an earnest, kind, hard-working person, and supervising you was nothing short of a joy. For the unaware amongst us, Maura is in fact an internet celebrity and was promoted to such elite ranks after she made the world's smallest Christmas tree by manipulating single atoms—something she did late into the night while listening to the greatest Christmas album ever made (thank you, Michael Bublé) as a surprise for me. Thanks for being an excellent human being to everyone who has the honor of being in your life (and in case you're wondering, yes, you should be crying by now).

A constant throughout my PhD has been my amazing office mates: **Irina** and **Sabrya**, you have been incredibly supportive friends and colleagues. You encouraged me as I spent weeks and weeks writing, fed me with homemade baked goods, and offered your time and listening ear whenever it was getting to be too much. Not to mention, you have served as my Offical Dutch Guide, patiently offering translations and useful advice as I've navigated the different aspects of Dutch society. Most importantly, I have heard from several different (unbiased) sources that our office always smells amazing—an ac-

complishment in the physics faculty indeed.

To my fellow quantum mechanics teaching assistants: **Mark**, **Jorrit**, and **Marios**, our in-person homework sessions filled with jokes, crappuccinos, and occasionally senseless questions still bring a smile to my face. Thanks for teaching me that grading exams is a task best performed with a pile of donuts at hand. **JorJor**, aka the boy genius, your steadiness and gentle kindness have improved my day on many occasions. **Marios**—the man, the myth, the legend—despite your taste in music, I am glad to call you a friend.

In recent years, the Caviglia lab has become an indispensable part of my daily lunch breaks. **Jorrit**, I thoroughly enjoyed the opportunity this afforded me to mock your lunch choices. **Ulderico** and **Thierry**, aside from our many fun and engaging conversations, you imparted an invaluable lesson to not only me, but anyone brave enough to live by your example: you live by the apple, you die by the apple. **Thierry**, thank you for your generosity and a never ending thirst for Friday night beers. **Ulderico**, I really enjoy your characteristic easy cool, especially when it's paired with your uproarious laughter—but let's be honest, I was only in this for the burgers and espressos. **Patrick**, you were a happy addition to our Dispatch TA sessions, and have been a great colleague, lunch companion, and friend these past years.

Allard, your enthusiasm is contagious and I've always had a great time hearing about your climbing adventures. **Brecht**osaurus Rex, I usually find myself in a pile of laughter around you—whether we are roommates at a conference, bumping into each other in the hall, or viciously playing paintball. **Joris**, your easy going attitude and bright smile have always made my days better. **Michael**, my male nympho and playa playa supreme: I will miss being able to creepily stare at you from across the hall, but most of all, I will miss the times you'd pop into my office for a quick chat. Aside from filling me in on your most recent escapades, you'd always check in on how I was doing—and that's been very much appreciated. **Samer**, talking to you makes me feel like I'm home again, and I'm inconsolable that I won't be able to badger you with my jokes or test your Toronto slang vocabulary on a daily basis anymore. I hope to see you around the yoga studio to salvage at least some of my undeniably *fire* material.

The first few months of my PhD were bleak and lonely: I was far away from home, and I didn't have much of a social network in the Netherlands—that is, until I met **Iacopo**. From that fateful Friday night four years ago, you have been my dear and cherished friend. You single-handedly made me feel welcome and included, and I don't want to imagine how this experience would have panned out without you. Your kindness and generosity have marked so many of my experiences here: Easter at your adorable house with the lovely **Ana**, Friday night drinks and dinner, Covid brunch dates and shopping sprees, skiing in the French alps, dancing the night away, and so much more. I would say I'll miss you, but I know I won't—prepare to hang out, buddy!

To the h-bar group, thank you for adopting me. **Hélène**, you're a treasure: a one-woman rug-weaving, cheese-making, masterpiece-painting wonder. Voted Funniest Friend Alive the last two years running, I'm not sure there's anything you can't do. Collaborating with you was a highlight of my PhD, and I will miss you and your physics insight sorely (but not really, since you're under contractual obligation to keep hanging out with me). **Christian**, you're the Canadian ideal embodied, and I mean that in the most positive way possible—polite, kind to no end, inclusive, and incredibly considerate. Keep

fermenting and pickling, brother! **Marta**, you have all the makings of an incredible scientist without any of the ego, and on top of that, you're a thoughtful and caring friend—I only wish you'd stop eating cheese as a main meal.

Luigi, your memes, support, and office chats have been very much appreciated. You're a staple of the department, and Manchester is lucky to have you! **Thomas**, going to Utrecht was a necessary change of pace, and working with an optimistic, capable, and Foosball savvy person such as yourself was the icing on the cake. To all the aforementioned folks, as well as **Parsa**, **Nicco**, **Nina**, **Sonakshi**, **Abel**, **Holger**, **Gary**, **Yildiz**, **Ranko**, **Nikos** and all the countless others that make QN a social, positive place to be: thank you!

It would be gross oversight to not mention the hard work of the supporting staff, without whom this department would fall apart. **Etty**, **Heleen**, **Maria**, and **Karin**, thank you for all that you've done for me, and for going the extra mile for the department. **Marinka**, you have helped me through many sticky situations, and your sage advice has often come to my rescue. Thank you for making time for me on short notice, for giving me the tools and perspective to put myself first, and for contextualizing work as just that—work.

To my dearest friends: you're living proof of the old adage that the best things come in small packages. **Gina**, you've been an integral part of my life since our first Macumba night, and have immeasurably improved my time in Delft. Our (miserable) gym session, weekly PSOR drinks, cozy days working from home, and nights dancing (at least until your one one knee gave out) are precious to me. **Gabito**, our friendship was elevated to new heights when I got my first forehead kiss. I can't count the number of times I've poured my heart out to you and Gina at the dining room table—thank you both for your friendship, support, and the innumerable great experiences/chisme we've shared (*¡eso mamonas!*). **Ione**, master knitter and crocheter, ruler of all yarn: your generosity, compassion, and thoughtfulness are remarkable. You take pleasure from the small things in life, and your friendship has given me amazing memories, food experiences, and the ability to knit! **Kays**, you've shaped me as a person, a partner, and a scientist—thank you for believing in me, encouraging me, and being my best friend for so many years. **Tracy**, your smile brightens any room you enter (as confirmed by the democratic process, Royal Victoria College circa 2018). In honor of the current owner of Schwartz's Deli, I will summarize our decade long friendship with a powerful quote: *'near, far, wherever you are, I believe that the heart does go on'*. It goes on, Tray—it goes on. I love you, and I can't wait for the next time I can hold your tiny body in person. **Joanna**, you've been like a sister to me since high school, and I love you (you have to say it back). I wouldn't have dared to move overseas without your courageous example, and I wouldn't have made it throughout this trying experience without your patience and love. I am so proud of the person you've become, and I can hardly summarize what our friendship has meant to me—but know that it's cherished.

To my family, the wind beneath my proverbial wings, thank you for your unconditional love, encouragement, and support. You have believed in me for as long as I can remember, and have braved every step of this tumultuous path with me. **Mattias**, my beloved, to try to distill what you've done for me and meant to me the last few years is a fool's errand, and so I will leave it at this: takk for alt du betyr for meg, jeg elsker deg.